FEMTOSECOND LASER INDUCED RIPPLES AND OTHER APPLICATIONS

STUDY OF ULTRASHORT PULSE LASER INDUCED SURFACE RIPPLES AND INVESTIGATION OF OTHER APPLICATIONS OF ULTRASHORT PULSE LASER MICROMACHINING AND ABLATION

By

EUGENE HSU, B. ENG.

A Thesis

Submitted to the School of Graduate Studies

In Partial Fulfillment of the Requirements

For the Degree

Master of Applied Science

McMaster University

MASTER OF APPLIED SCIENCE (2007) McMaster University

(Engineering Physics) Hamilton, Ontario

TITLE: Study of Ultrashort Pulse Laser Induced Surface Ripples and Investigation of Other Applications of Ultrashort Pulse Laser Micromachining and Ablation

AUTHOR: Eugene Hsu, B. Eng. (Carleton University)

SUPERVISOR: Professor Harold Haugen

NUMBER OF PAGES: xviii, 157

Abstract

This thesis reports findings from three series of experiments related to ultrashort laser pulse interactions with materials. The first series investigates the formation of laser induced ripples that have spatial periods much shorter than the irradiation wavelength after laser irradiation. The second series of experiments explores the capabilities of ultrashort pulse laser micromachining on optical fiber modifications for niche applications. Lastly, preliminary work in establishing a double-pulse ablation technique is reported.

The first set of experiments reported in this thesis investigates the morphology of surface ripples that are generated when irradiated with multiple ultrashort laser pulses. Two types of surface ripples can form after irradiation. The first type has spatial periods near the wavelength of the irradiation pulses and the second has spatial periods substantially below the irradiation wavelength (typically 1/4 to 1/5 of the free-space irradiation wavelength are observed in our studies). These substantially subwavelength ripples form when the irradiation wavelength corresponds to a photon energy that is below the bandgap of the target material. The Ti:Sapphire laser systems used in this series of experiments provides pulses centered around 800 nm. Gallium phosphide (GaP) was chosen to be the main material for investigation since 800 nm corresponds to a photon energy that is below the bandgap of this material; no frequency conversion needs

to be carried out when GaP is the material of choice for subwavelength ripples studies. In this series of experiments substantially different irradiation conditions were investigated: pulse durations varied from 150 fs to 7 ns, laser energies ranges from well above the ablation and modification threshold to well below, both 800 nm and 400 nm wavelengths, and "scrambled" (where polarization was rotated between each successive pulse) polarization as well as circular polarization were used. Microscopy techniques employed to study these ripples include optical microscopy, scanning electron microscopy, atomic force microscopy and transmission electron microscopy. Cross-sectional studies with transmission electron microscopy were also carried out by using focused ion beam milling to prepare thin specimens across irradiated regions. Sapphire was also used as the irradiation target for 800 nm and 400 nm pulses since it has a large bandgap and even 400 nm corresponds to an energy that is below its bandgap. Irradiation conditions where the two types of ripples are observed are determined. Also, microscopy of the ripple features provided insights in to the formation mechanism of the subwavelength ripples.

In the second series of experiments, preliminary work was performed to investigate the capabilities of ultrashort laser micromachining in fiber optic applications. This series of experiments can be subdivided in to two categories.

The goal of the first fiber investigation was to create a slit in a metallic coating deposited on a fiber facet. Such a feature might eliminate the use of

external slits (e.g. for spectrometers), especially if the output of the fiber depends on its geometry (e.g. polarization-maintaining fiber). The first experiment carried out was micromachining of a ~180 nm layer of gold that was deposited on a glass substrate, in order to determine irradiation conditions where the gold layer can be removed while the glass is not damaged. Once the irradiation condition was established by studying the micromachined gold layer on glass substrate, gold layers were deposited on fiber facets for micromachining experiments. The results showed promising potential, but fine tuning of the irradiation parameters, and processing as well as microscopy techniques are needed before useful applications can be realized.

The second set of fiber experiments investigates irradiation conditions that are appropriate to micromachine features into fibers such as v-grooves and beveled ends. Preliminary work was carried out to determine a suitable focusing scheme for this application. Different pulse durations and a pulse train were also employed in hope of minimize chipping and cracking. This investigation did not reach a conclusion on whether micromachining with ultrashort laser pulses are in fact suitable for processing of optical fibers, where high quality facets are required. Future investigation could provide further information on the feasibility of laser micromachining on fabricating features in optical fibers.

Lastly, a double-pulse ablation scheme was established and explored. Double-pulse ablation had been reported in the literature to improve material

removal rate and the appearance of the final morphology. However, this setup can be adapted to investigate the ablation mechanisms and provide insight into the state of the material at different time frames of ablation. While the experimental results are preliminary, this technique showed potential, along with possible extensions of this technique, to further investigate the ablation mechanisms.

Acknowledgements

It would only be natural to take this chance and express my great gratitude to my supervisor Dr. Harold Haugen for providing me with the opportunity with the Photonics Research Lab and the countless hours of guidance throughout my Master's program. On a daily basis, Harold's attention to details and enthusiasm for science has influenced me into a better researcher (so I would like to think). The goals and the welcomed challenges Harold proposed for me had motivated me tremendously and allowed me to achieve much more than I had even hoped for in a M.A.Sc. program. I would also like to thank Dr. Henry Tiedje and Travis Crawford for training me to be proficient in this lab and taking part in many fruitful discussions. Andrew Budz had always been generous in sharing his knowledge with me and fueled my curiosity for physics, along with Jon Waisman and Sarah Golin, they made my time in the Master's program a very pleasant and entertaining experience. "Inspiring" would be an understatement to describe the work ethics and enthusiasm for research exhibited by Sarah Golin and Bernhard Bayer, and in turn, they have became a good part of my motivation factor. Also, it should be pointed out that Sarah and Andrew, on many occasions, have kept my sanity in check throughout my M.A.Sc. program.

Also should be included here are my friends and family that believed in me and encouraged me to further pursue knowledge in graduate studies when I was having doubts myself. Tony Quon, especially, has encouraged me all along and had provided endless entertaining motivational speeches during my thesis writing process. And most of all, Emily Wong, who has given me the courage to venture farther and was more than supportive in my decision to study away from home to take on this opportunity here at McMaster.

Table of Contents

List of Figures

Chapter 1 Introduction

1.1 Introduction to Ultrashort Pulse Laser Technology and Interactions with Materials

Ultrashort laser pulses are typically accepted as laser pulses with pulse durations in or less than the picosecond (10^{-12} s) regime. Pulses with such short durations offer capabilities and applications that longer laser pulses or continuous wave (CW) lasers do not offer. The ultrashort pulse duration provides very high instantaneous power while keeping the average power low. To provide an example, a typical micromachining experiment reported in this thesis uses 2 mW of average power at 1 kHz with a pulse duration of 150 fs (1.5×10^{-13} s); each pulse only has 2 μJ of energy. However, with the short pulse duration the pulse has ~ 15 MW of power. Applications of ultrashort laser pulses include ultrafast spectroscopy [e.g. 1], materials modification and micromachining, diamond cutting, metrology and vast medical applications [2].

In terms of interaction of ultrashort laser pulses with materials, ultrashort pulses are reported to provide cleaner features after material removal [3]. For example, ultrashort laser pulses could deposit energy into the material faster than the electron-phonon interaction time and heat diffusion rate of materials, thus able to modify or remove materials with a small heat affected zone. Ultrashort laser pulses can remove materials in vapour or cluster form [4, 5]. On the contrary, longer laser pulses would introduce a melting phase in the material removal process, causing more splattering, debris and burring in the process [4, 6]. The

clean material removal is suitable for applications where precision is required, such as MEMS and microfluidic passages [6, 7], for example. Due to the high laser intensity, materials that are normally transparent to the laser can be modified or ablated through multiphoton absorption and avalanche processes [8-11].

1.2 Thesis Outline

This thesis presents work performed on ultrashort-pulse laser interactions with materials between September 2005 and 2007, under the supervision of Professor Harold Haugen.

This thesis is divided into 5 main sections. Chapter 2 provides background related to micromachining work, including brief background related to ultrashort pulse laser ablation and micromachining, theory on laser mode-locking, description of the laser system used to carry out the experiments and a typical overall experimental setup, and instruments and techniques to diagnose the laser pulses. Chapter 3 presents a series of experimental work to study the formation mechanism and resulting features of laser induced near-wavelength and substantially sub-wavelength ripples on gallium phosphide and sapphire. Work presented in Chapter 3 is the main focus of the research for this thesis. Chapter 4 presents results from a few preliminary exploratory experiments, including investigation of the application of ultrashort-pulse laser micromachining on optical fibers, as well as a double-pulse ablation and micromachining technique, where two pulses with very short but variable delays are used to irradiate the sample surface. It should be noted that the double-pulse ablation results presented

in Section 4.3 was performed early on in the thesis project and showed promising potential both in improving surface morphologies of ablated features and investigating ablation mechanisms. However the studies of ultrashort-pulse laser induced subwavelength ripple structures (presented in Chapter 3) had since became the focus of the thesis work. Finally, concluding remarks are provided in Chapter 5.

Chapter 2 Background

This chapter of the thesis provides background information related to the ultrashort-pulse laser interactions with materials that most of this thesis is based on. There are three main sections to this chapter. The first part of this chapter provides some brief proposed mechanism in the literature on ultrashort pulse laser ablation mechanisms. Following the background on ultrashort pulse laser ablation, theory and description of the laser systems used to perform the experiments described in this thesis are provided. Finally, the last part of this chapter describes setups and techniques used to diagnose and measure the ultrashort laser pulses.

2.1 Background: Ultrashort Pulse Laser Ablation

This section of the thesis provides a brief overview of processes involved in ablation caused by ultrashort pulse laser processing. This section is not a comprehensive literature review for all the experiments included in this thesis. Literature related to niche topics that apply to the specific experiments reported in this thesis are discussed in individual subsections in Chapter 3 and Chapter 4.

Aside from continuous-wave laser systems, laser systems in use today typically provide pulse durations of a few tens of nanoseconds down to a few tens of femtoseconds. It is generally accepted that ultrashort laser pulses refer to laser pulses with pulse durations below a few picoseconds. In the discussion to follow

in this section, "long pulse" or "longer pulses" will be used to describe laser pulses with durations longer than this time frame.

When a continuous-wave laser is used to irradiate a material, due to the continuous energy deposition that is over a time scale much larger than electron-lattice coupling time, material removal using CW lasers primarily depends on melting of the material. The physics of laser processing with CW lasers can be modeled entirely based on classical heat and mass transfer laws [12].

When nanosecond laser pulses are used, the pulse duration is still a few orders of magnitude higher than the electron-lattice coupling time. Consequently, equilibrium can be assumed in the temperatures of the excited electronic subsystem and the lattice, and traditional heat transfer models can be applied [12]. The long pulse duration relative to the electron-lattice coupling time results in heating of the lattice. When adequate energy is deposited in the material, slight melting is followed by rapid evaporation [12, 13]. It should be noted the heat conduction begins to occur as the pulse is still irradiating the material surface. The heat affected zone (HAZ) is smaller than processing performed by CW laser irradiation. However, the existence of a liquid-phase does act to limit the precision of material removal and the final ablated/micromachined features [12, 13]. The precision and smallest feature obtainable by nanosecond laser machining is limited by the heat conduction distance. Ejection of a plume also occurs with nanosecond laser ablation when higher fluences are used (when over ~2-3 times the threshold fluence for the material) [14]. The plume acts to screen

the trailing part of the pulse that is still approaching the sample surface. This effect becomes significant after a few picoseconds following the initial incidence of the laser pulse [14].

In the case of laser ablation with ultrashort pulses, the laser pulse duration is shorter than the electron-lattice coupling time; deposition of laser energy into the material surface occurs without much of the energy being transferred away from the target region by thermal conduction. The electrons are heated almost instantly, and on a picosecond time scale (for most materials) the excited electrons transfer their energy to the lattice. If the energy is adequate, the bonds of the lattice are broken, causing a direct solid-vapour and plasma transition, followed by rapid expansion [12, 13]. Since the involvement of lattice heating is minimal, certain regimes of ultrashort-pulse laser ablation process is sometimes considered as non-thermal ablation. Based on the same phenomena, the heat affected zone is also minimized. Due to high intensities associated with ultrashort laser pulses, nonlinear processes such as multiphoton absorption and avalanche ionization can occur readily, allowing the ablation of materials that are transparent to the irradiation wavelength of the laser at lower intensities [12].

The above description for ablation mechanisms with ultrashort laser pulses is a simplified "ideal" scenario. Since the work presented in this thesis is primarily based on the interaction of ultrashort laser pulses with materials, more details on the possible mechanisms involved should be discussed.

2.1.1 Mechanisms of Ultrashort Pulse Laser Ablation

There are several proposed mechanisms in the literature responsible for ultrashort pulse laser ablation. The exact processes of ultrashort-pulse laser ablation still have not been clearly identified and are still under discussion in the literature. Part of the challenge arises from the ultrashort time frame where assumptions imposed on models for long pulse ablation can not be applied; a highly non-equilibrium state that occurs in the ultrashort period of time creates intricacies in modeling of ultrashort pulse laser ablation.

It was shown experimentally that different materials behave similarly when irradiated with ultrashort laser pulses, suggesting that the same general mechanisms are responsible for the ablation process [15, 16]. This is not a surprising observation since the laser energy is deposited in a time period much faster than the electronic system could interact with the lattice for most materials. The electron-lattice time constants as well as heat diffusion rate from different materials are less significant in ultrashort pulse laser ablation compared to long pulse processing.

Coulomb Explosion

In ablation with laser fluences close to the ablation threshold, Coulomb explosion is proposed as one of the mechanisms at play for ablation. Coulomb explosion begins to occur in a femtosecond time scale as excited electrons gain enough energy to leave the material surface. This creates a net positive surface

charge. As the density of the positive ions increase, repulsive force between the positive ions causes instability in the mechanical structure of the lattice and explosion occurs from this repulsive force. Heating of the lattice is not significant at low fluences when Coulomb explosion is the primary mechanism for ablation [17-19].

Coulomb explosion as a contributing factor for semiconductors is under debate in the literature [17]. However, supportive evidence such as the emission of positive ions are being reported [17, 18, 20]. Figure 2-1 is a symbolic diagram of the Coulomb explosion process.

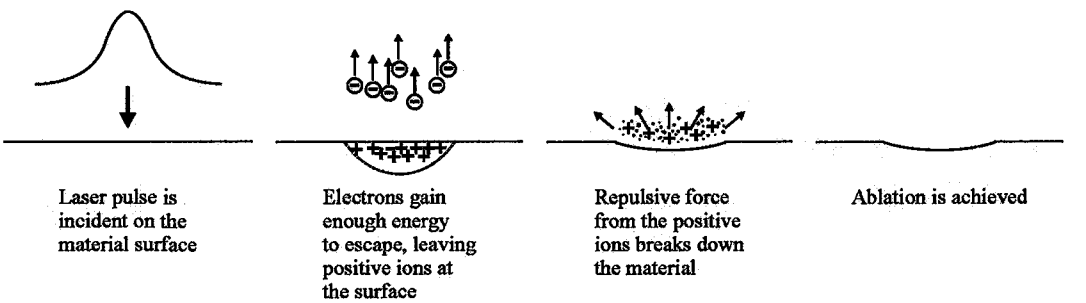

Figure 2-1: Symbolic diagram of the Coulomb explosion process. The region enclosed by dashed lines represents the region over which the laser energy is absorbed. Note that the dimensions of the energy absorption region and ablated region are arbitrary.

Spallation

Spallation is another proposed mechanism that occurs when materials are irradiated with near-threshold fluences. After irradiation, two compressive pressure waves propagate from the irradiated region, one of which propagates towards the bulk and the other towards the surface. The wave is incident on the surface and reflects, where the reflected component becomes tensile [21, 22]. This tensile stress causes fracture beneath the surface and consequently a layer of

the material is ejected [21, 23, 24]. Stress confinement is required to create strong pressure waves, thus spallation is most likely restricted to ultrashort laser ablation [21]. At higher fluences, the material is softened due to thermal effects and the propagation of the pressure wave is dampened [21], spallation thus becomes suppressed.

Figure 2-2 is a symbolic diagram for the spallation process.

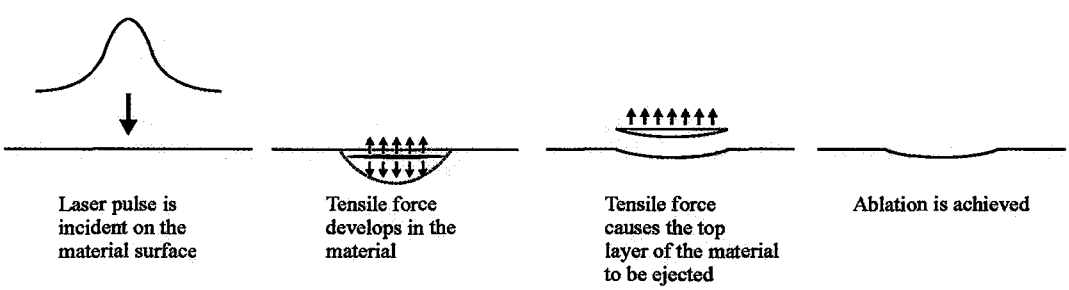

Figure 2-2: Symbolic diagram of the spallation process. The region enclosed by dashed lines represents the region over which the laser energy is absorbed. Note that the dimensions of the energy absorption region and ablated region are drawn arbitrary. The diagrams are symbolic representation only; in real life scenarios the ejected layer does not have a smooth boundary.

Homogeneous Nucleation (Phase explosion)

Homogeneous nucleation, or phase explosion, occurs at fluences higher than the range where Coulomb explosion or spallation occurs. When a higher laser fluence is used, free electron density increases due to higher excitation energy. The electrons relax through electron-phonon collision on a sub-picosecond to picosecond time scale for most materials [18, 25], heating the surface of the material high above the melting point. However, the volume of the material practically remains constant in this time frame since volume expansion is

limited to the speed of sound and relaxation through volume expansion is expected to occur on a few picosecond time scale [11, 18, 25]. The high heating rate creates a homogeneous, superheated liquid. As the liquid expands, it enters a liquid-vapour metastable regime where the gas phase is the most stable phase of the material but an energy barrier exists between the liquid phase and the gas phase. Gas bubbles will form inside the liquid, through a process called homogeneous nucleation (or phase explosion) [16, 18, 21, 24, 26, 27]. The pressure of the system causes the gas bubbles to expand. Eventually the bubbles rupture, releasing the built-up pressure and causing ejection of the material. This process is responsible for phase explosion in laser ablation [11, 18, 21, 28].

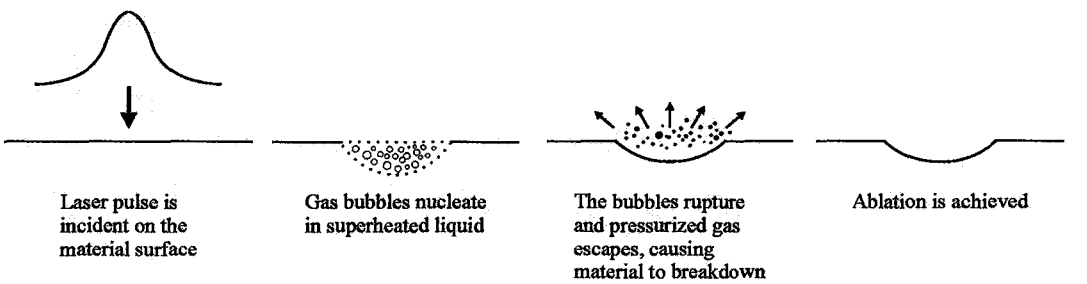

Figure 2-3: Symbolic diagram of the phase explosion process. The region enclosed by dashed lines represents the region over which the laser energy is absorbed. Note that the dimensions of the energy absorption region and ablated region are drawn arbitrary.

Fragmentation

Fragmentation occurs when the material is exposed to even higher laser fluence than where phase explosion occurs. In this case the irradiated region heats up with a very high heating rate and the material is pushed into a superheated solid state [21]. Like phase explosion, this rapid heating occurs at a

constant volume since it takes place at a time frame faster than the material expansion occurs [11, 18, 25]. Melting occurs quickly and the material expands as a supercritical fluid, after which voids begin to appear [21, 27, 24]. The main difference between fragmentation and phase explosion is that in fragmentation the voids begin to occur (and thus the material decomposes) much earlier than the material enters a liquid-vapour metastable state [21]. This implies that fragmentation and phase explosion are mutually exclusive processes [21, 24].

Fragmentation can also be described from a stress point of view. A large stress is induced by the constant-volume heating, causing a rapid expansion at a very high speed. The stress and thus the expansion rate is a varying function of the energy deposited at the specific location of the target. The gradient in the expansion speed will prevent the fluctuations of density from reaching equilibrium; the inhomogeneities are retained and can actually grow, causing internal surfaces to form as a means of relaxation. This creates clusters inside the expanding material, and ablation occurs [15].

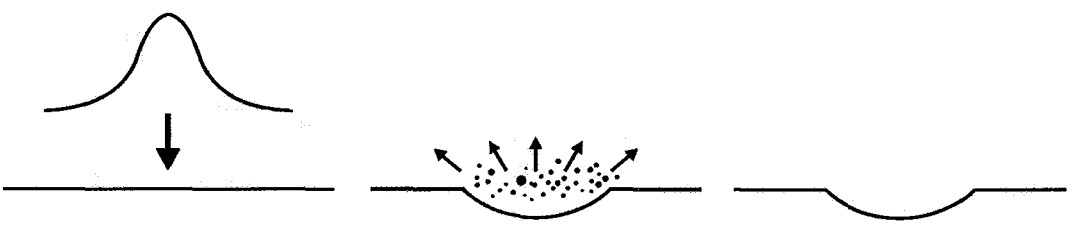

Figure 2-4: Symbolic description of the fragmentation process. Note that the dimensions of the energy absorption region and ablated region are drawn arbitrary.

Vaporization

Vaporization is proposed to occur when the laser energy is close to or exceeds the cohesive energy of the material. In this case the deposited high energy is adequate to break the bonds of the lattice, causing ejection of the atoms. When vaporization occurs the ejected material behaves as a gas [15, 21].

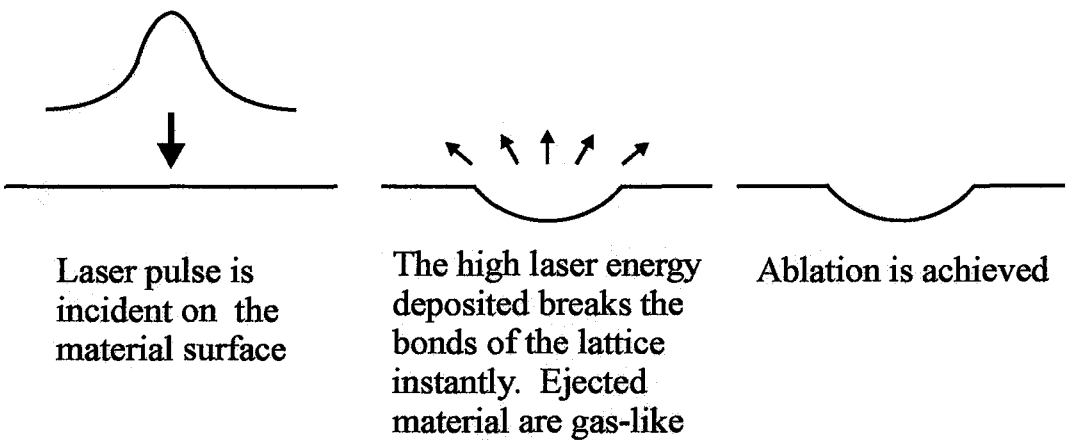

Figure 2-5: Symbolic description of the vaporization process. Note that the dimensions ablated region is drawn arbitrary.

The five ablation mechanisms described above are proposed based on theoretical modeling and some of them are confirmed to be contributing factors with suggestive experimental results [e.g. 26]. As described above, the dominating mechanism for the ablation process depends on the local fluence. Since the pulses have an approximately Gaussian spatial intensity distribution, the local fluence arriving at the material surface varies across the diameter of the beam. It was proposed that a few of the mechanisms describe above can occur

when the material is irradiated with a laser pulse and that no single process alone can account for ablation [12].

2.1.2 Time Frames of Events in Ultrashort Pulse Laser Ablation

This subsection of the thesis provides time frames of events involved in ablation processes.

Due to the different electronic structures, metals, semiconductors, large bandgap semiconductors and dielectrics have different means of optical energy absorption [29]. In metals, optical absorption is dominated by free carrier absorption [29]. If the photon energy of the irradiation light is larger than the bandgap of a semiconductor, the optical energy excites electrons from the valence band to the conduction band [29]. For wide bandgap semiconductors and dielectrics, where the photon energy is below bandgap, multiphoton transitions are required to excite electrons from the valence band to the conduction band [29].

The discussion below regarding time frames of events associated with ultrashort-pulse laser ablation are based on the summary presented in [29 (and references therein), 16]. In metals, semiconductors and dielectrics, optical absorption and electron excitation occur on a time scale of ~100 fs [29]. For metals, semiconductors and dielectrics irradiated with lower pulse intensity, lattice heating (due to electron-lattice energy coupling) occurs between several

hundreds of femtoseconds to the picosecond time scale. The heated lattice can undergo heterogeneous melting (for irradiation with lower intensity pulses) between a few tens to a few hundreds of picoseconds, homogeneous melting (for irradiation with higher intensity pulses) in a few to a few tens of picoseconds, or become an overcritical fluid (at even higher pulse intensity) on the same time scale [29]. Depending on the pressure and temperature of the material, the homogeneously melted material can quickly turn into overcritical fluid as well [29]. On another hand, when semiconductors and dielectrics are irradiated with higher intensity pulses, nonthermal melting (lattice destabilization) or the formation of a plasma state (for irradiation with energy higher than the cohesive energy of the bonds) can form in a few tens of femtoseconds [29]. Nonthermal melting can, again, lead to the formation of overcritical fluid in a few to a few tens of picoseconds [29]. Following either homogeneous melting, formation of overcritical fluid or a plasma state, ablation takes place in a few hundreds of picoseconds to a few nanoseconds [29]. Surface cooling and resolidification begin to occur after a few tens of nanosecond, and reaches its final state under 100 ns [29, 16].

2.2 Typical Experimental Setup

Some essential background related to the laser system is introduced in the following subsections. As well, the femtosecond laser system used to perform the experiments reported in this thesis will be explained. A typical experimental

setup for ultrashort pulse laser ablation and micromachining work will be described.

2.2.1 The Femtosecond Laser System

The femtosecond laser system used for most of the experiments described in this thesis consists of a continuous wave, frequency-doubled Nd:YVO_4 laser at 532 nm (Millenia V) that pumps a Titanium:Sapphire mode-locked oscillator (Tsunami). The output of this oscillator is used as seed pulses in a Titanium:Sapphire chirped-pulse amplifier (Spitfire) pumped by a 1 kHz 527 nm Q-switched, frequency-doubled arc-lamp-pumped Nd:YLF laser source (Merlin). In some experiments another Ti:Sapphire laser system is used in conjunction with the system described above. In the second system, the setup is similar to the one above, with the exception of the amplifier being pumped by a diode-pumped Nd:YLF source (Evolution), and the system providing shorter pulses with a larger spectral bandwidth. Titanium doped sapphire crystals are widely used in femtosecond work due to their superb suitability for this application. They have high optical and thermal breakdown threshold and have a wide optical bandwidth [e.g. 30]. The high optical and thermal breakdown threshold allows them to withstand the high intensity associated with the ultrashort laser pulses. A gain medium supporting a wide optical bandwidth allows very short pulse output when mode-locked [3]. Titanium:Sapphire lasers have a maximum spectral width of ~400 nm (spanning from ~700 nm to 1100 nm [1, 29, 31]), corresponding to a

theoretical minimum pulse duration of 3 fs [3]. Titanium:Sapphire crystals have peak absorption between 400 nm to 600 nm, and an emission band centered around 800 nm. Brief theoretical backgrounds and more detailed descriptions of each part of the laser system are provided in the following subsections of this chapter.

2.2.1.1 Mode-Locking

In a given laser cavity, only frequencies that satisfy the following relationship can oscillate in the cavity:

$$\nu = \frac{ac}{2L} \qquad \textbf{(2-1)}$$

where a is an integer and L is the length of the cavity. This equation defines the longitudinal modes that can exist for a given oscillator geometry. Three operation regimes can exist for a given cavity [32]:

- Single mode operation, where one longitudinal mode is selectively favored by the oscillator cavity while the other modes are suppressed.
- Multimode operation, with random relative phases
- Multimode operation, with the phases of each mode locked such that in a point in time the peaks from all the modes overlap. This

regime is commonly referred to as the "mode-locked" operation regime.

The superimposition of all the peaks in the mode-locked regime allows the generation of short pulses. As the number of modes increases, the duration of the superimposed peak decreases. Figure 2-6 show simulation results of the addition of three sine waves with random phases as well as the same three sine waves phase locked such that the peaks of the sine waves occur at the same point in time.

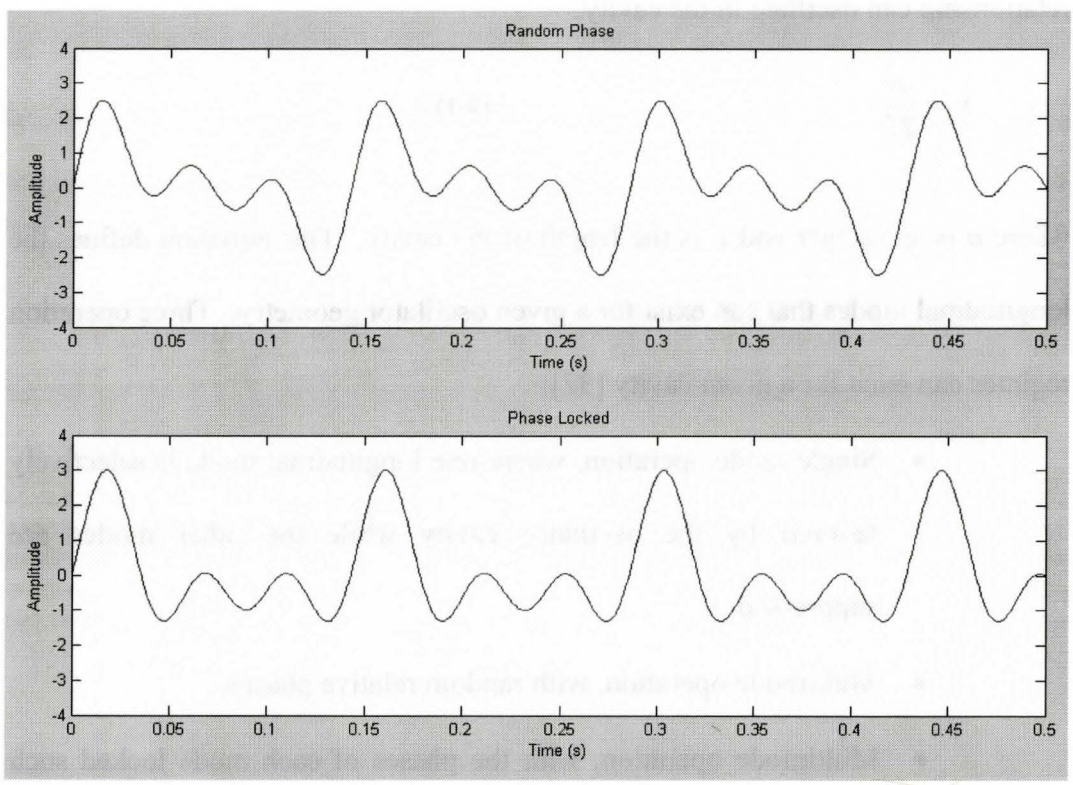

Figure 2-6: Summing of three sine waves with different frequencies (7 Hz, 14 Hz and 21 Hz) with a random phase relationship (top), and phase locked so that the peaks occur at the same point in time periodically (bottom).

Aside from cavity geometry, the spectral components of the output laser pulses also depend on the gain bandwidth of the amplifying medium; a specific mode must overcome the losses of the optical elements in the cavity for oscillation of that mode to occur.

There are several different schemes to create a mode-locked operation regime in a laser oscillator. When external modulators are used, an active mode-locking scheme is established [3]. On the contrary, when a saturable absorber is used in the cavity a passive mode-locking scheme is in place [3]. A mode-locking scheme where the gain medium itself contributes to the locking of the modes is referred to as "self-locking". Details of different mode-locking techniques are outside the scope of this thesis. However, a specific mode-locking technique, "Kerr lens mode-locking", is used in Titanium:Sapphire oscillators and will be discussed [3]. Since the Titanium:Sapphire crystal itself acts as a nonlinear medium for the Kerr lens effect, self-locking of the mode can be achieved with this setup.

The Kerr lens effect is a nonlinear effect and it exists due to a dependence of the refractive index of the material on the intensity of light. More specifically, the relationship between the refractive index of a material and the intensity of the light is given by:

$$n(I) = n_o + n_2 I \qquad \textbf{(2-2)}$$

where I is the intensity of the light, $n(I)$ is the refractive index experienced by the light propagating through the material, n_o is refractive index of the material, and n_2 is the nonlinear refractive index.

It is typically reasonable to assume a Gaussian spatial profile for the laser pulses. For a positive n_2, the central portion of the beam will experience the highest refractive index. A Kerr lens effect occurs when the intensity exceeds 10^{11} W/cm^2 in Titanium:Sapphire crystals [30]. At this intensity we estimate the change in the refractive index for the crystal to be 3.1×10^{-5}. Farther away from the propagation axis of the beam, where the intensity decreases due to the Gaussian beam profile, a lower refractive index is experienced by the pulse. The overall effect is analogous to that of a converging lens.

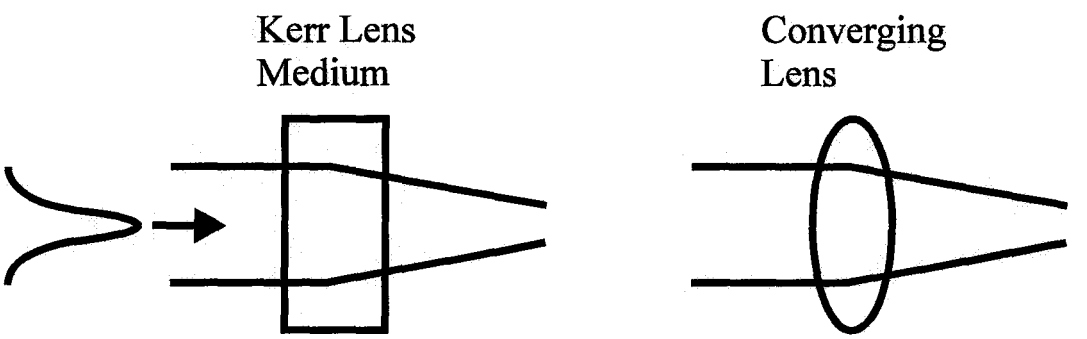

Figure 2-7: Symbolic diagram of Kerr lens effect. Due to the higher refractive index experienced at the higher intensity portion of the pulse, the overall effect of a high intensity pulse propagating through a Kerr lens medium is similar to light propagating through a converging lens. The converging angles for both cases are drawn arbitrarily.

The need for high intensity favors the oscillation of short pulses once the Kerr lens effect is established [30]. Another factor that contributes to discriminate against cw operation (the regime that a Titanium:Sapphire system operates in a non-mode-locked regime) is the reduced spatial profile of the

pulsed-mode oscillation due to Kerr lens effect. A beam with smaller profile typically experiences less optical losses in the optics of the cavity [3]. To further increase the discrimination against cw operation mode, a slit or an aperture is introduced in the cavity where the opening allows the narrowed intense pulses through. If the oscillation modes are not mode-locked, the intensity is low compared to the pulses in mode-locked regime. In this case the Kerr lens effect is not significant, and the beam size is not reduced as the light propagates through the Titanium:Sapphire crystal. As a result, the beam profile of a non-mode-locked beam remains large and part of the beam is clipped by the slit or the aperture. This creates a lossy cavity in the non-mode-locked regime, while a low-loss cavity exists when the cavity is mode-locked (Figure 2-8).

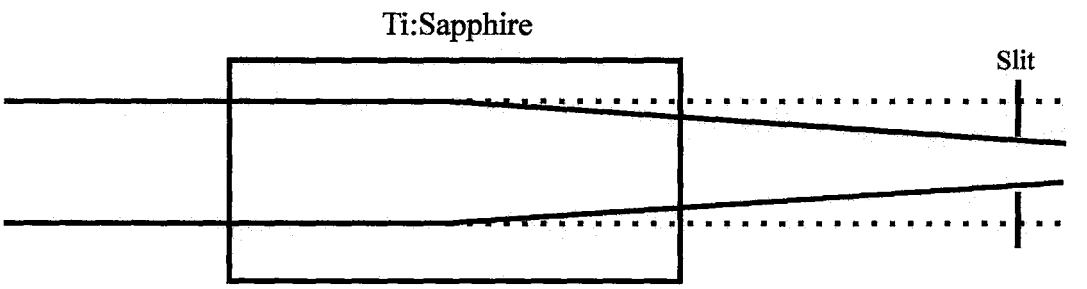

Figure 2-8: Symbolic representation of the combination of a slit and Kerr lens effect acting together to behave as a saturable absorber. Higher intensity modes are represented by solid lines and lower intensity modes are represented by dashed lines. The diagram is a symbolic representation only, the focusing behavior of the beam presented is not based on calculation. The placement of the slit also differs from the exact placement in a real-life Ti:Sapphire oscillator, with intermediate optics omitted.

The combination of the slit and a Kerr lens medium, as well as discriminatory losses from the optical elements, are analogous to a saturable absorber in a passive mode-locking scheme. However such a setup has a response

time in the femtosecond range, whereas a semiconductor saturable absorber has a response time in the picosecond range [32].

2.2.1.2 Titanium:Sapphire Oscillator

The Titanium:Sapphire oscillator (Spectra Physics Tsunami) of the ultrashort laser system is pumped by a Spectra Physics Millennia V neodymium yttrium vanadate (Nd:YVO_4) laser that is frequency-doubled to 532 nm. A technique known as longitudinal pumping is used in the oscillator. In this technique the pump beam is focused into a narrow line as it propagates through the Titanium:Sapphire crystal to ensure continuous inversion density throughout the length of the crystal rod. A narrow beam is used since it is difficult to create a scenario where continuous inversion density is achieved throughout the entire volume of the crystal, which is several millimeters in diameter. The oscillating laser mode is focused similarly to overlap in the same volume in the crystal [31]. Dichromatic mirrors are used to retain the oscillating modes in the cavity while allowing the pump beam to exit the cavity.

As discussed previously, self-locking of the modes are achieved in the oscillator using Kerr lens mode-locking (see previous section for details). However, another intensity-dependent nonlinear optical effect also exists in a Titanium:Sapphire oscillator. While Kerr lens effect affects the spatial profile of the beam, the phase of the pulses in the time domain is also affected by the intensity of the pulse. It is typically reasonable to assume a Gaussian intensity distribution of the laser pulses in the time domain. The change of intensity in

time, due to the Gaussian intensity distribution, implies that different refractive indices are experienced by different part of the pulse as it propagates through the material. This leads to an instantaneous phase shift of the pulses. This effect is referred to as self-phase modulation (SPM) and can lead to the generation of the broad pulse spectrum required for short pulse generation [32]. Figure 2-9 demonstrates the relationship between phase shift and the intensity of the pulse as a function of time due to self phase modulation.

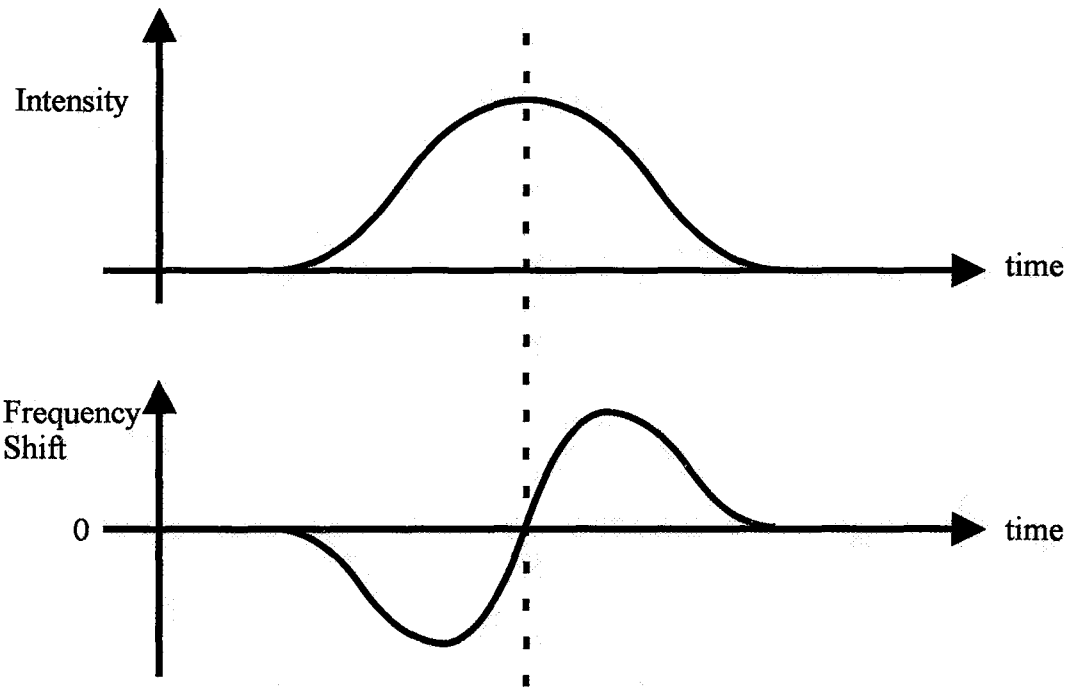

Figure 2-9: Frequency shifting as a result of self phase modulation due to the Gaussian distribution of pulse intensity in time.

In a dispersive medium where the group refractive index varies with the wavelength of the propagating light, causing different spectral components of the pulse to travel at different speeds, temporal broadening of the pulses can occur.

This effect is referred to as Group Velocity Dispersion, or GVD. The combination of SPM in the Ti:Sapphire crystal and positive GVD from in the oscillator cavity leads to a positive chirp of the pulses. A positive chirp refers to a pulse where the (temporally) leading part of the pulse has a longer wavelength than the trailing part. To ensure stable oscillation condition, this positive chirp needs be compensated. This can be done by introducing prism pairs in the cavity. A slit is placed in the prism setup where the positioning of the slit selects the central wavelength of the oscillating modes, while the size of the slit opening controls the spectral bandwidth. An acousto-optic modulator is used to initiate the mode-locking when the laser is first started.

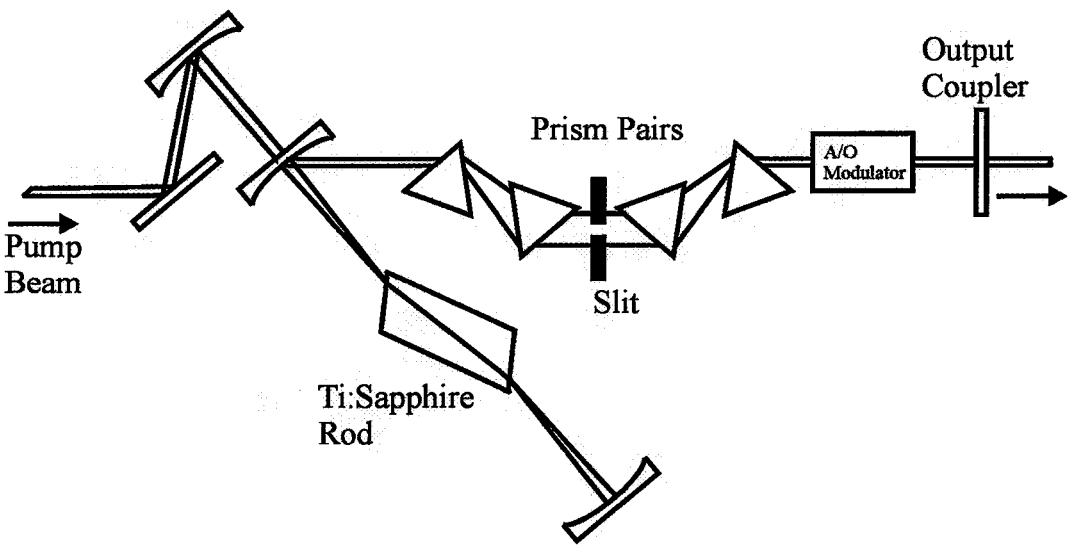

Figure 2-10: Symbolic diagram of a Ti:Sapphire oscillator. This diagram is simplified and some optical elements that are included in a real-life oscillator are omitted. Please note this is a symbolic representation and the geometries of the beam and the optics are not based on calculations.

The Tsunami is capable of producing pulses with an energy of ~7.5 nJ and a duration of 90 fs at a repetition rate of 82 MHz. The pulses are centered around a wavelength of 800 nm and have a full-width half max (FWHM) bandwidth of ~10 nm.

2.2.1.3 Chirped-Pulse Amplifier

Ultrashort pulses can have a very high instantaneous intensity due to the short pulse duration. The high intensity can lead to thermal damage to the optical components in the amplifier where the pulse energies are amplified by more than five orders of magnitude [29, 33]. Nonlinear effects associated with the high intensity can also cause unwanted effects. For example, Kerr lens effect can cause self focusing of the laser pulses in the long Ti:Sapphire crystal rod, creating a localized high intensity region and causing damage to the rod. Dispersion due to nonlinear effects can also occur due to the high intensity, changing the focusing properties of the pulses after amplification [30].

To circumvent the issues associated with amplifying ultrashort laser pulses, a chirped-pulse amplification scheme was introduced in the mid 1980's [34]. In this technique an incoming ultrashort laser pulse is "stretched" in time through the use of dispersive optics. The pulses are stretched by creating a temporal offset of the spectrum, or a temporal "chirp", hence the name "chirped-pulse amplification".

The stretched pulses are subsequently amplified in a regenerative amplifier pumped by a 1 kHz pump beam. The amplified pulses are recompressed through a compressor in the last stage of the amplifier to generate amplified ultrashort pulses as the output.

Overall, the Chirped-Pulse Amplifier, or CPA, can be broken down into three parts: a pulse stretcher, a regenerative amplifier, and a pulse compressor Each individual part is discussed in the following subsections.

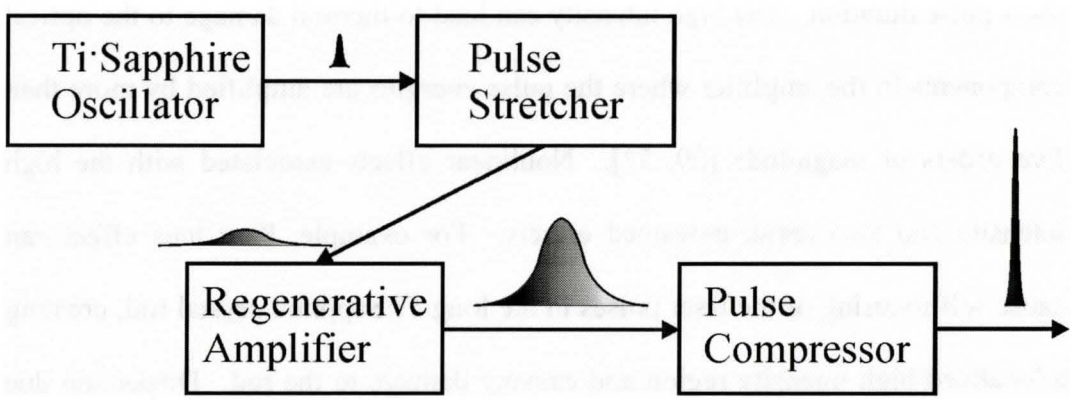

Figure 2-11: Symbolic representation of a chirped pulse amplifier. A seed pulse from the Ti:Sapphire oscillator is stretched in time, amplified and recompressed subsequently. The difference in shading represents different spectral components within the pulse.

The following is a summary of typical pulse durations and energies at different stages of the two Ti:Sapphire CPAs that were available for the experiments reported in this thesis:

Table 1: Summary of pulse durations and pulse energies at different stages of the Ti:Sapphire CPA systems.

		Pulse Duration	Pulse Energy
Ti:Sapphire System #1	Oscillator Output	~90 fs	~7.5 nJ
	Stretcher Output	~220 ps	~5.4 nJ*
	Regenerative Amplifier Output	~220 ps	~565 μJ
	Compressor Output	~150 fs	~350 μJ
Ti:Sapphire System #2	Oscillator Output	~45 fs	~5.5 nJ
	Stretcher Output	~130 ps	~3.9 nJ*
	Regenerative Amplifier Output	~130 ps	~900 μJ
	Compressor Output	~50 fs	~540 μJ

*Pulse energies are estimated based on losses from the gratings in the stretcher.

2.2.1.3.1 Pulse Stretcher

The first part of the CPA is the pulse stretcher. Pulse stretching is required to prevent damage from occurring inside the regenerative amplifier due to the high intensity of the ultrashort pulses. Temporal stretching of the pulses is achieved by spatially spreading the spectrum in the "seed" pulses (output of the oscillator) such that different spectral components have slightly different optical path lengths from one another and when these components are recombined a temporal broadening is obtained due to these path length differences. Since the spectral component of the output pulse is changing in time, the pulse is said to be "chirped". A symbolic diagram is presented in Figure 2-12 to demonstrate pulse stretching with diffraction gratings.

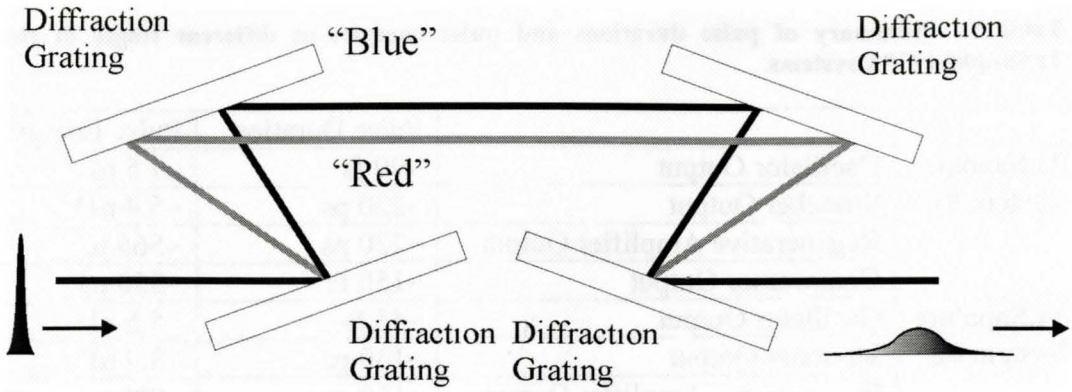

Figure 2-12: Pulse stretcher setup based on chirping technique. Different shading represents different spectral components in the incident pulse. When the different components are merged, the "redder" components will lag in time due to a longer beam path, resulting in a pulse longer than the incoming pulse. Note this figure is a symbolic representation only; diffraction angles shown are not based on calculations.

A pulse with shorter wavelength leading in time, as the output pulse in Figure 2-12, is said to have a "negative chirp", and the stretcher shown in this figure is said to have a negative GVD. However, in order to use a compressor to undo the pulse stretching after amplifying, the GVD in the stretcher and the compressor need to have opposite signs.

In the case of the CPA used for experiments reported in this thesis, the stretcher produces a positively chirped pulse that is recompressed, after amplification, with a compressor with a negative GVD.

To reverse the sign of GVD in the stretcher, telescopes can be used, as illustrated in Figure 2-13

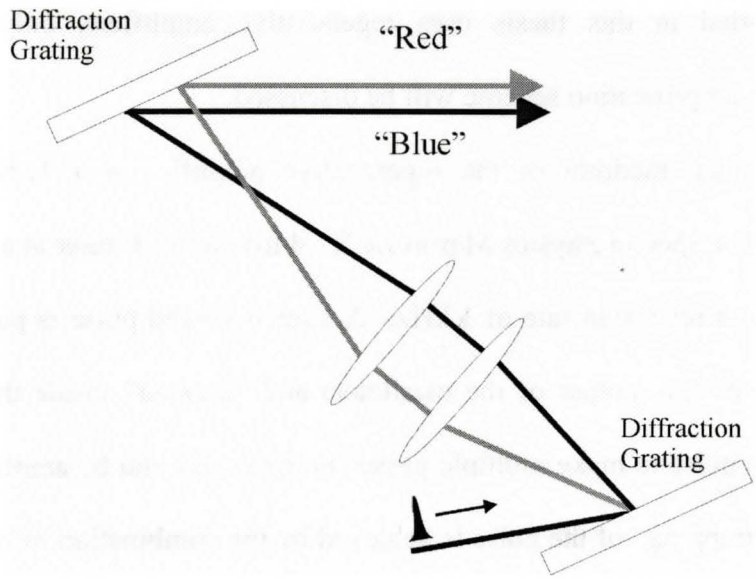

Figure 2-13: Reversing the sign of GVD with the use of a telescope comprising of two converging lenses. The telescope "switches" the beam paths of the "reder" and "bluer" components, thus overall the sign of the GVD for the stretcher is switched from negative to positive.

Note the setup shown in Figure 2-12 uses four gratings with unfolded beam paths to present a simplified visualization of such a technique. In actuality a single grating is used inside the stretcher of the CPA and mirrors are placed in the stretcher to fold the beam path such that the beam is incident on the grating four times, thus achieving the effect equivalent to a system with four separate gratings. The folding of the beam path allows the system to be made more compact. Instead of lenses, a curved mirror acts as the lenses in the telescope to switch the GVD from negative to positive in the stretcher

2.2.1.3.2 Regenerative Amplifier

Two popular types of amplifiers exist in CPAs amplifiers: regenerative amplifier and multipass amplifiers [32]. Since the CPAs used for all experimental

works reported in this thesis uses regenerative amplifiers, only details on regenerative amplification scheme will be discussed.

The gain medium of the regenerative amplifier is a Ti:Sapphire rod pumped with a Spectra Physics Merlin LCX ~4 mJ Nd:YLF laser at a wavelength of 527 nm and repetition rate of 1 kHz. A stretched seed pulse is picked from a train of pulses (i.e. output of the oscillator) and "trapped" inside the amplifier, allowing the pulse to make multiple passes in the cavity and be amplified in each pass. The "trapping" of the pulse is achieved by the combination of manipulation the polarization of the pulses via Pockels cells and the use of polarizer.

A Pockels cell is a material that exhibits linear electrooptic effect, or Pockels effect, where a linear change in the refractive index of the material occurs when a DC or low-frequency signal is applied to the material [35]. More specifically, the Pockels cells used in the regenerative amplifiers are based on potassium dihydrogen phosphate (KDP) crystals, where when properly aligned they allow light to propagate through unchanged without an applied voltage, but exhibit quarter-wave plate or half-wave plate behaviors depending on the applied voltage. A quarter-wave plate transforms linearly polarized light into circularly polarized light and vice versa, whereas a half-wave plate rotates the polarization of the incident light.

Figure 2-1 is a symbolic diagram representing the components in the regenerative amplifier.

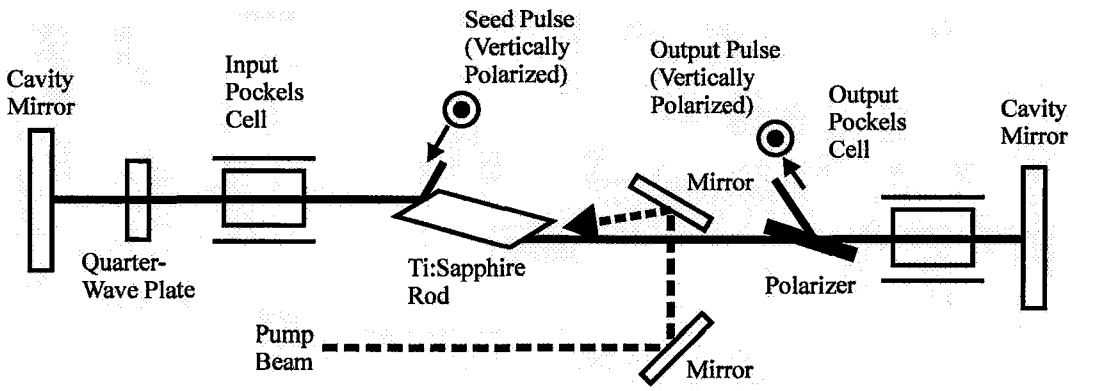

Figure 2-14: Symbolic diagram of a Ti:Sapphire regenerative amplifier.

The operation of a regenerative amplifier is as follows. A vertically polarized pulse is injected into the cavity from the stretcher and reflects off the facet of the Ti:Sapphire crystal. When the pump pulse is not present, the input Pockels cell is deactivated. The pulse passes through a quarter-wave plate, reflects off a cavity mirror and passes through the quarter-wave plate again. Since the pulse passes through the quarter-wave plate twice, the overall result is equivalent to passing through a half-wave plate; the polarization of the pulse is rotated by 90° and is now horizontally polarized. As the pulse makes a round-trip and makes another double-pass through the quarter-wave plate, its polarization is rotated by another 90°, returning to vertical polarization, and is reflected off the Ti:Sapphire crystal and exits the cavity. Since these events take place when the Ti:Sapphire crystal is not pumped, the pulse experiences little to no amplification. In fact, the pulse will experience attenuation from the optical elements in the regenerative amplifier.

The Pockels cell is synchronized (with an adjustable delay) to the pump pulses. When a vertically polarized seed pulse is injected into the cavity it passes

through the non-active input Pockels cell, it makes a double-pass through the quarter-wave plate (due to reflection off the cavity mirror) and becomes horizontally polarized, then back through the input Pockels cell. Immediately after the pulse exits the input Pockels cell, a voltage is applied to the Pockels cell so that it behaves as a quarter-wave plate. This voltage is referred to as the quarter-wave voltage. As the pulse makes a round trip in the cavity, it would then propagate through the input Pockels cell with a quarter-wave voltage applied to it, followed by a quartz quarter-wave plate. Overall the input Pockels cell and the quarter-wave plate together behave as a half-wave plate. As the pulse reflects through the cavity mirror and passes through the quarter-wave plate and the Pockels cell again, it experiences an equivalent effect of another half-wave plate. At this point, the pulse had passed through an equivalent of a full-wave plate; the polarization of the pulse is horizontal, and thus remains trapped in the cavity. Since the Ti:Sapphire crystal is now pumped, the pulse is amplified each time it propagates through the crystal. When the amplification of the pulse reaches a maximum, a quarter-wave voltage is applied to the output Pockels cell. The pulse makes a double-pass through the output Pockels cell (due to the cavity mirror) and the polarization of the pulse is rotated by 90°, allowing the pulse to reflect off the polarizer and exit the amplifier.

2.2.1.3.3 Pulse Compressor

The basic concept of the pulse compressor is similar to that of a pulse stretcher. Diffraction gratings are used to spatially spread out different spectral

components of the pulse so that different components travel through different path lengths. Figure 2-15 is a symbolic illustration of the pulse compressor with a negative GVD, as is the case in the compressor used in the CPA employed for experiments reported in this thesis.

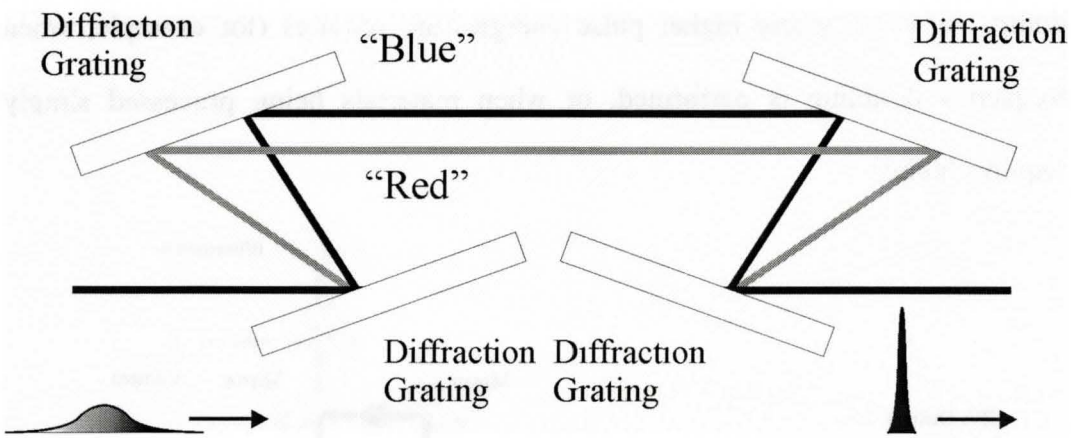

Figure 2-15: Gratings configuration with a negative GVD that compresses a positively chirped incoming pulse. The leading "red" component of the chirped pulse travels through a longer path length than the lagging "blue" component of the pulse, thus overall the pulse is compressed. Note this figure is a symbolic representation only; diffraction angles shown are not based on calculations.

2.2.2 Typical Laser Micromachining Setup

Figure 2-16 depicts the setup for a typical micromachining experiment. Beam delivery between the Ti:Sapphire system and the micromachining setup (~ 8 m) is achieved using a series of mirrors. The output beam of the Ti:Sapphire system is estimated to be ~ 5 mm in diameter ($1/e^2$). For sections of where the beam travels a longer distance along the optical bench, tubes are placed to enclose the beam. These beam tubes prevent stray beam from traveling across the

laboratory if a mirror is misaligned. Also they prevent users from accidental exposure to the beam and provide stability of the beam at the micromachining setup (e.g. reduces interference of air currents). Typically, initial attenuation of the laser pulses is achieved by using a beam-splitter, where 20% of the energy is kept for micromachining use, while 80% of the energy is captured in a beam-dump. In cases where higher pulse energies are requires (for example, when frequency doubling is performed, or when materials being processed simply requires higher

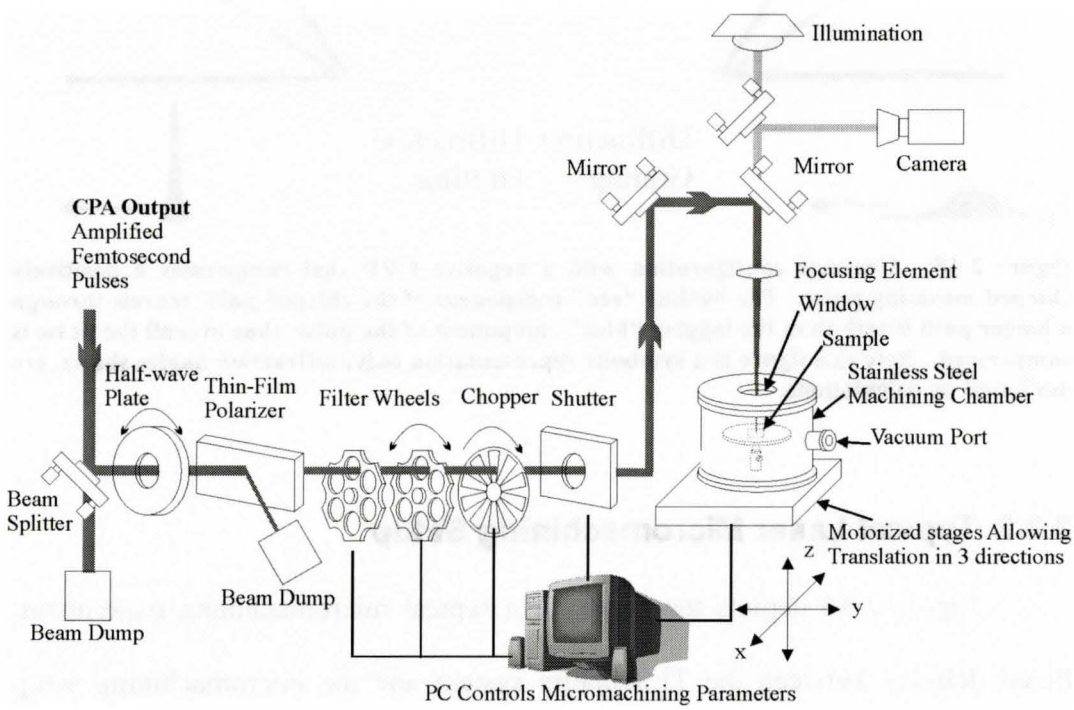

Figure 2-16: A typical ultrashort pulse laser micromachining setup employed for experiments described in this thesis.

pulse energy) a mirror is used in place of the beam splitter A beam dump is used to capture the part of the split beam that is not used. The purpose of the beam dump is to collect the unused portion of the laser pulses to prevent having a stray

beam across the optical bench. Two computerized filter wheels house metallic-coated neutral density filters with different optical densities (O.D., where transmitted power $P_{out} = P_{in} \times 10^{-O.D.}$). The combination of different filters in the filter wheels allow pulse energies to be controlled by the computer during an experiment. A mechanical chopper and shutter are used to control the number of pulses that are incident on the sample surface. The chopper is needed to reduce the repetition rate of the laser pulses to 50 Hz, since the shutter requires more than 1 ms (corresponds to 1 kHz laser repetition rate from the Ti:Sapphire system) to switch from fully opened state to fully closed, and vice versa. Another series of mirrors steer the beam so that the beam arrives vertically at the micromachining platform on which the sample is situated. The platform is secured down inside the micromachining chamber which is equipped with a vacuum port that allows experiments to be performed under vacuum as to reduce the amount of debris from laser processing which redeposits on the sample surface. The mechanical roughing pump is vented directed to a fume hood system. The micromachining chamber is made of 6 mm thick stainless steel to attenuate x-rays that could be produced during the micromachining process [36]. It is mounted on two motorized translation stages to allow movement in the x- and y-directions. This is useful for cutting features such as grooves and gratings. A focusing optical element (i.e. a lens or a microscope objective) is used to focus the beam on to the sample surface. This optical element is also mounted on a motorized translation stage to allow movement in the z-direction.

Additional metal shielding, made of ¼″ thick steel, is placed around and above the micromachining chamber to attenuate x-rays that may leak through the chamber or out through the window of the chamber Under normal operating conditions only medically soft x-rays are expected to be generated. The shielding is intended to be greatly over-designed.

To provide a visualization of the setup employed in the laboratory, a photograph of some of the optical components illustrated in Figure 2-16 are presented in

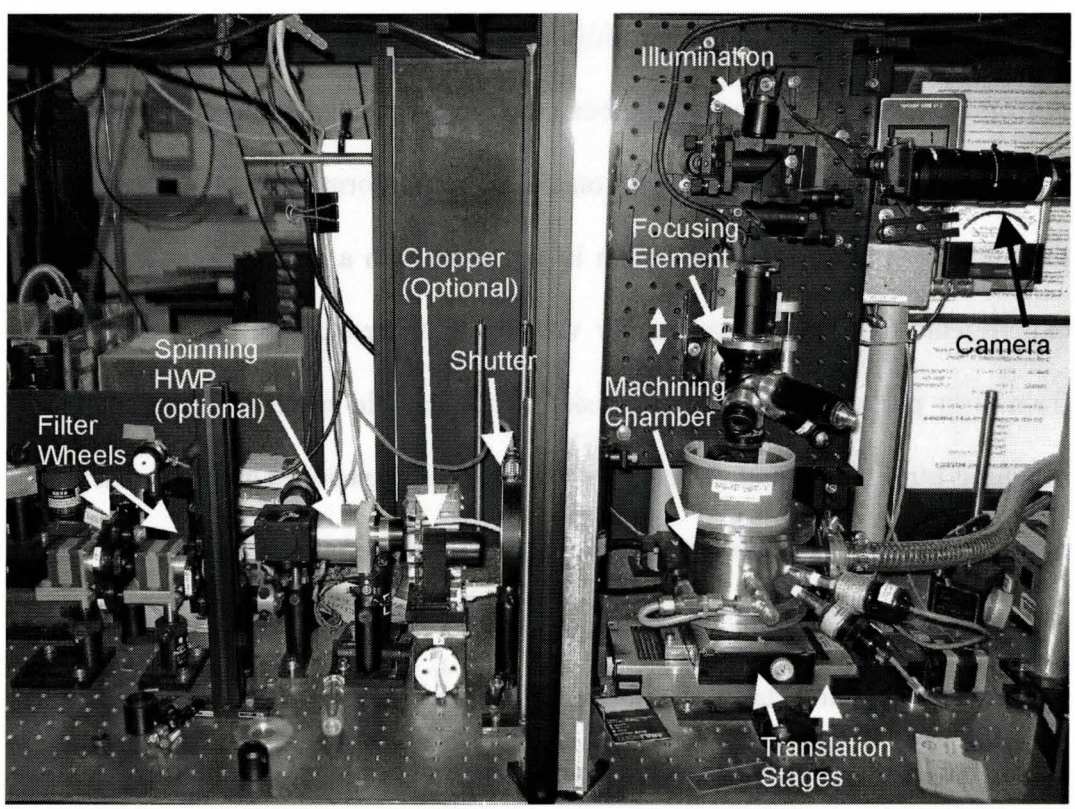

Figure 2-17: Photograph of some of the components used in the ultrashort-pulse laser micromachining setup.

2.3 Beam Measurement and Diagnostic

This section of the thesis describes techniques employed for the characterization of the femtosecond laser pulses. A challenge posed by the ultrashort pulses is that the pulse duration is much shorter than the response time of electronic diagnostic equipment.

2.3.1 Pulse Duration

Autocorrelation is one of the techniques to measure pulse durations of short pulses [37, and references therein]. Most of the pulse durations quoted in this thesis are measured using a non-collinear second-order autocorrelator. Figure 2-18 depicts such a setup. Incoming pulses are divided into two separate paths through the use of a beam-splitter. Two retro-reflection mirrors are used to direct the beams back to the beam splitter. One of these mirrors is mounted on a motorized translation stage to create an optical delay line. The two pulses are steered by the beam-splitter again towards a converging lens on parallel beam paths. The lens directs the pulses such that they will cross one another at the focal region of the lens.

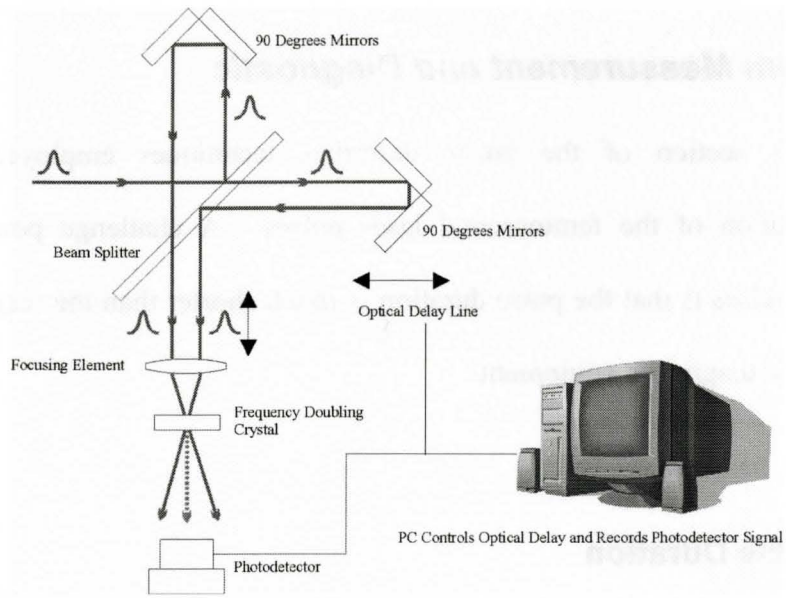

Figure 2-18: A second-order non-collinear autocorrelator. The dashed-line represents pulses that have been frequency-doubled.

A frequency-doubling crystal is placed at the focal region of the lens where the two pulses overlap. Frequency-doubled pulses will be produced collinearly to the incident pulses. Via conservation of momentum arguments, when the two pulses overlap another frequency-doubled pulse will also be produced in the direction that is between the two paths of the incoming pulses [35], as presented by a dash line in Figure 2-18. This frequency-doubled pulse strikes a photodetector where its energy is monitored. The intensity of the on-axis frequency-doubled pulses is a function of the amount of "overlap" in time of the two incoming pulses. By changing the length of the optical delay line, one pulse is shifted past another in time. The change in the signal from the photodetector can be correlated to the known delay of the two pulses, as calculated by the

change in distance; the duration of the original incoming pulse thus can be deduced.

Considerations need to be given to the material and thickness of the frequency doubling crystal used in the autocorrelator. Different materials might be more efficient at frequency doubling, but may not provide a phase matching bandwidth required for laser pulses with a large range of spectral components. A thicker crystal provides a longer length of medium over which frequency conversion takes place, resulting in more of the energy in the fundamental pulses converted to the frequency-doubled pulses. However, thicker crystals also provide a narrower phase-matching bandwidth [37]. The phase-matching bandwidth for a crystal with thickness L is given by the equation [37]:

$$\delta\lambda_{FWHM} = \frac{0.44\lambda_o / L}{\left| n'(\lambda_o) - \frac{1}{2} n'\left(\frac{\lambda_o}{2}\right) \right|} \qquad (2\text{-}3)$$

Where $\delta\lambda_{FWHM}$ is the full-width-half-max phase-matching bandwidth, and $n'(\lambda)=dn/d\lambda$. The derivation of this equation is provided in [37].

Another use of the autocorrelator is to detect satellite pulses. For example, due to multiple reflections a secondary pulse closely spaced (in time) to the primary pulse can be generated in optical elements. If this happens in the CPA cavity, the secondary pulse can be amplified as well. This could influence the resulting morphology of laser ablated materials. For example, in a "single pulse" experiment a sample can potentially be irradiated by the main pulse followed by the satellite pulses. This effect of the satellite pulses on surface morphology may

be subtle or insignificant for a lot of our work since we are mainly interested in studying the physics near the ablation threshold. When the main pulse has a pulse energy near the ablation threshold, it should be reasonable to assume the satellite pulses to have energies well below the threshold. Figure 2-19(a) presents autocorrelation results of a "clean" autocorrelation trace of a pulse where no unwanted features are evident, and Figure 2-19(b) shows a trace where satellite pulses are detected. Under typical operating conditions, satellite pulses are not expected to occur. Satellite pulses shown in Figure 2-19(b) resulted from a poorly aligned intracavity element in the Ti:Sapphire regenerative amplifier following cavity tests performed prior to this autocorrelation measurement.

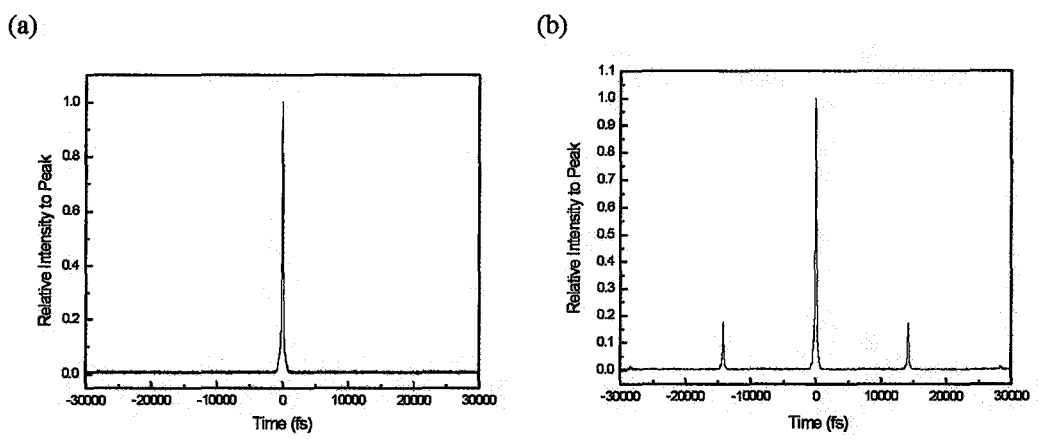

Figure 2-19: Examples of autocorrelation traces. (a) A "clean" autocorrelation trace with low background noise, and (b) An autocorrelation trace where satellite pulses are observed.

On a regular basis, GRENOUILLE (GRating-Eliminated No-nonsense Observation of Ultrafast Incident Laser Light) is also used to characterize the pulse duration. Details of GRENOUILLE are provided in section 2.3.4.

2.3.2 Pulse Spectrum

The spectrum of the laser pulses is examined using an Ocean Optics PC2000 Spectrometer. The spectrometer has an optical fiber input. Scattered light off a piece of white paper provides more than adequate signal to monitor and record the spectrum on a computer.

As a precautionary measure, the spectrum of the seed pulses from the Ti:Sapphire oscillator is characterized prior to seeding them into the CPA. Since the pulse stretching in the CPA relies on spreading the spectral components of the pulse spatially, not having a wide enough bandwidth in the seed pulses might cause inadequate stretching and resulting in high intensity pulse being seeded into the amplifier. While there is a bandwidth detector built in to the CPA that stops the amplifier operation if a wide bandwidth is not detected, this precautionary step adds another layer of protection.

Figure 2-20 shows a screen capture of the Ocean Optics Spectrometer software, presenting a typical spectrum of the output pulses from the Tsunami Ti:Sapphire oscillator.

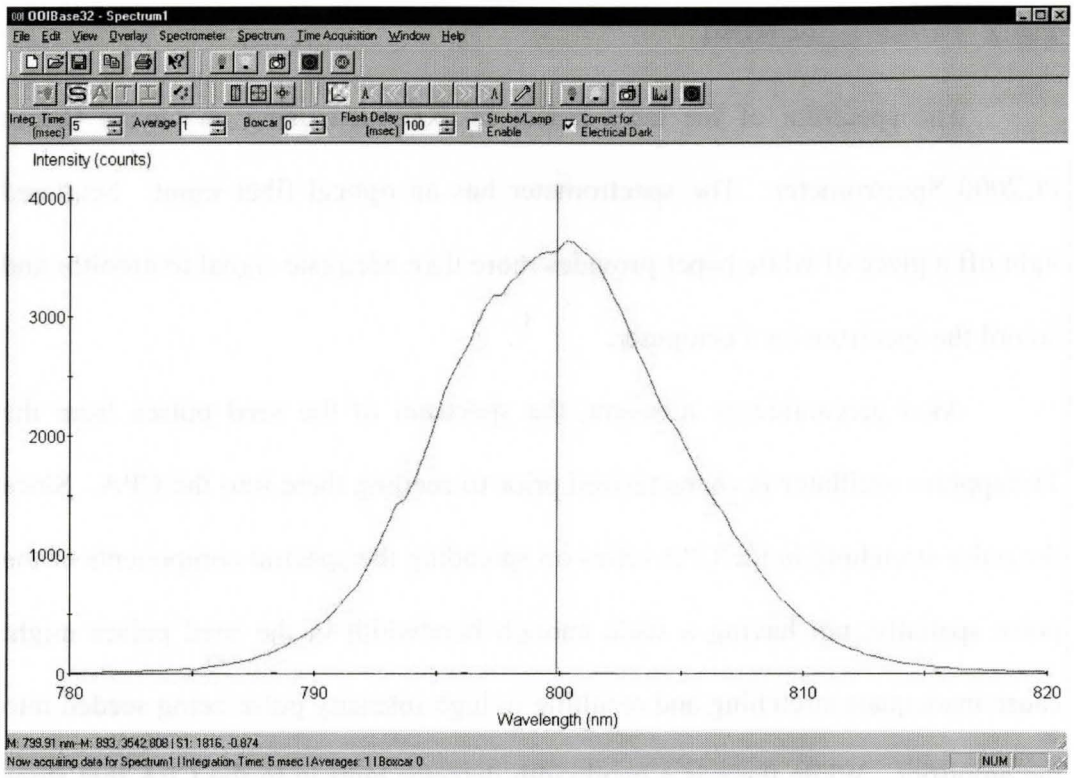

Figure 2-20: Screen capture of Ocean Optic PC2000's software. Shown here is a typical spectrum data from the Tsunami Ti:Sapphire oscillator. The pulses generally have a central wavelength of 800 nm, with a 10 nm FWHM bandwidth.

On several occasions an Ocean Optics USB2000 spectrometer was used to record the spectrum of pulses. This spectrometer does not require an optical fiber linkage between the spectrometer and the computer Instead, an USB cable is used. The advantage of not using optical fiber is that it eliminates the chances of artifacts which can result from coupling light into the fiber

The use of a second spectrometer, along with (infrequently) a Jobin Yvon HRS2 monochromator and an Ando AQ 0315E Optical Spectrum Analyzer, act to confirm the calibration of each of the spectral monitoring and recording instruments employed.

2.3.3 Beam Profile

The spatial profile of the beam is characterized in each experiment prior to the laser ablation and micromachining work, typically with an OPHIR BeamStar silicon CCD beam profiler In most cases the beam profile has approximately a Gaussian intensity distribution and is close to circular, although, minor degree of asymmetry is generally observed.

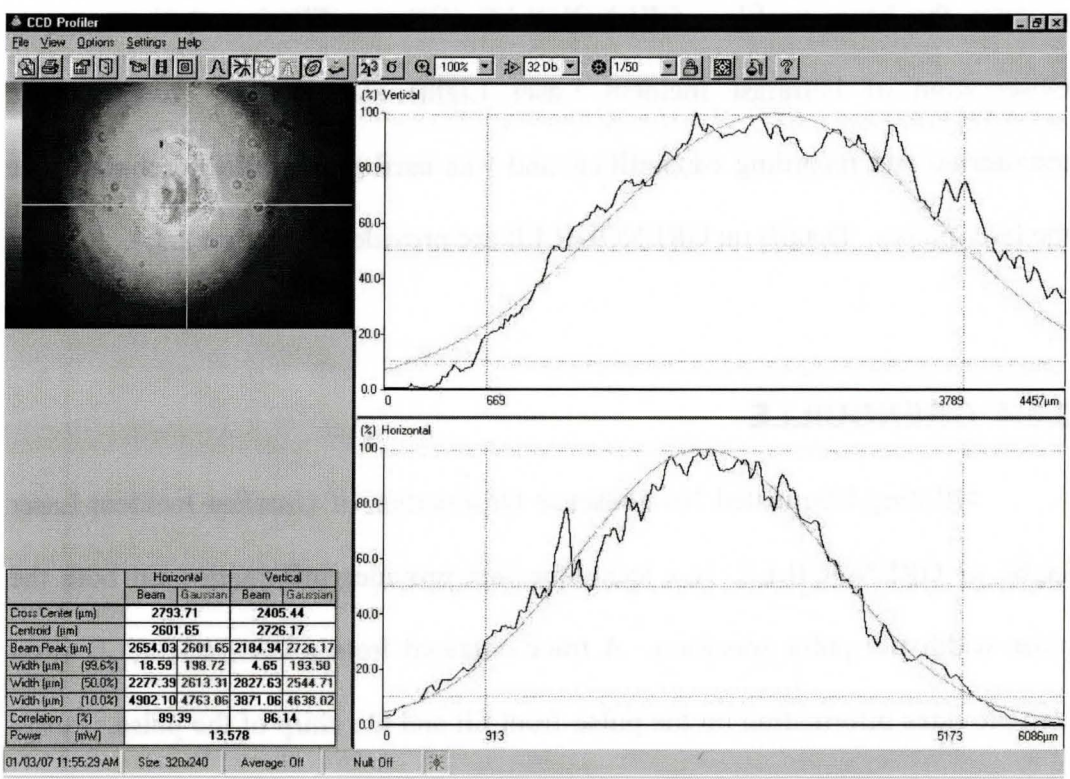

Figure 2-21: Screen capture of BeamStar OPHIR software that is used to characterize and record the beam profile. The overall beam profile (top left corner) shows that the beam is mostly circular with some ellipticity. The two traces on the right are line traces of vertical (top) and horizontal (bottom) sections, and should approximate a Gaussian intensity distribution in space.

Figure 2-21 shows a screen capture of the BeamStar OPHIR CCD beam profiler software, presenting a typical beam profile of the output pulses from the CPA. In this particular image dust and debris on optical elements is evident, indicated as rings and speckles in the profile image. The irregularity (i.e. spiking) of the traces may arise from dust on optics farther away from the machining setup, or damaged optical elements such as gratings or Pockels cells in the regenerative amplifier.

On a few occasions another OPHIR BeamStar CCD camera was used to monitor the beam profile. GRENOUILLE (GRating-Eliminated No-nonsense Observation of Ultrafast Incident Laser Light) also provides beam profile monitoring and recording capabilities, and was used periodically to characterize the laser pulses. Details on GRENOUILLE are provided in section 2.3.4.

2.3.4 GRENOUILLE

GRating-Eliminated No-nonsense Observation of Ultrafast Incident Laser Light, or GRENOUILLE, is a technique that provides information on both the pulse width and pulse spectrum. A trace obtained from a GRENOUILLE setup also provides information on the pulse-front tilt and the chirp of the pulse. Pulse-front refers to the contours of constant intensity [37]. In a pulse with a tilted pulse-front, the axes of the constant intensity are neither parallel nor perpendicular to the propagation direction [37]. For ultrafast pulses, where the pulses are a few to a few tens of micrometers in space, a tilted pulse-front can

have a significant effect in the pulse duration measured using an autocorrelator. Figure 2-22 presents a symbolic representation of a GRENOUILLE setup. It is based on the Frequency Resolved Optical Gating (FROG) technique (details of FROG is not discussed in this thesis), but with a simplified setup such that it has far less optical elements. The discussions on GRENOUILLE in this section are based on [37].

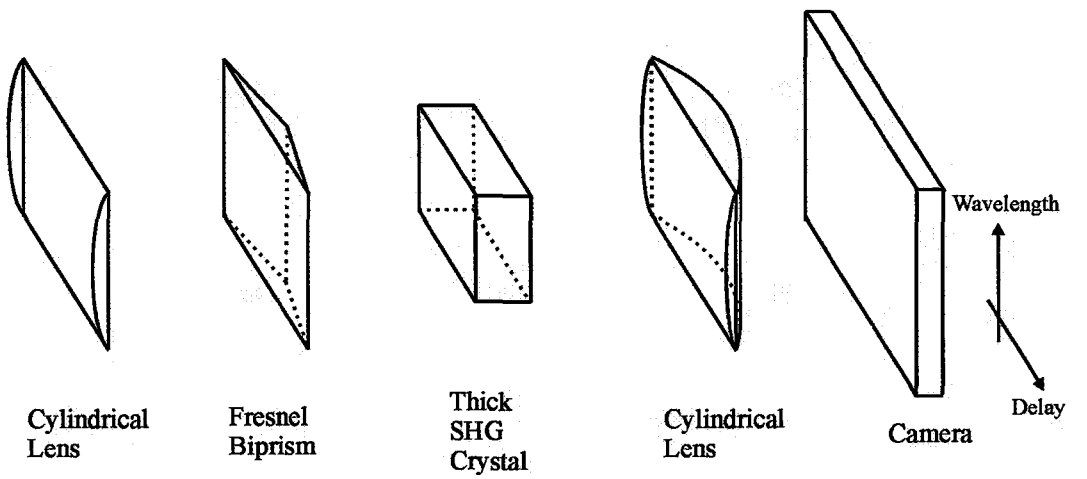

Figure 2-22: A GRENOUILLE setup, which can provide information on pulse width, pulse spectrum, pulse-front tilt as well as chirp in laser pulses. The vertical axis of the trace obtained on the camera provides spectral information about the pulse, whereas the horizontal axis provides information on the relative delay (time) information.

A beam splitter splits off a small portion of the incoming pulse energy for projection onto a second camera so the beam profile and alignment can be monitored (not shown).

The operation of the GRENOUILLE setup is best illustrated by examining the time and spectral diagnostic components separately. Figure 2-23 is a side view of the GRENOUILLE setup. An incoming beam is focused through the

thick second harmonic generation (SHG) crystal via a cylindrical lens. Equation (2-3) indicates a narrow phase-matching bandwidth for a thick SHG crystal. The narrow phase-matching bandwidth provides a spatial separation of the converted spectral components, much like a grating. A second cylindrical lens is used to collimate the output of the SHG crystal and project it on to the camera. The vertical axis of the trace obtained from the camera thus shows the spectral information of the incoming pulse. The camera is sensitive to the intensity of the incident beam, and in a GRENOUILLE trace the intensity distribution can be displayed as false-color

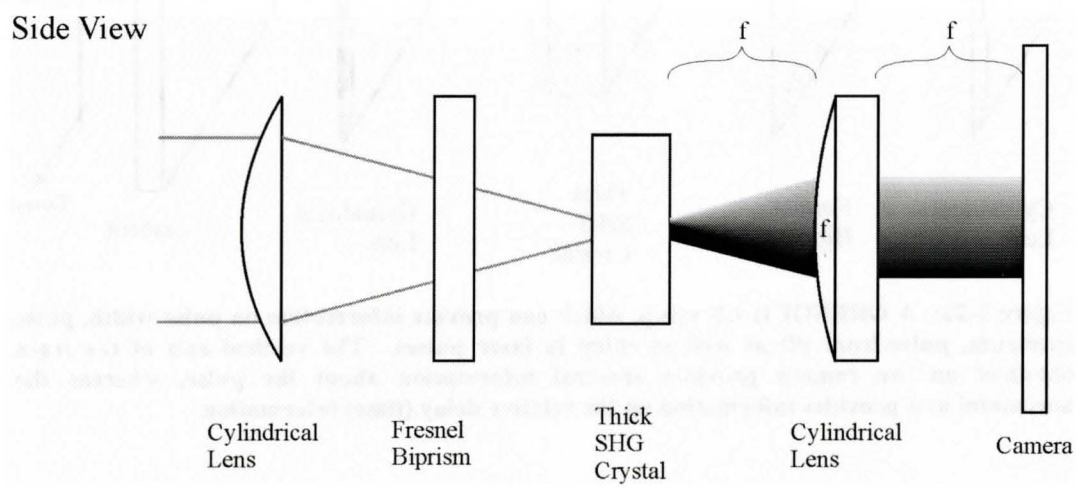

Figure 2-23: Side view of a GRENOUILLE setup. The non-shaded regions represent the (incoming) fundamental beam. The shaded regions represent frequency-doubled beam, in which the different shading represent different spectral components in the beam. These parts of the GRENOUILLE setup act as a spectrometer.

Figure 2-24 presents a top view of the GRENOUILLE setup. An incoming beam is split into two beamlets which cross in the SHG crystal. In this respect the Fresnel biprism acts as the beam splitter, delay line and combiner By

using a Frensel biprism, the optical setup is simplified and both temporal and spatial overlapping of the two beamlets is achieved automatically As the beamlets passes each other in the SHG crystal, a second-harmonic beam is generated. Due to the beamlets crossing each other at an angle, it has an overall effect of one pulse slipping past the other in time, much like the case in the autocorrelator However, in the case of GRENOUILLE the time delay information is also separated spatially, and this information is imaged on to the camera with a cylindrical lens. Spatial intensity distribution is represented as false-color on a GRENOUILLE trace.

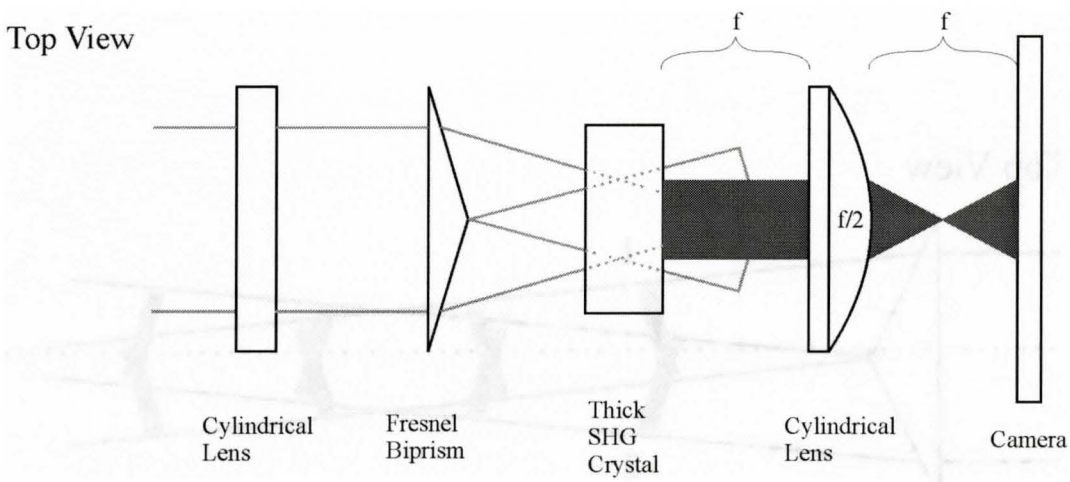

Figure 2-24: Top view of a GRENOUILLE setup. The non-shaded regions represent the (incoming) fundamental beam. The shaded regions represent frequency-doubled beam. These parts of the GRENOUILLE setup act as an autocorrelator.

Figure 2-25 demonstrate that two beamlets crossing at an angle having an overall effect as two pulses slipping past one another in time, similar to the case in an autocorrelator setup. Also shown is the dependence of the horizontal position on the relative delay between the two pulses. Based on this diagram, one can

visualize that distortions such as pulse-front tilt and spatial chirp (variation of wavelength in space) can be detected using GRENOUILLE as well. For example, a tilted pulse front will cause asymmetry of the two pulses in the beamlets, causing the region with the most intense second harmonic generated to be off center on the camera. If the pulse has a spatial chirp, a (horizontal) spatial gradient will be produced in the frequency-doubled beam. Along with the spectrometer function of the GRENOUILLE (note that the spectral components are displayed on the vertical axis of the trace), spatial chirp will cause a GRENOUILLE trace to be tilted.

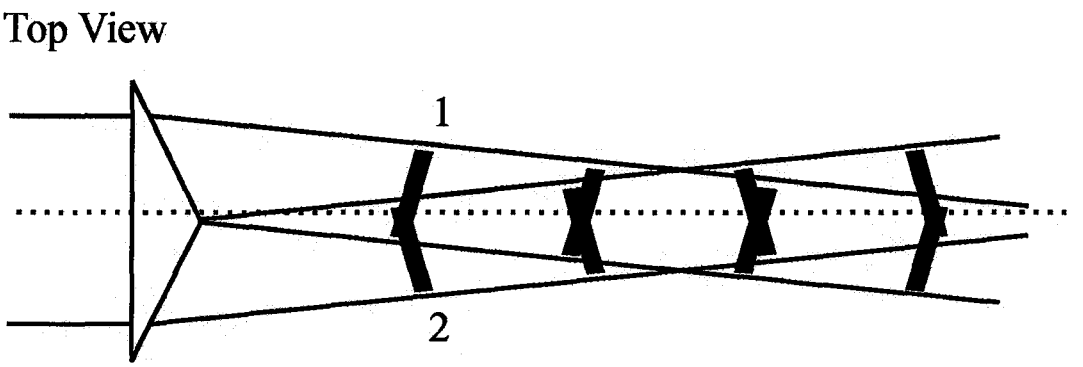

Figure 2-25: A Fresnel biprism creates two intersecting beamlets. The solid lines show the beam paths of the incoming beam and the two beamlets. The black slices represent pulses crossing each other at different time frames.

2.3.5 Tilted Pulse-Front Autocorrelator

A Light Conversion Ltd. tilted-front-pulse autocorrelation (TFPA) is infrequently used to check the pulse duration and the tilt of pulse-front.

Discussions of TFPA are based on [38] and [39]. A TFPA is based on a modified second-order noncollinear autocorrelator (refer to Section 2.3.1 for details of a second-order noncollinear autocorrelator), where one of the two beams undergo an extra reflection, thus when the two beams overlap in the crystal they are spatially inverted.

To demonstrate the effect of a tilted pulse-front on an autocorrelation trace, first consider a typical second-order non-collinear autocorrelator, as shown in Figure 2-26 (where yz-plane represents the vertical plane). Since the pulses cross at an angle, positions along the y-axis (vertical axis on the CCD camera) contain relative time-delay information between the two pulses. The resulting autocorrelation trace on the CCD camera is an ellipse with its major axis along the x-axis [39].

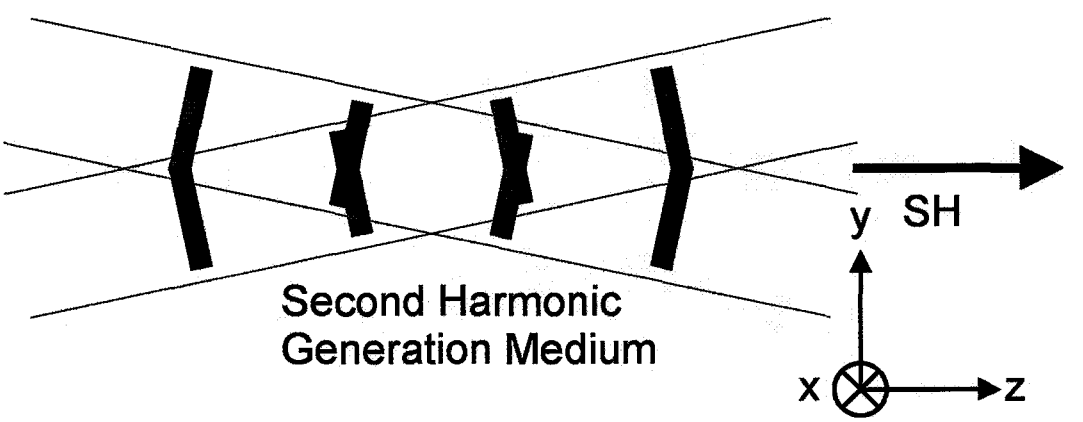

Figure 2-26: Side views of two beams crossing in a tilted-pulse front nonlinear autocorrelator. An on-axis second harmonic beam is generated as the two pulses cross in a second harmonic generation medium.

Typically a misaligned CPA compressor introduces a pulse-front tilt in the horizontal plane (i.e. tilted about a vertical axis) [39]. Figure 2-27 shows a symbolic representation of a tilted pulse crossing with its spatially inverted replica in the horizontal (xz-) plane. When a pulse-front tilt exists, the overlapped region will move along the cross-section of the pulses as they scan past one another, and the resulting scan on the camera will be a tilted ellipse. The amount of pulse-front tilt, in degrees, can be correlated to the amount of tilt of the autocorrelation trace [39].

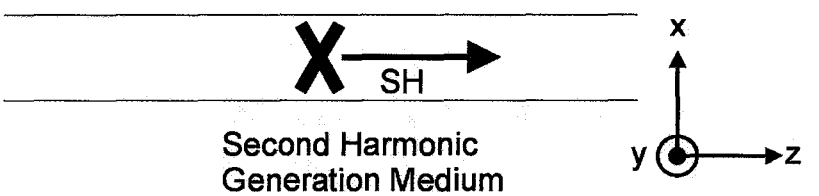

Figure 2-27: Top view of the second-harmonic generation crystal in a tilted-pulse front autocorrelator, showing the crossing of two tilted pulses.

A TFPA is useful for measuring pulse-front tilt and is an alternative to the GRENOUILLE.

Chapter 3 Experiment: Investigation of Laser Induced Periodic Surface Structures (LIPSS)

3.1 Introduction

Laser induced surface ripples, or sometimes referred to as Laser Induced Periodic Surface Structures, or LIPSS, were first observed over four decades ago [38]. The spatial periods of LIPSS formed due to interference of scattered waves on the account of surface roughness waves are typically described by the following equations [14]:

$$\Lambda = \frac{\lambda}{1 \pm \sin\theta} \qquad (3\text{-}1)$$

for reflected wave from the material surface, and

$$\Lambda = \frac{\lambda}{n \pm \sin\theta} \qquad (3\text{-}2)$$

for scattered wave transmitted into the material, where Λ is the spatial period of the ripples formed on the surface, λ is the wavelength of the incident laser light, n is the refractive index of the material and θ is the angle of incidence of the laser with respect to the surface normal of the sample.

Aside from the interference pattern due to surface scattered wave, surface electromagnetic wave (SEW) can also contribute to ripple formation. Ripple formation is the most pronounced if one of the surface electromagnetic wave is in

resonance with the scattered surface waves. The following equations describes the spatial periods of the ripples caused by SEW [14]:

$$\Lambda \approx \frac{\lambda}{1 \pm \sin\theta} \qquad (3\text{-}3)$$

for incident electric field in the plane of incidence, and

$$\Lambda \approx \frac{\lambda}{\cos\theta} \qquad (3\text{-}4)$$

for incident electric field perpendicular to the plane of incidence. The above equations are simplified from exact expressions based the assumption that the refractive index of the SEW, n_{SEW} is approximately 1 [14].

Due to the wide range of laser conditions and materials that these LIPSS are observed to appear under, they are considered to be a universal phenomenon [41-43]. The origin of these LIPSS is attributed to the interaction between the incident light with scattered light on the surface of the material, creating an interference effect [41, 44].

In the more recent history of laser-material interactions, research groups have been reporting LIPSS with spatial periods substantially smaller than the wavelength of irradiation laser pulses on a variety of materials when irradiated under certain laser conditions [45-57]. More specifically, multiple-pulse irradiation with incident laser wavelength corresponding to below-bandgap energy of the material is typically the required irradiation conditions for HSFL to form [45, 48-50]. Due to their small physical dimensions relative to the wavelength of the incident laser pulses, we have referred to them as High Spatial

Frequency LIPSS, or HSFL in previous work [49, 50]. In contrast, the classic ripples with spatial periods close to the irradiation wavelengths have been referred to as Low Spatial Frequency LIPSS, or LSFL. The exact formation mechanism of HSFL is still under debate in the current literature. Some of the proposed HSFL formation mechanisms include self assembly of the material surface [46, 52-54], nonlinear interaction at the material surface [45, 47, 49, 50, 55, 56], and extensions [57, 58] of existing theory [41-43]. Coulomb explosion has also been attributed to the formation of nanostructures [59].

Studying the structures of HSFL after a material is exposed to different irradiation conditions can yield insights into the origin of HSFL. This chapter of the thesis describes experiments performed to investigate the effect of some irradiation conditions on the formation of HSFL. The subsections of this chapter are divided based on the irradiation conditions and the material of the irradiation targets. For convenience, discussions and comparison of the experimental results from all the LIPSS experiments presented in this thesis with literature reports will be presented collectively in a separate subsection.

3.2 LIPSS on Gallium Phosphide: Study of LIPSS Structures

3.2.1 Introduction

Gallium Phosphide (GaP) is a suitable material for our investigation since it is a III-V semiconductor much like indium phosphide that we have studied by our group previously [48, 49], and it has a bandgap of 2.26 eV, corresponding to a wavelength of 549 nm [59]. Since HSFL typically form when the material is irradiated with laser pulses having wavelengths corresponding to below bandgap photon energies, the output of our Ti:Sapphire systems at 800 nm can be used directly for HSFL investigation experiments without having to perform frequency conversions to obtain longer wavelengths using an optical parametric amplifier, which would increase the complexity of the experimental setup.

3.3 LIPSS on Gallium Phosphide: Effect of Pulse Duration

3.3.1 Introduction

Since non-linear effects are sensitive to the intensity of the incident laser pulses, it is possible to test the role of non-linear interactions as the origin of HSFL formation by irradiating the sample with pulses of different intensities. One way to obtain a large range of pulse intensities is to vary the durations of the output pulses of the CPA.

Selected data and figures from this section appear in a recent publication by our group and are reprinted with permission [60] (Copyright 2007, American Institute of Physics).

3.3.2 Experimental Setup

The setup for this experiment was mostly identical to the general setup described in Chapter 2.2.2. However, two different commercial Ti:Sapphire ultrashort-pulse laser systems were used to obtain a wider range of pulse durations. One of the two systems delivered pulses with a beam profile that was more elliptical than circular. The goal of this experiment was to obtain a qualitative and semiquantative survey of the formation of LIPSS, thus the beam shape in the one case not being circular should not be a significant issue. Pulse durations were varied by adjusting the compressors in the CPAs [61]. With access to the two systems, pulse durations from 50 fs to 7 ns can be obtained. In this experiment, pulse durations employed were 150 fs, 500 fs, 1 ps, 5 ps, 10 ps, 20 ps, 40 ps, 60 ps, 80 ps, 130 ps, 220 ps and 7 ns, corresponding to a intensity range of over five orders of magnitude. Pulse durations were measured using a second-order non-collinear autocorrelator. To ensure the pulses were phase-matched in the second-order generation (SHG) crystal in the autocorrelator, different SHG crystals were used to confirm the autocorrelation results, including 150 μm and 50 μm thick beta barium borate crystals. For longer picosecond pulses, a New Focus 1454-50 fast photodiode and a Tektronix CSA 803

communications signal analyzer were also used to confirm the calibration of the autocorrelator. Pulse durations of the ns-pulses were measured using a fast silicon PIN photodiode with a rise time of 1 ns. With each pulse duration, the number of pulses per irradiation site N employed includes 1, 5, 10, 20, 50, 100, 200, 500 and 1000, and pulse energies ranged from 2 μJ to 7 nJ. For irradiation with 150 fs pulses, N was subsequently increased to 2000, 5000, 10 000 and one million to further study the behavior of HSFL at very high N. Irradiation was performed on double-side polished gallium phosphide (100) samples with a thickness of ~ 430 μm, an n-doping of 1.85×10^{16} a/cm^3 and a mobility of 160 cm^{2}V^{-1}s^{-2}. The laser pulses were focused perpendicularly to the sample surface with a 5× microscope objective, yielding a spot size of ~ 5 μm $1/e^2$ radius as extracted using the D^2 technique [62]. The D^2 technique for the extraction of laser spot size and threshold fluence is discussed in the paragraph below. Irradiation was performed in rough vacuum (~ 0.05 mbar). The pressure was monitored using a Kurt J. Lesker Co. KJL-902002 digital vacuum gauge connected to a port on the micromachining chamber. Irradiated sites were studied using Nomarski optical microscopy (OM) and scanning electron microscopy (SEM). It should be noted that LIPSS observations reported in this section of the thesis were limited to features observable under optical and scanning electron microscopy; observation of deeper regions in some craters were not possible. Calibration of lengths in SEM images were checked from time to time using known distances on samples (i.e. ablation craters with known spacings can

provide an approximate check, also calibration test specimens were available from Canadian Centre for Electron Microscopy, where all the microscopy works were carried out).

A technique to determine the spot size of the laser pulses and the threshold fluence is to measure the diameter of the ablated craters and correlate that to the known laser energy used for that specific crater. The relationship between the diameter and the pulse energy is given by [62]:

$$D^2 = 2\omega_o^2 \ln\left(\frac{E}{E_{th}}\right) \qquad \textbf{(3-5)}$$

where D is the diameter of the ablated crater, ω_o is the $1/e^2$ radius of the incident spot, E is the pulse energy used for each specific crater, and E_{th} is the threshold fluence for the material. This technique is referred to as the "D^2 technique".

3.3.3 Results and Discussions

The D^2 technique was employed in attempts to extract spot size and threshold fluence information for all N and pulse durations. However, we have concluded that a simple D^2 model might not be applicable to all the different N and pulse durations employed in this experiment due to the intricate and possibly different physics when these parameters are varied. For instance, this model appears to be suitable for single-pulse irradiation and may not take properly into account the incubation effect, where the ablation threshold fluence decreases as higher N is used [e.g. 63, 64]. Also, the behavior of the heat affected zone and

mechanisms for material removal are not the same as the pulse duration increases [12-14], creating further uncertainty in the D^2 model. Debris and material redeposition also made measurements of craters diameter difficult. Around each ablation crater there typically is a rim. For irradiation with higher N or higher fluences, the amount of material removed is increased and the amount of debris and redeposited material also increases. The redeposited material can make identification of the edges of the rims difficult. In addition, as the pulse duration increases, a greater amount of melting is expected (refer to Section 2.1 for comparison of ablation mechanisms with different pulse durations). As a result, the size and appearance of crater rims vary when irradiated with different pulse durations, further increase the uncertainty in measurements of the crater diameters. Keeping track of the same ablation features as well as obtaining an accurate and consistent spot size for the large range of N and pulse durations employed in this experiment was challenging. Figure 3-1 presents spot sizes extracted using the D^2 technique for $N = 1$ and $N = 1000$ at selected pulse durations employed in this experiment. Aside from the 220 ps and 7 ns cases where the geometry of the CPA were changed, the other pulse durations presented in this figure would be expected to have almost the same spot size regardless of the pulse durations or N. In light of this difficulty, irradiation energies where visible damage is still observed with optical and/or electron microscopy are used as an indicative value for threshold energies (instead of using the D^2 technique to determine the ablation threshold fluences).

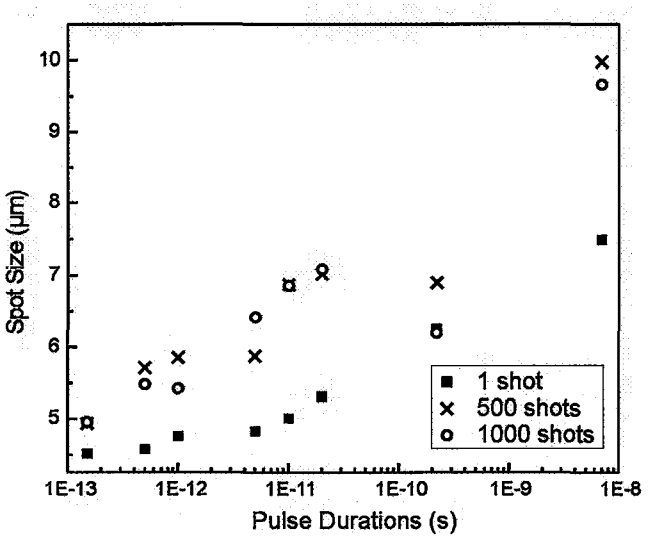

Figure 3-1: Spot size extracted using the D^2 technique for N = 1, 500 and 1000 at selected pulse durations.

In terms of LIPSS observations, in all cases LIPSS were observed to run perpendicular to the direction of the electric field of the incident pulses. Also, no LIPSS were observed on any single-shot irradiated sites. In general, it was observed that for a given N, HSFL tend to be generated at low fluences. Also, for a given fluence, HSFL tend to be generated at higher N. Observation of LIPSS in deeper regions of irradiated sites was limited by the capability of the microscopy techniques to resolve the details in such depth.

Sites irradiated with 150 fs pulses were studied thoroughly as a preliminary observation since they were irradiated with a pulse duration comparable to those employed in the studies in the literature where HSFL were observed [45-57]. At this pulse duration, LSFL were readily observed at N = 5.

Although no obvious HSFL were observed at $N = 5$, fine bumps were observed at the periphery of sites where LSFL occupy the central region (Figure 3-2). At a very low pulse energy, where we suspect only surface amorphization took place, hints HSFL pattern was observed (Figure 3-3).

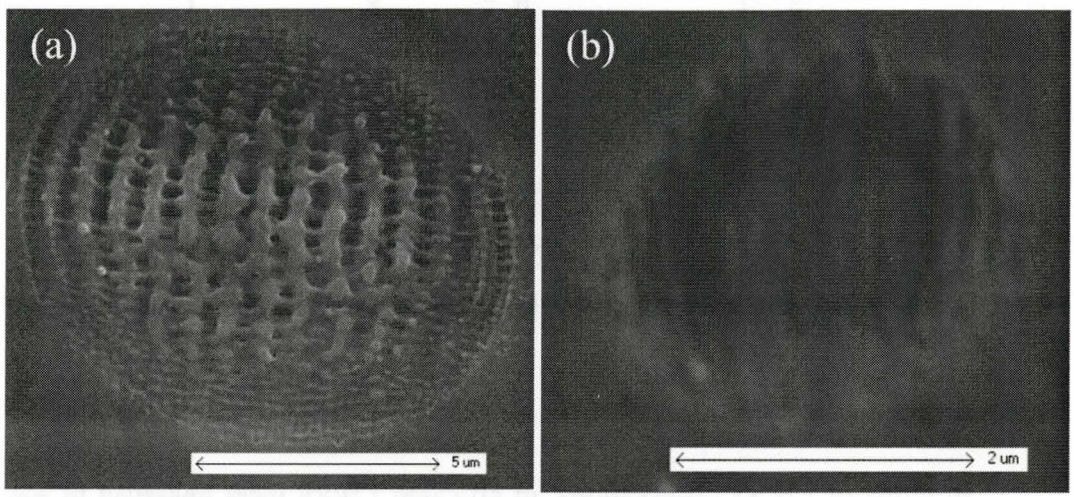

Figure 3-2: SEM images of sites irradiated with 5 pulses at 150 fs, and a pulse energy of (a) 364 nJ, and (b) 68 nJ. (a) At 364 nJ, fine bumps are observed at the periphery of the site where LSFL are observed in the central region. (b) At 68 nJ, LIPSS pattern are observed on regions that are suspected to just have been amorphized. The poor contrast in (b) is likely due to the subtle nature of the surface modification.

At $N = 10$ HSFL were observed at the periphery of sites where LSFL were observed at the central region. First impressions on the SEM images suggest that at $N = 10$ HSFL (Figure 3-3(a)) were formed near regions where the fine bumps were observed for $N = 5$ (in comparison to Figure 3-2(a)).

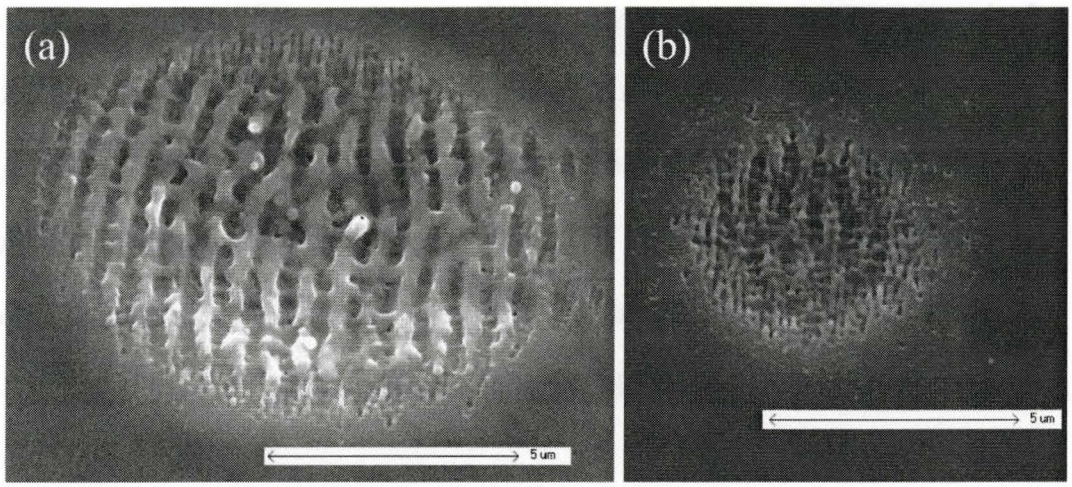

Figure 3-3: SEM images of sites irradiated with 10 pulses at 150 fs and a pulse energy of (a) 280 nJ, and (b) 115 nJ. In (a), HSFL are observed at the periphery of the site where LSFL are observed in the central region. The locations of HSFL roughly corresponds to the locations of the fine bumps when irradiate with $N = 5$. Refer to Figure 3-2(a) for comparison. The site shown in (b) is the only instance in which we observed both HSFL and LSFL are superimposed.

As N increases further, regions occupied by HSFL extended toward the central portion where LSFL was observed for lower N Only HSFL were observed for sites irradiated with $N \geq 150$. The spatial period of LSFL decreased from ~680 nm to ~520 nm as N increased from 5 to 40. Similarly, HSFL spatial period decreased from approximately 175 nm to 150 nm when N was increased from 50 to 1000. However, a subsequent experiment showed no further decrease in HSFL spatial periods when N was increased to 10 000. The decrease of HSFL spatial frequency with increasing N has been previously reported in the literature [45].

To investigate the effect of pulse durations and pulse intensity on the formation of HSFL, pulses with durations of 500 fs, 1 ps, 5 ps, 10 ps, 20 ps, 40 ps, 60 ps, 80 ps, 130 ps, 220 ps and 7 ns were also used to irradiate the GaP samples.

In the range of pulse durations where HSFL were observed, higher N was required for HSFL to form as the pulse duration increased. Figure 3-4 presents examples of LIPSS observed at 150 fs and 20 ps to demonstrate the LIPSS evolution with varying N and pulse energies. The behavior of LIPSS as the pulse duration increases can be demonstrated by comparing the LIPSS distribution when irradiated with 150 fs pulses with 20 ps pulses (Figure 3-5).

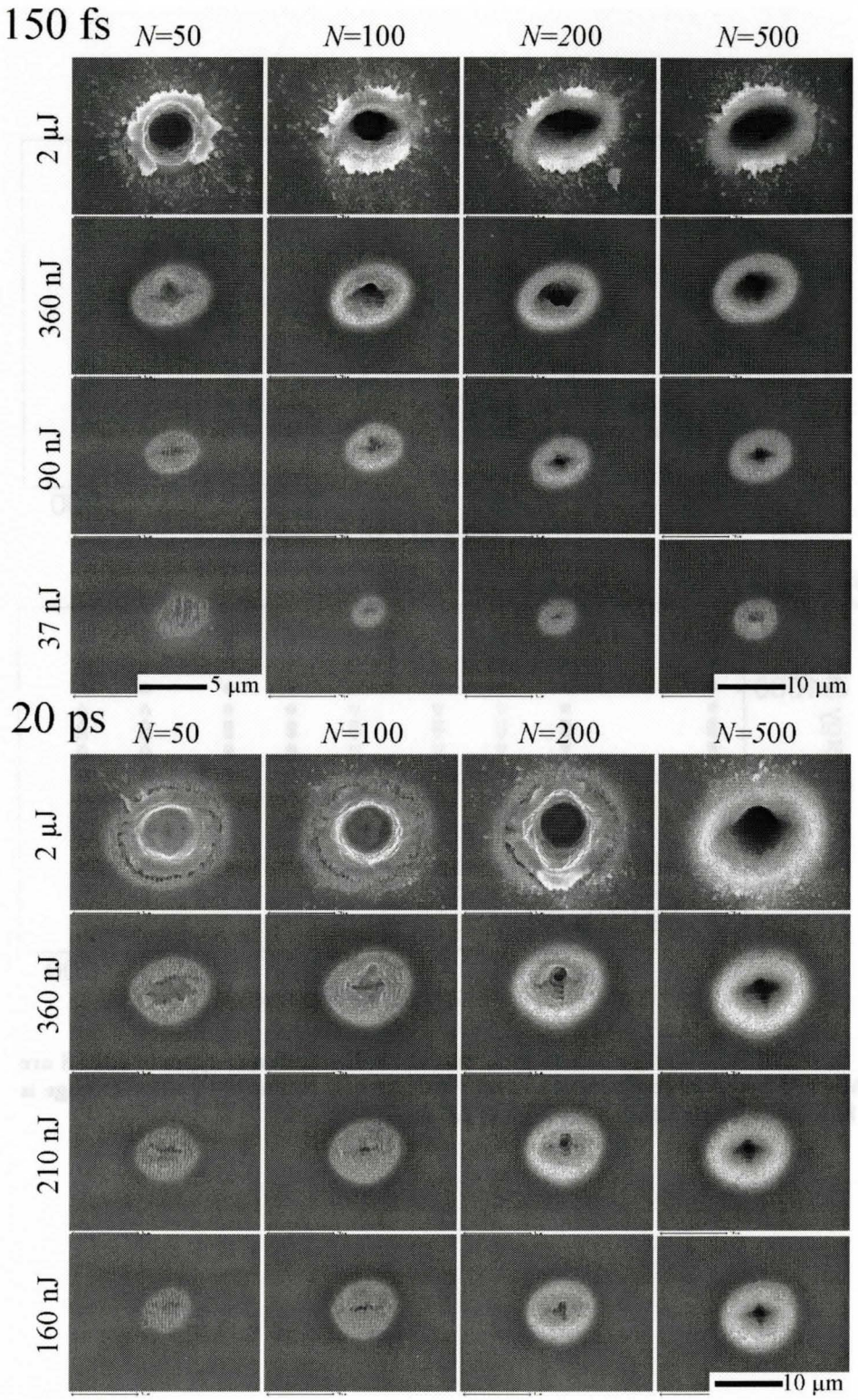

Figure 3-4: LIPSS observations at selected *N* and pulse energies at (a) 150 fs and (b) 20 ps. The 10 μm calibration bars are applicable to all the images, and the 5 μm calibration bar only applies to the specific image.

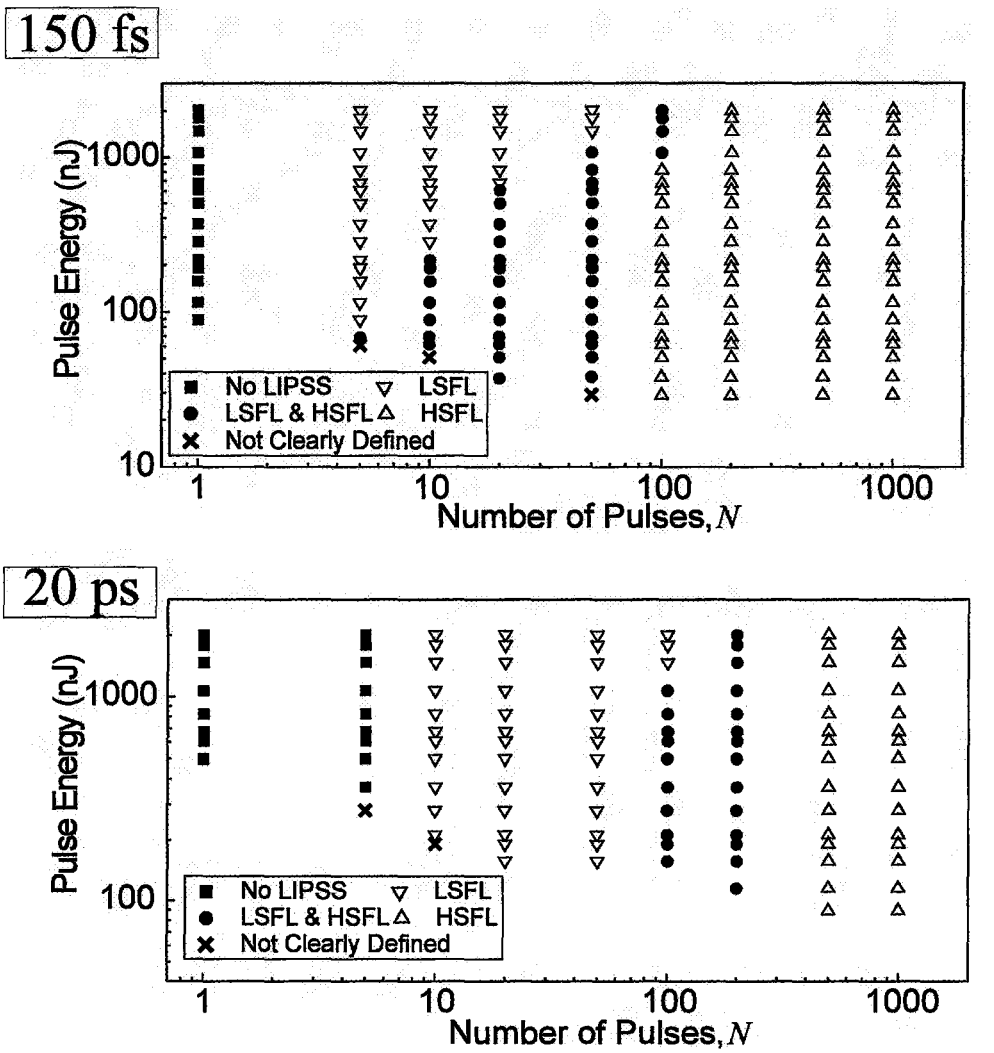

Figure 3-5: Summary of *N* and pulse energy conditions where different types of LIPSS are observed when 150 fs and 20 ps pulses are used. "Not Clearly Defined" signifies damage is too small to be able to clearly identify the type of LIPSS.

At a pulse duration of 80 ps, on the sites where HSFL were evident, HSFL were just scarcely observed at the periphery of LSFL-dominant sites (e.g., see Figure 3-6). As described in section 3.3.2, one of the two laser systems used delivered pulses with a somewhat elliptical profile. The ellipticity profile of the beam can arise from damaged intracavity optical elements in the CPA. Such a beam profile is evident in Figure 3-6.

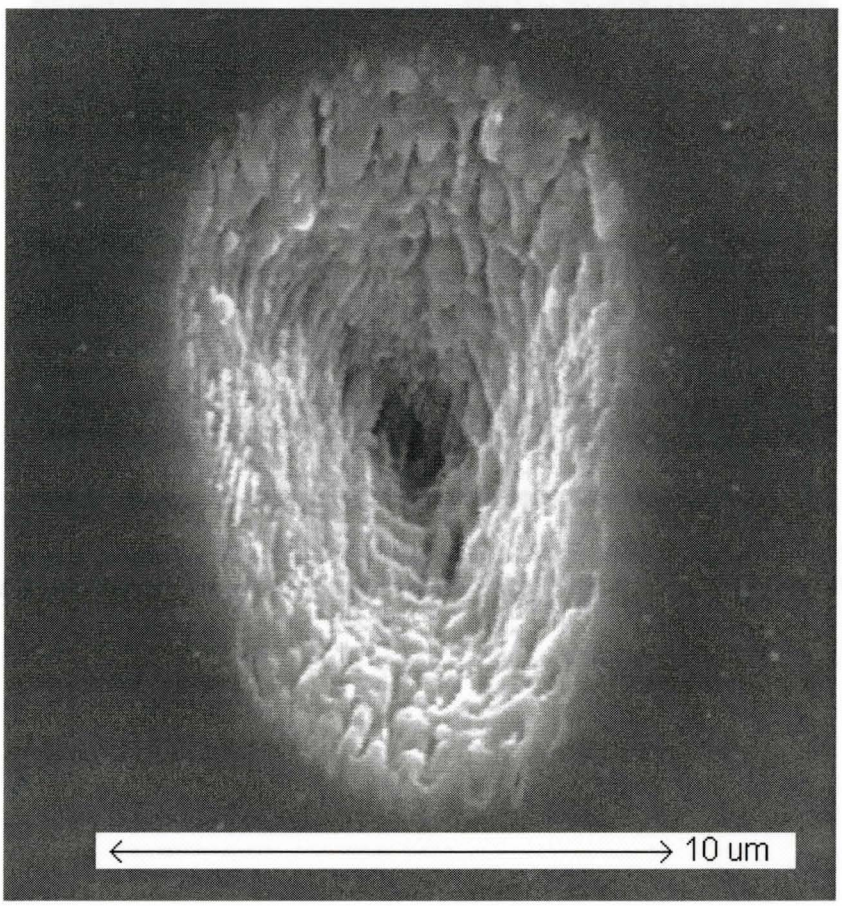

Figure 3-6: SEM image of a site irradiated with 1000 pulses with a pulse energy of 150 nJ and a pulse duration of 80 ps. At this pulse duration, if HSFL are present they are only scarcely observed while LSFL are observed in the central region.

Only LSFL were observed at sites irradiated with 130 ps and 220 ps pulses (e.g., see Figure 3-7), and no LIPSS are observed at sites irradiated with 7 ns pulses. Instead, signs of melting and resolidification are observed on sites irradiated with this pulse duration (Figure 3-8).

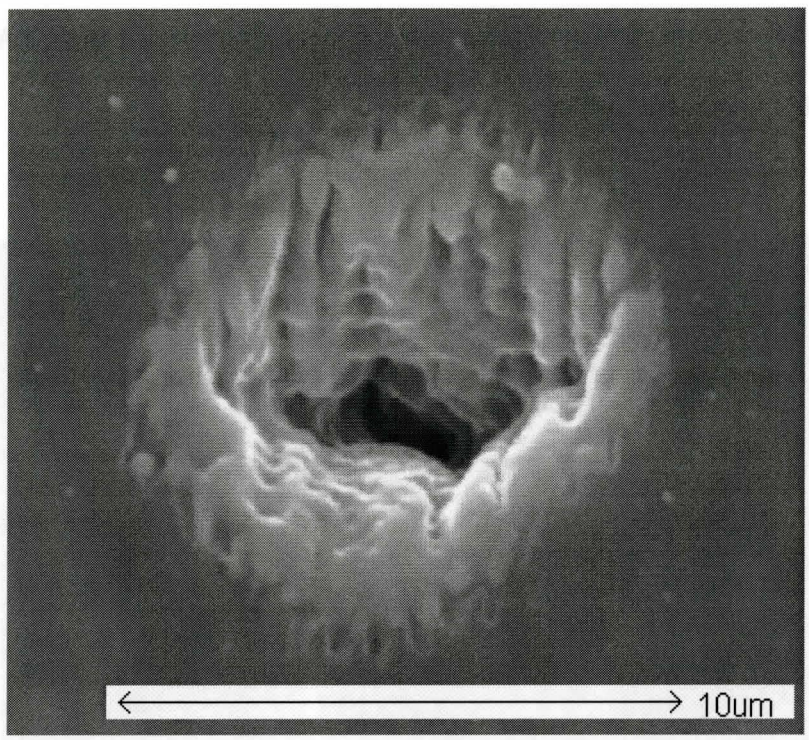

Figure 3-7: SEM image of a site irradiated with 1000 pulses with a pulse energy of 110 nJ at a pulse duration of 130 ps. No HSFL are observed in any of the sites irradiated at this pulse duration.

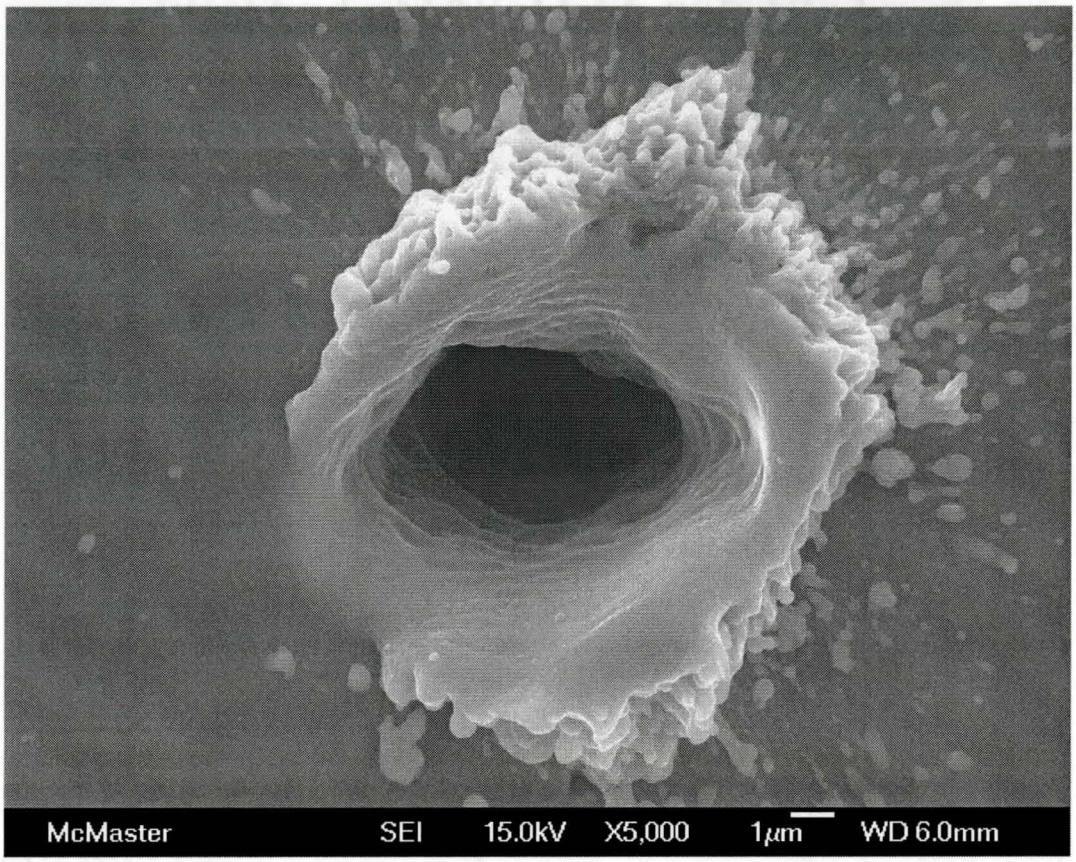

Figure 3-8: SEM image of a site irradiated with 500 pulses with a pulse energy of 1.7 μJ at a pulse duration of 7 ns. No LIPSS are observed on any sites irradiated with this pulse duration. Instead, signs of melting, resolidification and cracking are evident.

Figure 3-9 shows a summary of LIPSS evolution for selected N and pulse durations for pulse energies close to threshold for each N and pulse duration condition. It can be observed that as the pulse duration increased, HSFL required a higher number of pulses to form. For example, when irradiated with 150 fs pulses, HSFL can be generated at $N = 50$. However when the pulse is stretched to 20 ps, only LSFL are observed at $N = 50$.

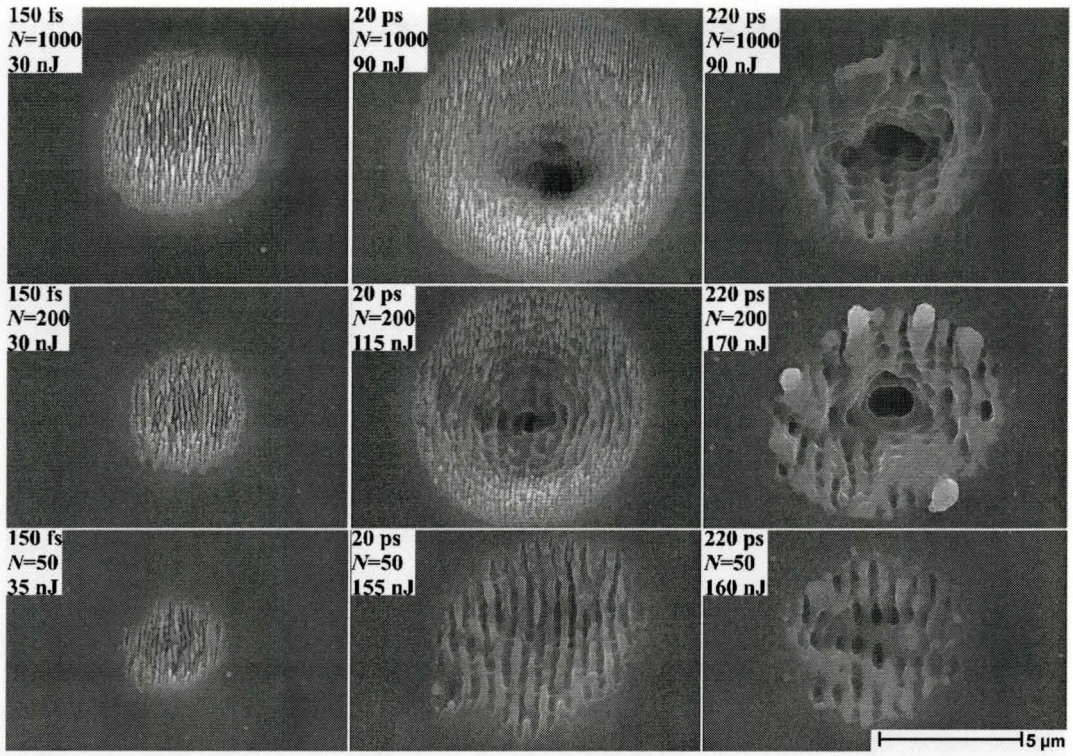

Figure 3-9: Summary of LIPSS distribution at selected *N* and pulse durations, at energies that are relatively close to threshold. As pulse duration is increased, higher number of pulses is required to generate HSFL. When the pulse duration is stretched beyond 80 ps, HSFL are no longer observed.

This experiment showed that HSFL can form over a large range of pulse durations. The threshold energies only increased slowly as pulse duration is increased (Figure 3-10). Behavior of the threshold energies as the pulse duration increases is qualitatively similar to reports in the literature for several other materials [65-68]. However, the intensity of the laser pulses corresponding to near-threshold energies decreases rapidly as the pulses are stretched.

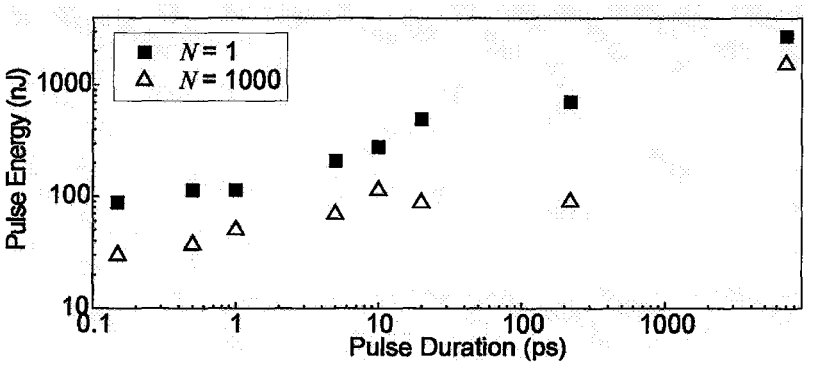

Figure 3-10: Lowest pulse energies employed in this experiment where surface modification is observed at selected pulse lengths for $N = 1$ and $N = 1000$.

The results of this experiment also suggeste the HSFL formation can be quite insensitive to the peak pulse intensity of the incident pulses. Extensions of this experiment in conjunction with work reported in [54] can further test the role of nonlinear interactions as an origin of HSFL formation. In [54], simultaneous irradiation of 800 nm and 400 nm was carried out and the behavior of HSFL formation was studied when the power ratio and polarization between the 800 nm and 400 nm pulses were changed. Further discussions are presented in Section 3.8 where the LIPSS results presented in this thesis are considered collectively, for convenience, when comparing to literature reports.

A side observation made was that at longer pulse durations (> 10 ps, for instance) the threshold behavior of the ablation becomes less deterministic. This observation is consistent with some reports in the literature [69, 70].

3.4 LIPSS on Gallium Phosphide: Cross-sectional Study

3.4.1 Introduction

Careful study of HSFL features is an important task in determining their formation mechanism. Common imaging techniques used in the literature include scanning electron microscopy (SEM) and atomic force microscopy (AFM). While both techniques complement each other to yield valuable information about HSFL, they each have their own limitations. Both techniques can readily provide information for irradiated sites, however, depth can not be accurately determined based on SEM images and for closely spaced fine features such as HSFL, depth information can be limited by the probe tip geometry in AFM. A cross-sectional study of HSFL, on the other hand, is a promising method to examine the features deeper into the surface (i.e. troughs of the ripples).

However, preparing a sample for cross-sectional study using polishing techniques on small features such as HSFL can cause unwanted mechanical damage, and precision becomes an issue when attempting to target a cleavage plane through a single laser irradiated site (typically a few to tens of micrometers in diameter). The cleaving method could be more suited for HSFL formed in a groove by laser irradiation along a length on the surface. In a groove, HSFL occupy a long linear region, making it more forgiving to the inaccuracy of cleaving. However, damage such as chipping of the LIPSS can result from this technique as well. Through the use of Focused Ion Beam (FIB) milling, thin cross

section specimens that are transparent to an electron beam can be prepared with less collateral damage than by mechanical means. These specimens can be examined using transmission electron microscopy (TEM).

This part of the thesis is based on two experimental studies of cross-sections of HSFL structures, where the cross-sections are prepared using FIB-preparation and the cleaving technique.

A journal manuscript is being prepared based on selected data and figures presented in this section.

3.4.2 Cross-sectional Study of LIPSS on Focused Ion Beam Prepared Specimens

In the first experiment, TEM studies were performed on FIB prepared specimens from sites where LIPSS were observed. A cross-sectional TEM study of a FIB specimen showing LIPSS formed on InP had previously been studied in our group [48]. However, the irradiation in the aforementioned work was performed with a long wavelength and lower number of shots, and the region where the FIB specimen was extracted was not ideal for HSFL observation since it was obtained from a transitional region between LSFL and HSFL. LIPSS formed in Si had also been reported in the literature using cross-sectional TEM technique on FIB specimen [69].

3.4.2.1 Experimental Setup

This experiment employed a typical experimental setup as described in section 2.2.2. Irradiation was performed in rough vacuum (~ 0.05 mbar) on a GaP sample having the same properties as the sample used in Section 3.3. The laser pulses were focused perpendicularly to the sample surface with a lens having a 75 mm focal length, yielding a spot size of ~ 13 μm $1/e^2$ radius as extracted using the D^2 technique [62]. Compared to the 5× microscope objective used in the experiment described in the previous section, the larger spot size provided by the 75 mm focal length lens allows a larger area over which LIPSS form upon irradiation. Having a larger area of observation allows a more forgiving margin of inaccuracy in the cross-section preparation process. Irradiation was performed with 150 fs pulses and a repetition rate lowered by the chopper to 50 Hz. The pulse duration was measured using a second-order noncollinear autocorrelator. Pulse energies used in this experiment ranged from 460 nJ to 135 nJ, while N is varied from 100 to 1000.

3.4.2.2 Results and Discussions

Due to the expenses associated with the FIB specimen preparation, only a limited selection of irradiated sites was chosen for cross-section specimen preparation. In all cases LIPSS run perpendicular to the direction of the electric field polarization of the laser pulses. The first cross-section specimen was prepared on a site irradiated with 100 pulses at a pulse energy of ~ 415 nJ. Under

this irradiation condition, both LSFL and HSFL were generated, with HSFL appearing at the periphery of the site and LSFL found in the center region. Figure 3-11 presents SEM and TEM images of this site showing the locations of both types of LIPSS. LSFL and HSFL spatial periods at this site were found to be ~ 580 nm and 185 nm, respectively Assuming a Gaussian spatial distribution of energy in the laser pulses, the area where HSFL formed corresponds to a region where the localized fluence was lower This suggests that for a given N, a lower local fluence favors HSFL generation. Such an observation is consistent with the trend shown in Figure 3-4 and Figure 3-5.

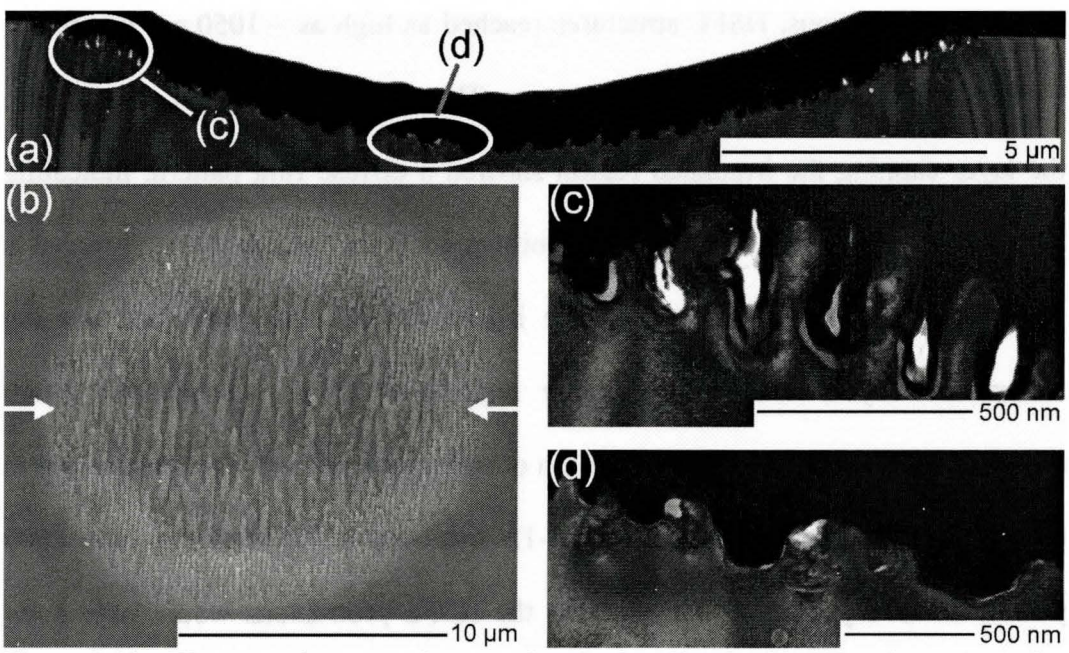

Figure 3-11: Electron microscopy images of a site irradiated with 100 pulses, at a pulse energy of ~ 415 nJ. With this irradiation condition both HSFL and LSFL are observed. (a) Cross-sectional TEM image on a FIB-prepared specimen. (b) SEM image of the irradiated site, showing HSFL surrounding LSFL. The arrows in the image indicate the region where FIB specimen was obtained. (c) High magnification TEM image of HSFL found at the periphery of the site, as marked in (a). (d) High magnification TEM image of LSFL found at the central portion of the site, as marked in (a)

The other two FIB specimens were obtained from sites irradiated with 1000 pulses at pulse energies of ~190 nJ and ~155 nJ, respectively. It should be noted that 155 nJ was the lowest energy used where observable damage (using both OM and SEM) on the GaP surface was still present. Since observations of both specimens were very similar, only details of the site irradiated with 190 nJ pulses will be reported. Under these irradiation conditions, only HSFL were observed throughout.

Figure 3-12 presents TEM images of a cross-section specimen prepared from a site irradiated with 1000 pulses at a pulse energy of ~190 nJ and a plane view SEM image of a site irradiated with the same conditions. Under such irradiation conditions, HSFL structures reached as high as ~ 1050 nm measuring from the base of the protrusions to the top. The electron diffraction pattern from the layer capping the irradiated region showed a diffuse ring pattern, indicating amorphous material. Under high magnification TEM imaging, we observed a single crystal structure throughout the irradiated site underneath the capping amorphized layer, including the inner regions of HSFL protrusions. More specifically, the structure and orientation of the crystal in the HSFL protrusions is the same as that in the bulk. Figure 3-12 presented a site irradiated with 1000 pulses, in the crystal-regrowth scenario the HSFL protrusions would have gone through numerous melt-regrow cycles. Based on the amount of material in the HSFL protrusions, it is unlikely for the material to have melted, then subsequently to have regrown perfectly matched to the bulk throughout the length of

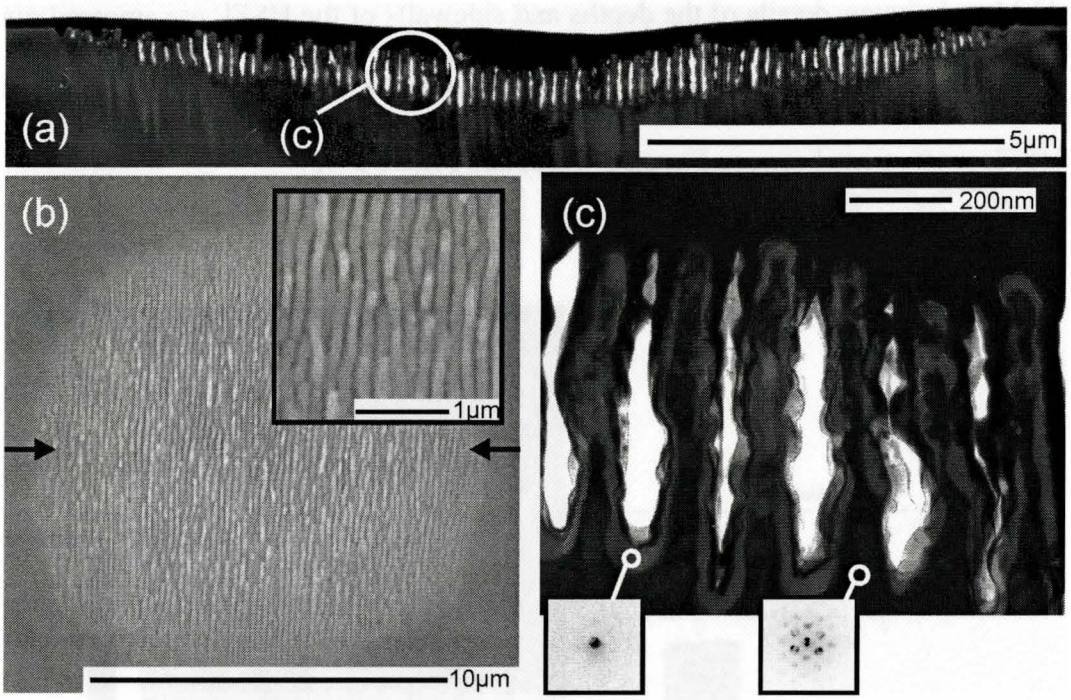

Figure 3-12: Electron microscopy images of sites irradiated with 1000 pulses, at a pulse energy of ~ 190 nJ. With this irradiation condition only HSFL are observed. (a) Cross-sectional TEM image on a FIB-prepared specimen. (b) SEM image of an irradiated site, showing generated at the site. Note that this is not the same site presented in (a) but one that is irradiated with the same conditions. The arrows in the image indicate the general region where FIB specimen was obtained. (c) High magnification TEM image of HSFL, showing the high aspect ratios of the HSFL structures. Inset: Convergent beam electron diffraction shows diffuse ring patterns indicating an amorphous layer capping the irradiated region, whereas single crystal structure is found in the bulk and the inner parts of the LIPSS structures.

HSFL protrusions. The observations of the crystal structures suggest the inner regions of HSFL protrusions remained unmodified throughout the irradiation process.

AFM imaging was performed on another site irradiated with the same N and pulse energy condition as the site presented in Figure 3-12. Figure 3-13 presents data obtained from the AFM work. While this microscopy technique provided measurements for the spatial periods that are consistent with SEM and

TEM techniques, details of the depths and sidewalls of the HSFL are smeared out by the geometry of the probe tip. This is evident in by comparing the sidewalls of HSFL protrusions between Figure 3-12(c) and Figure 3-13.

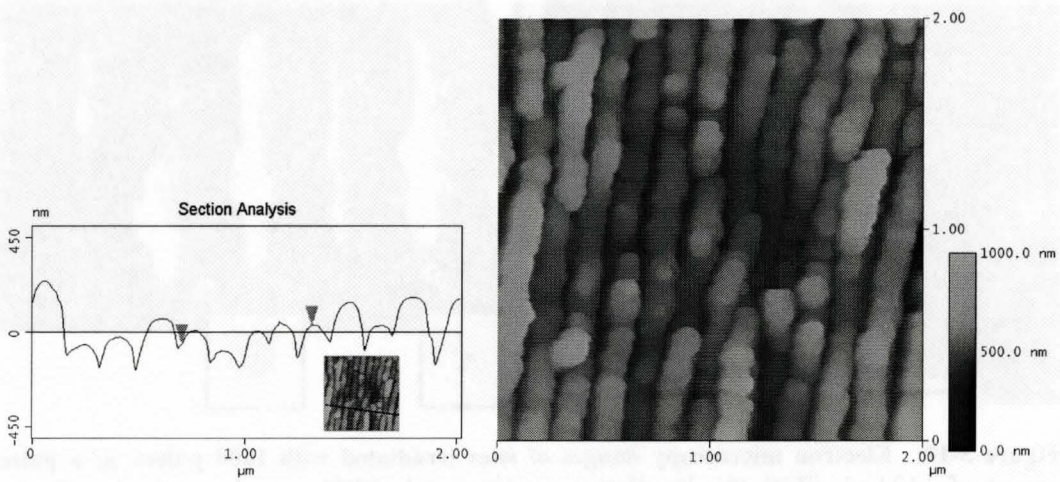

Figure 3-13: AFM section analysis and image of a site irradiated with 1000 pulses at a pulse energy of 190 nJ. While the correct spatial period of the HSFL is extracted with this technique, it is evident that the information in the deeper regions of the ripples and the sidewalls are lost due to the geometry of the probe tip.

Cross-sectional TEM images of HSFL showed that very high aspect ratios can be obtained when irradiation is performed with N = 1000 pulses (Figure 3-12). Extending this structure into three-dimensions, one could visualize these ripples as sheet-like planar structures. A major question arising from the observation was whether the HSFL periodicity was seeded initially near the surface and the periodicity was retained while HSFL protrusions deepened as material is removed with successive pulses, or whether the material was affected down to the depth of the HSFL protrusions at the early stages of irradiation.

Crystallographic studies on cross-sectional specimens from deeper regions of sites irradiated with a lower number of shots may answer this question.

Planar nanostructures have been reported in the literature when the laser pulses were focused into and translated across bulk fused silica [72-75]. In [74], a model was proposed for the formation mechanisms where the nanoplanes are said to originate from inhomogeneous local field enhancement. In this model, the formation of the nanostructures arises from nanoplasmas growing into nanoplanes when a linearly polarized laser source is used. This model also attributes the $\lambda_o/2n$ spacing to the supported mode in a linear waveguide (where n is the refractive index). Although the periodicity of the HSFL observed in this experiment was larger than $\lambda_o/2n$, the high aspect ratios of the HSFL protrusions do resemble planer nanostructures.

A comparison between the HSFL spatial wavelengths and the fundamental and the second harmonic wavelengths can be made. As in the experiment reported in Section 3.3, the spatial periods of HSFL obtained was smaller than the fundamental wavelength in the bulk of GaP, but larger than the second harmonic wavelength. Assuming that the second harmonic plays a key role in the generation of these structures, one possible argument for a second harmonic wavelength being larger than expected was raised in Section 3.3.3 where the refractive index is reduced due to the free electrons induced upon irradiation [54]. However, the high aspect ratio of the HSFL could also contribute to a reduction in the refractive index. From the cross-sectional images, it was shown that a

considerable amount of material can be removed in between the protrusions of the HSFL, implying that the average refractive index of the regions where HSFL formed was reduced. The reduction in the effective refractive index would occur once HSFL begin to form, and the refractive index decreased further as HSFL deepen with successive pulses.

Overall, this experiment revealed that HSFL can have a very high aspect ratio, and that single crystal structures were observed in the inner part of each HSFL protrusion. While a model for HSFL origin has not been developed based on this experiment, results of this experiment provide important insight to the formation mechanism of HSFL. Further discussions are presented in Section 3.8 where the LIPSS results presented in this thesis are considered collectively, for convenience, when comparing to literature reports.

3.4.3 Cross-Sectional Study of LIPSS Formed in Grooves Using Cleaving Technique

This experiment explored a simpler and more economical way to obtain a cross-section using a cleaving technique. Grooves were formed on the GaP sample while it was being irradiated and translated. The sample was subsequently cleaved such that a cleavage plane perpendicularly intersects the direction of the grooves, exposing the cross-sections of the grooves in the cleaved surfaces. The types of LIPSS generated in these grooves were determined by the pulse energy

and the effective number of pulses N_{eff} for a given region. An estimate of N_{eff} is given by the equation [76]:

$$N_{eff} = \sqrt{\frac{\pi}{2}} \frac{\omega_o f}{v} \qquad (3\text{-}6)$$

In the above equation, ω_o is the spot size of the laser pulses, f is the frequency of the incident pulses (or repetition rate), and v is the translation speed of the laser beam across the sample surface.

3.4.3.1 Experimental Setup

Irradiation of the sample was carried out in rough vacuum (~0.05 mbar) with 170 fs pulses (shortest pulse obtainable on the day this specific experiment was carried out) with a repetition rate of 1 kHz. Irradiation was performed on a GaP sample with the same properties as that used in the experiment reported in Section 3.4.2.1.

Since much of our previous work on the study of HSFL on GaP was carried out on sites irradiated with $N = 1000$ where they are readily formed (see previous sections), a sample translation speed which yields $N \sim 1000$ was desired to allow comparison of HSFL formed in both cases. Given that the Ti:Sapphire CPA system produces laser pulses at 1 kHz and the 75 mm-focal length lens yields a spot size of ~13 μm radius, a translation speed of 13 μm/s was used (Equation (3-6) yields $N_{eff} \sim 1100$). A different energy was used for each groove;

energies used in this experiment ranged from 440 nJ to 170 nJ. Deep notches were also cut at the edge of the sample to guide the subsequent cleave perpendicular to the grooves for the cross-section preparation. Figure 3-14 shows the cross-section of the entire sample to better illustrate the experimental procedure.

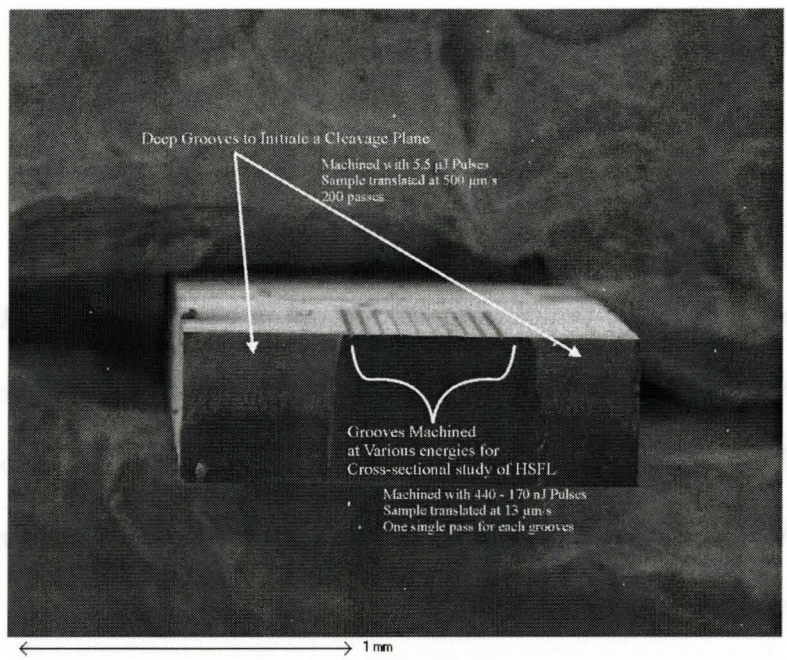

Figure 3-14: SEM image providing an overall view of the entire cross-section experiment. Different parts of the experiment are labeled in the image.

3.4.3.2 Results and Discussions

The first inspection of the grooves with SEM showed that there were indeed HSFL generated in the grooves. Spatial periods measured ranged from ~180 nm to ~155 nm, in the same vicinity of values measured for stationary

target irradiation as reported in Sections 3.3 and 3.4.2. Table 2 summarizes averaged spatial period measurements obtained from grooves machined with different pulse energies. There exists a statistical distribution of HSFL spatial periods measurements for each groove. Part of the statistics in the measurements can be due to bifurcation in the features. It is unclear whether the minimum HSFL spatial period found in grooves machined with 250 nJ pulses is due to HSFL formation mechanisms or whether the statistics in the measurements can explain this observation. For deeper grooves, measurements were made on HSFL found at the edges of the grooves where flatter features exist, since HSFL found on the sidewalls are at an angle relative to the incident direction of the laser pulses. Spatial periods for HSFL found at deeper regions were measured from cross-sectional SEM images. HSFL spatial periods in deeper regions of the grooves were slightly larger but comparable to the spatial periods of HSFL on the surface. It is unclear whether if the HSFL periods are larger at the bottom of the grooves due to the increased angle of incidence for the laser pulses, since some irregularity were observed in HSFL features. It was difficult to be certain the same part of the features measured in plane view SEM images were being measured in the cross-sectional images. More details on this irregularity are presented and discussed in this section.

Table 2: Spatial periods of HSFL formed in grooves micromachined with different laser pulse energies.

Pulse Energy	440 nJ	320 nJ	250 nJ	190 nJ	170 nJ
$\Lambda_{HSFL,\ surface}$	183 nm	161 nm	153 nm	158 nm	164 nm
$\Lambda_{HSFL,\ bottom}$		195 nm	162 nm		

HSFL were observed at the edges of the groove irradiated with a pulse energy of 440 nJ. Plane view SEM imaging showed rough structures in the deeper regions of the groove, possible resulted from redeposition of debris, preventing clear identification of LIPSS structures (Figure 3-15(a)). However, cross-sectional SEM image of the groove showed HSFL underneath the layer of rough features (Figure 3-15(b)).

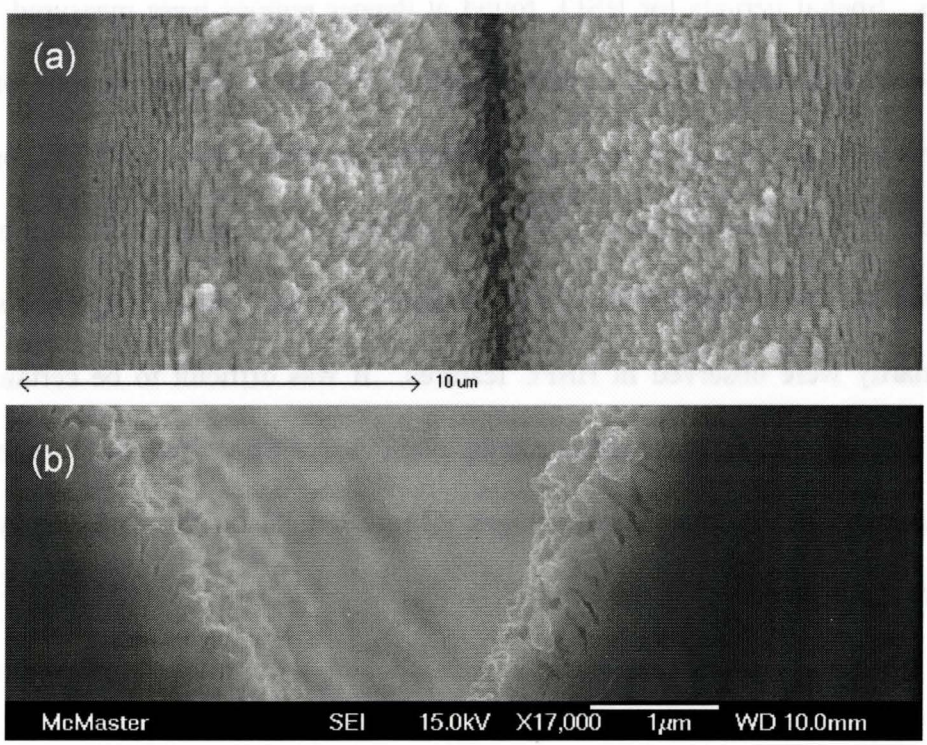

Figure 3-15: SEM image of a (single-pass) groove laser machined with 440 nJ pulses at a translation speed of 13 μm/s. HSFL are found at either side of the groove, corresponding to regions where the local fluence is lower. It is not obvious if HSFL exist on the sideawlls or the deepest portion of the grooves.

Figure 3-16 presents SEM images of grooves irradiated with 320 nJ pulses. As presented in this figure, HSFL were found from the edges of the groove to the very bottom, where significant depth was obtained via laser ablation. Also evident in this image was damage to HSFL near the cleavage plane that was likely to be introduced during the cleaving process (Figure 3-16(b)). One striking observation from the higher magnification cross-section SEM image (Figure 3-16(c)) was that in some cases the ripples appear to have the tendency to form at an angle somewhere between being perpendicular to the sidewalls and the incident direction of the irradiation pulses. This observation can perhaps shed light on the formation of HSFL.

As the irradiation pulse energy was decreased, the grooves became shallower. At a pulse energy of 190 nJ, relatively flat features were obtained. HSFL formed in the irradiation region have the top of the ripple structures almost at the level of the sample surface. Figure 3-17 presents SEM images of the top and cross-sectional view of a groove irradiated with 190 nJ pulses. HSFL are found to have a high aspect ratio similar to those observed in the FIB specimen reported in Section 3.4.2.

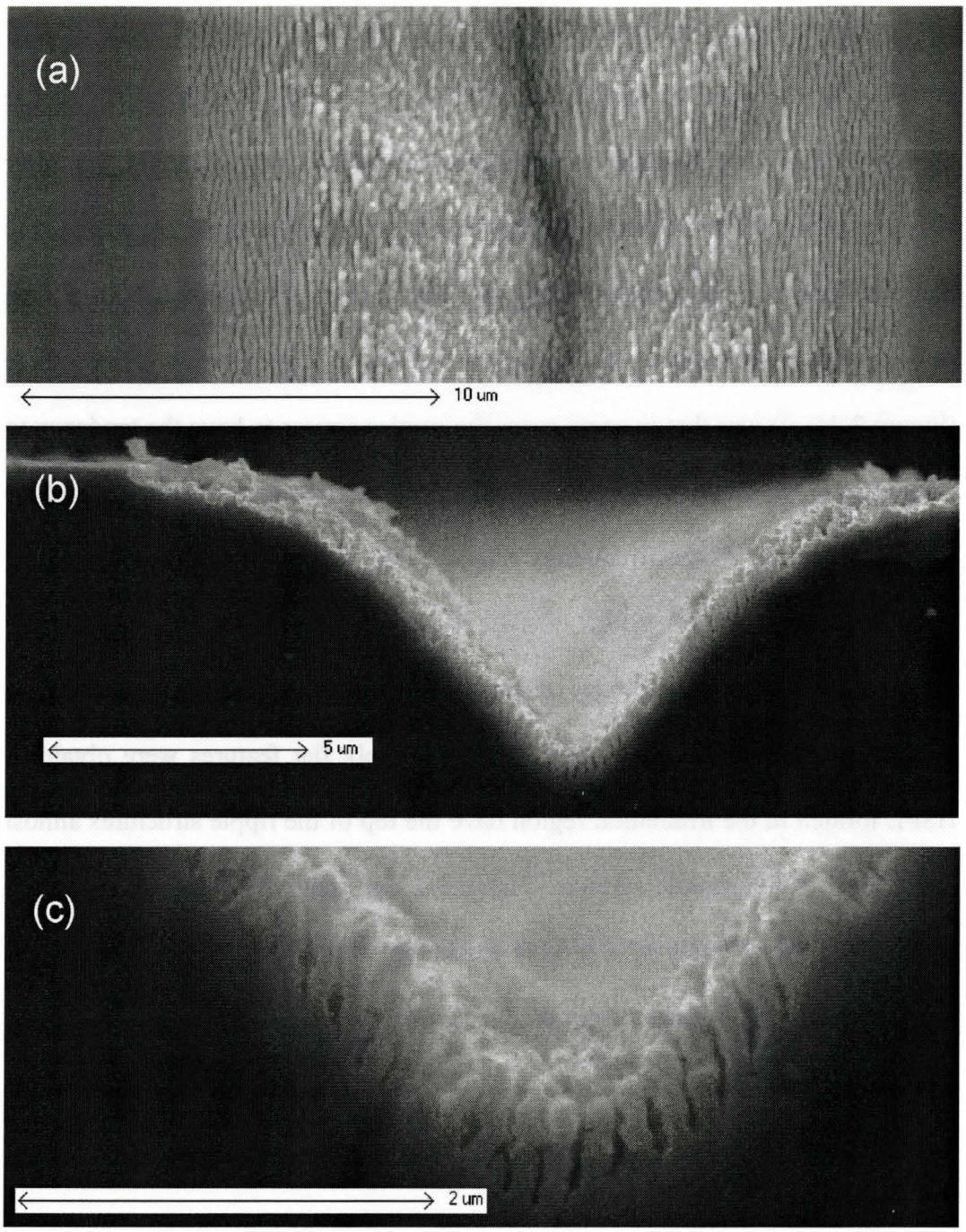

Figure 3-16: SEM images of a (single-pass) groove laser machined with 320 nJ pulses at a translation speed of 13 μm/s. HSFL are found throughout the groove. (a) Planar view of the groove. (b) Cross-section image obtained by looking at the ripples right at the cleaved surface. Damage likely introduced in the cleaving process is evident. (c) High magnification image of the bottom of the groove

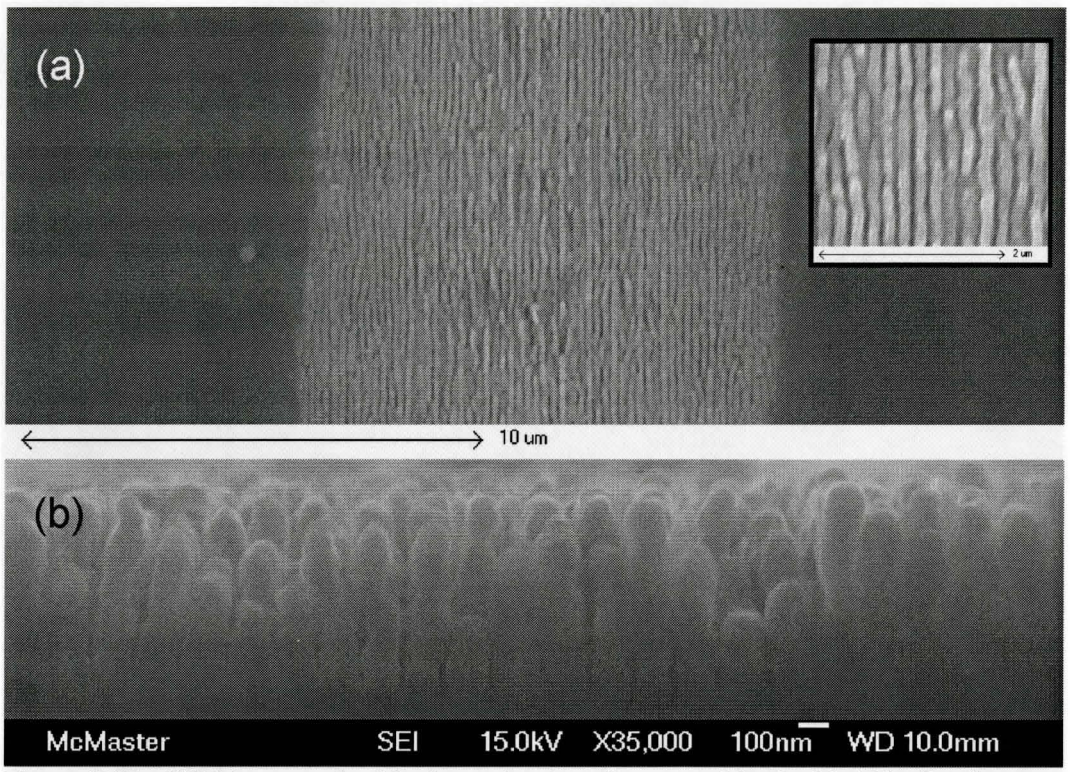

Figure 3-17: SEM images of a (single-pass) groove laser machined with 190 nJ pulses at a translation speed of 13 μm/s. HSFL are found throughout the groove. (a) Planar view of the grooves. The inset shows a high magnification of an arbitrary region in the groove. (b) High magnification cross-section image obtained by looking at the ripples right at the cleaved surface.

An accidental finding from this experiment was the formation of HSFL on the sidewalls of the deep notches that were merely intended to act to initiate and direct a cleavage plane across the grooves (refer to Figure 3-14). These deep grooves were irradiated with very different conditions compared to the grooves presented above.

Figure 3-18 presents SEM images of HSFL found on the sidewalls of one of these grooves. To quickly obtain a significant depth to guide the cleavage plane, a high pulse energy (~5.5 μJ), faster translation speed (500 μm/s) and multiple passes (100) were used. Equation (3-6) yields an effective pulse number

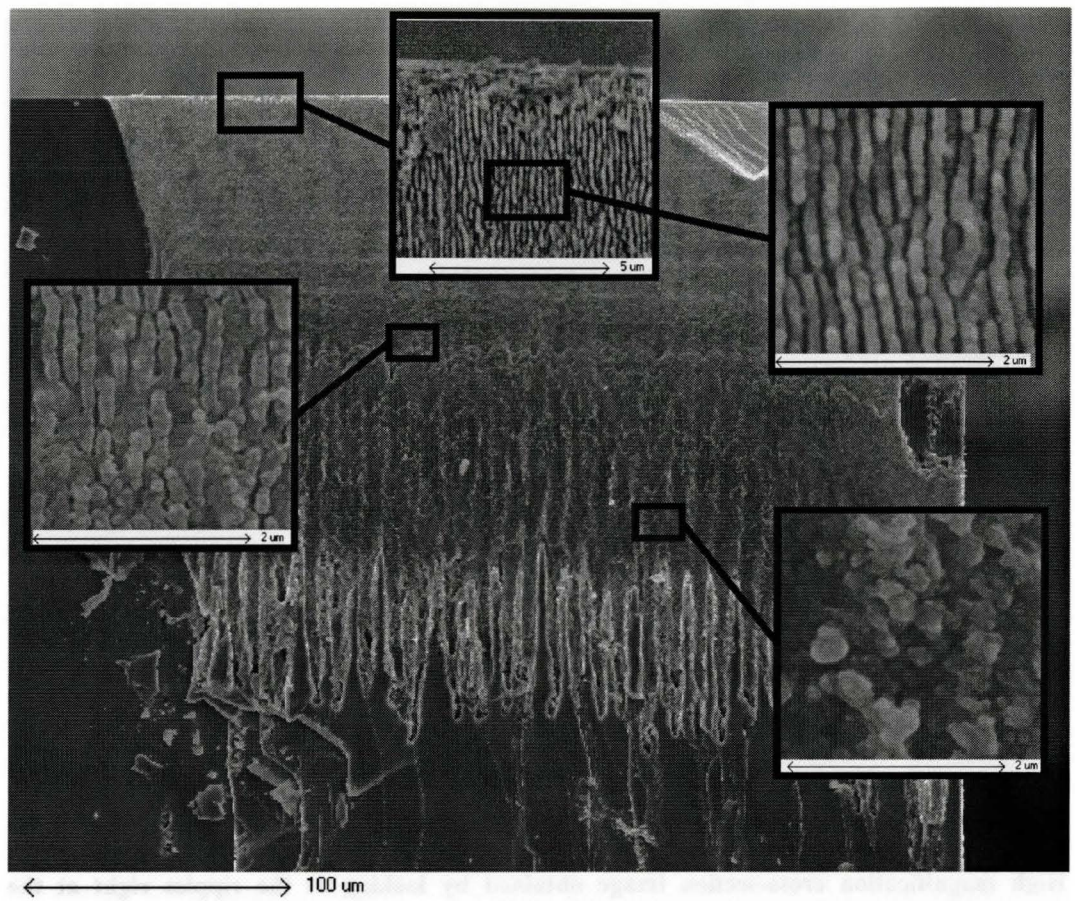

Figure 3-18: SEM images of the sidewall of a (100-pass) groove which was laser machined with 5.5 μJ pulses at a translation speed of 500 μm/s. HSFL are found on the sidewall of the grooves. Insets shows high magnification images on different regions of the grooves.

per irradiated region of approximately 30 for a single pass. From previous experiments, stationary irradiation with high fluences at $N = 30$ favor the generation of LSFL (refer to Section 3.3.3, more specifically Figure 3-5). Given that the repetition rate of the laser pulses is 1 kHz, the delay between each successive pulses (1 ms) is a few orders of magnitude longer than the expected time scale for ablation processes to complete and for the material to resolidify (refer to Section 2.1.2, on the order of tens of nanosecond). It is not surprising that micromachining with multiple passes would have the same effect as

irradiation with a single-pass that has a much higher N_{eff}, since the delay between each successive pulses, for both cases, effectively approaches infinity relative to the time scale of ablation processes. Future work can be performed to compare grooves ablated with multiple passes at higher speed and a single pass at a much slower speed where the two sets of grooves have the same total effective number of pulses per irradiation site. In the deeper regions, HSFL were not as prominent as they were near the upper sections of the sidewalls. Instead, semi-random and somewhat disruptive features were observed (refer to bottom-right inset of Figure 3-18). Coarse corrugation patterns are also observed on the sidewalls and bottom of the groove. The transition of ordered linear features (i.e. HSFL) to these disruptive, semi-random features (i.e. bottom right inset in Figure 3-18) towards the deeper regions of the groove, as well as the coarse corrugations are similar to observations made on grooves micromachined with ultrashort laser pulses on silicon [77].

Spatial periods between ~165 nm to ~195 nm were measured for HSFL found on these grooves. In the case of LSFL, Equation (3-1) predicts a reduction in the spatial periods as the angle of incidence decreases from surface normal (i.e. due to the slope of the sidewalls). Such an observation was made in [78] on copper, for irradiation with ~ 150 fs (at 800 nm and 400 nm) and ~10 ps (at 800 nm) pulses, where LSFL appeared to form after the holes were already developed (between 1000 and 10000 pulses) and the sidewalls of the holes were exposed to near-threshold laser fluence in at the wings of the spatial profile of the

beam. In [78], since the holes were developed before the formation of LSFL, the propagation direction of the pulses and the surface of the sidewalls of the holes approached 90° during the time frame where LSFL are developed. The LSFL spatial period observed in [78] was close to half of the irradiation wavelength, as predicted by Equation (3-1) for angle of incidence approaching 90°. However, HSFL observed in the grooves such as the one presented in Figure 3-18 have spatial periods that are comparable to those observed in the experiments reported in Sections 3.3 and 3.4.2, where the laser pulses were incident perpendicular to the sample surface. If HSFL spatial periods do have an angular dependency as demonstrated for LSFL, one might speculate the HSFL were formed at early stages of the irradiation near the surface, where the pulses were incident perpendicular to the surface, and the periodicity was maintained as the grooves deepened with successive pulses. Reports on the dependence of HSFL spatial periods to the angle of incidence during laser irradiation were not available during a recent literature survey. Such a study is warranted for future work.

3.5 LIPSS on Gallium Phosphide: Irradiation with "Scrambled" and Circular Polarization

3.5.1 Introduction

HSFL orientation is related to the polarization incident laser pulses. In most cases LIPSS tend to form perpendicularly to the electric field of the laser

pulses [14, 45-53]. However, some materials do show HSFL formed parallel to the direction of incident electric field [55, 56]. Irradiation with circularly polarized laser pulses has been reported in the literature, where bumps were observed in place of LIPSS [51, 56, 59, 80]. In this part of the thesis, results from two experiments will be reported and compared. In the first experiment, sites on GaP were irradiated with pulses with the polarization changing between each of the successive pulses, or "scrambled" polarization. In the second experiment the incident pulses had a circular polarization. The primary goal of this study is to compare the behavior of nanostructures formation when the polarization is rotated from one pulse to the next with the formation of nanostructures irradiated with circularly polarized light. The secondary goal of the experiment is to test whether it is possible to reduce or eliminate the formation of LIPSS through manipulation of laser polarization for applications where precision and smooth surfaces are required.

3.5.2 Experimental Setup

The experimental setup for both experiments mostly followed the typical experimental setup described in Section 2.2.2. Extra components were added to scramble the polarization or to create circularly polarized light. In both experiments ~ 150 fs pulses were used. The pulse duration was measured using a second-order noncollinear autocorrelator. The repetition rate of the laser pulses was lowered to 50 Hz by using a chopper. A lens with 75 mm focal length was

used to focus the light perpendicularly onto the sample. Irradiation was performed in rough vacuum (~ 0.05 mbar) on a GaP sample with the same properties as the sample used in Section 3.3.

3.5.2.1 Experimental Setup for Scrambling Polarization

To scramble the polarization from one pulse to the next, a half-wave plate was placed in a motorized spinning mount in the beam path such that the half-wave plate was rotating in a plane perpendicularly to the propagation direction of the laser pulses. A combination of its birefringent nature and predefined thickness allows the half-wave plate to rotate the polarization of linearly polarized laser pulses about the optical axis of the half-wave plate. By spinning the half-wave plate, the orientation of the optical axis of the half-wave plate was constantly being changed, and the electric field polarization between each successive pulse was rotated. Overall, this changed the polarization from one pulse to the next. To determine the rotation speed of the spinning mount, a strip of white tape was placed on to a black spinning portion of the mount. A HeNe laser was aimed at this spinning portion while the mount was spinning, and a photodetector was used to detect the increase in the amount scattered light each time the HeNe laser beam was incident on the tape. The output of the photodetector was connected to an oscilloscope where the time delay between each rotation (i.e. the rising edge of the signal from the photodetector, corresponding to the "leading edge" of the white strip of tape) could be measured.

The mount was determined to be rotating at 15.2°/ms. Since the rotation of the polarization of the light is about the optical axis of the half-wave plate, the polarization of the beam would be rotated by 30.4°/ms. The repetition rate of the laser was reduced to 50 Hz by a mechanical chopper (refer to Figure 2-16). We thus expect a rotation of 608° (or, effectively 112° in the opposite direction) in the polarization from each pulse to the next.

3.5.2.2 Experimental Setup to Create Circularly Polarized Light

To create circularly polarized light, a quarter-wave plate was placed in the beam path near the micromachining chamber (refer to Section 2.2.2). When aligned properly, a quarter-wave plate creates a phase shift between the two orthogonally polarized components of the incident light such that the output is circularly polarized. Since misalignment of the quarter-wave plate will produce elliptically polarized light instead of circularly polarized light, the alignment of the quarter-wave plate needed to be confirmed prior to irradiating of the sample. To confirm the alignment of the quarter-wave plate, a calcite polarizer cube was placed in a mount that can be rotated manually. If the light is truly circularly polarized, the output power through the polarizer should be constant regardless of the orientation of the polarizer. The power of the light through the polarizer was monitored with a power meter, and the orientation of the quarter-wave plate was adjusted until the above condition was met.

3.5.3 Results and Discussions

Both experiments yielded similar surface structures and morphologies. Instead of ripple-like structures obtained with linearly polarized light, as described in previous sections, SEM images showed that bump-like structures are generated. Two types of bumps were observed for both polarization schemes, one having an average diameter of ~ 410-520 nm (Figure 3-19(a) and (b)), while the second type are much smaller, having an average diameter of ~ 80-120 (Figure 3-19(c) and (d)). The larger bumps were observed at pulse energies and N conditions that roughly correspond to where LSFL were observed in the case of irradiation with linearly polarized light (refer to Section 3.3.3). Similarly the fine bumps were observed at pulse energies and N conditions that roughly correspond to where HSFL were observed in the case of irradiation with linearly polarized light (refer to Section 3.3.3). It might be reasonable to visualize the bumps to have formed by different sets of LIPSS with different orientations (due to the change in incident electric field polarization), forming an overlapping "grid" of LIPSS. However, while the fine bumps are similar in size for irradiation with scrambled and circular polarization schemes, qualitatively different surface morphologies were observed. On sites where the fine bumps are generated, irradiation with circularly polarized light generated larger bumps mixed in with the fine bumps (Figure 3-19(d)). This was not observed when samples were irradiated with scrambled linearly polarized light (Figure 3-19(c)).

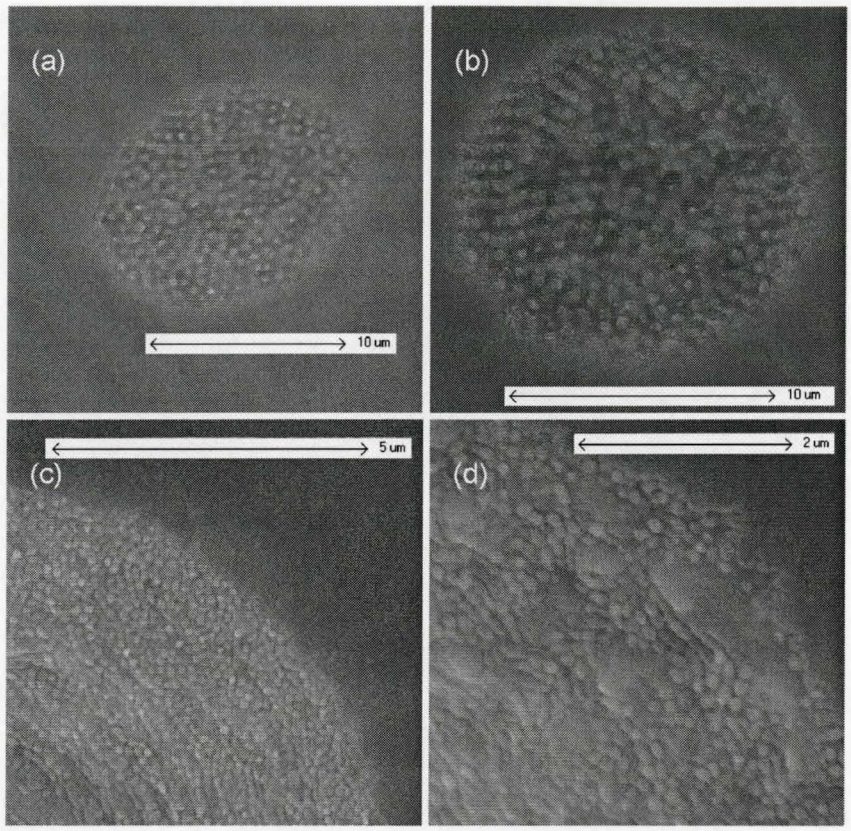

Figure 3-19: (a) and (b): Sites irradiated with $N = 50$ pulses, at a pulse energy of ~415 nJ, showing large bumps in the central portion and fine bumps just at the periphery of the sites. (a) Scrambled (but linearly polarized) light. (b) Circularly polarized light. (c) and (d): Sections of site irradiated with $N = 1000$ pulses, at a pulse energy of ~305 nJ, showing fine bumps found at the site. (c) Scrambled (but linearly polarized) light. (d) Circularly polarized light.

When circularly polarized light was used, deep craters showed a spiral pattern on the sidewalls of the craters. This pattern was not observed on craters ablated by light with scrambled polarization, and is much more pronounced in craters irradiated with a higher number of shots (Figure 3-20).

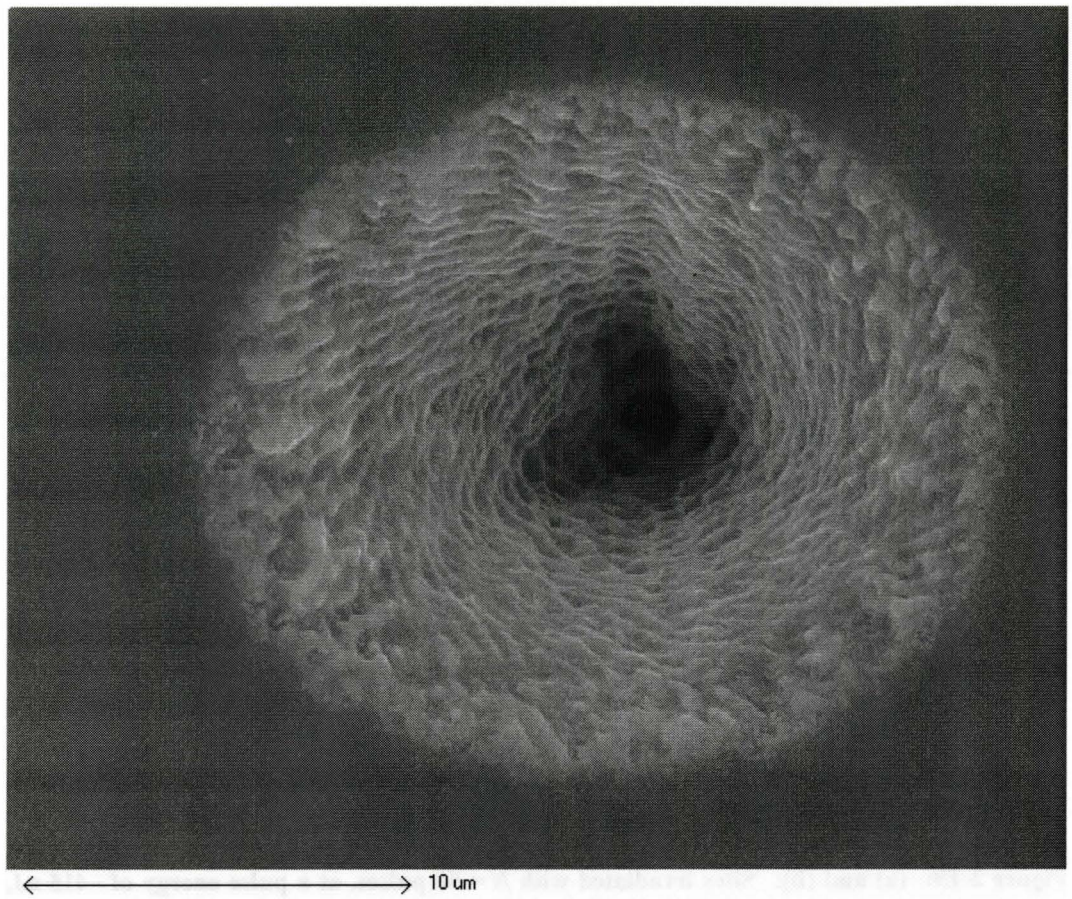

Figure 3-20: SEM image of a site irradiated with $N = 10\ 000$ at a pulse energy of ~310 nJ. When circularly polarized light is used, spiral pattern on the sidewall is observed for higher number of shots.

Fine bumps have been previously observed in the literature when materials are irradiated with circularly polarized ultrashort laser pulses on different materials [51, 56, 59, 80]. However, the observed features from this experiment appeared to be qualitatively different from the reported features in [51], [56], [59] and [80]. More specifically, [51], [56] and [80] report nanobumps arranged in long, mostly parallel chains. This type of distribution for the bumps was not observed in this experiment. Rather, the distribution of bumps observed in this work appeared to be somewhat random, similar to the observation reported in

[59]. However, much higher areal density of bumps was reported in [59] than was observed in this experiment. Also, the nanostructures reported in [51] appear to have somewhat angular and irregular shapes under 800 nm irradiation when compared to the features observed in this experiment as well as [56], [59], and [80], which show nanostructures that have a somewhat circular shape.

Another observation reported in [51] worth noting is the dependence of the mean diameter of the nanostructures on the irradiation wavelength. Under irradiation with 800 nm pulses, nanostructures with mean diameters of $\lambda/5$ and $\lambda/10$ (where λ is the free-space irradiation wavelength) were observed on titanium nitride and diamond-like carbon, respectively [51]. When the irradiation wavelength was frequency-tripled to 267 nm, the mean diameters of the nanostructures and the spacing between the nanostructures were reduced by a factor of 3, showing a linear scaling of the nanostructure dimensions with the irradiation wavelength [51]. Future work can be carried out to investigate the wavelength dependence of the nanobumps observed in this experiment.

An interesting future study would be to perform cross-sectional analysis on a site where the fine bumps are observed. If irradiation conditions can be established such that these bumps can have the same high aspect ratio as HSFL described in Section 3.4, they might have dimensions comparable to larger nanowires and may have potential niche applications. However, if their formation mechanism is identical to HSFL, it is possible that there would be an amorphized layer outside these structures. This could limit the potential applications, unless

follow-up processing is carried out (e.g. possibly thermal annealing to facilitate recrystalization).

Another interesting future experiment is to synchronize the spinning rate of the half-wave plate with the laser repetition rate such that each pulse will have its polarization rotated 90° from the previous one. This experiment will investigate the effect of polarization on the formation of LIPSS and determine to what extent the LIPSS gets "locked in" to a certain polarization. For example, once the LIPSS structures begin to form, would a 90° shift in polarization create LIPSS structures that are also rotated by 90°, or are the rotated set of LIPSS preferentially suppressed by the LIPSS that have formed already. Another way to obtain pulses with alternating polarization at 90° is to modify an autocorrelator such that a half-wave plate rotates the polarization of one of the pulses after splitting of the incoming pulse, and the two pulses can be combined using a polarizer. The separation of the pulses from such a setup can be controlled between 0 to ~330 ps with the components currently employed in the autocorrelator. Analysis of future work should include the use of 2D Fourier analysis of the microscopy images.

3.6 *LIPSS on Gallium Phosphide: Effect of Wavelength*

3.6.1 Introduction

This part of the thesis reports results from an experiment where GaP was irradiated with pulses having a 400 nm wavelength. The goal of this experiment

is to confirm two general observations reported in the literature as well as from our previous experiments. Based on literature reports and our previous work, LSFL are typically expected when samples are irradiated with pulses having a wavelength corresponding to an above-bandgap photon energy. Since the bandgap of GaP is 549 nm [59], 400 nm pulses have a photon energy that is above bandgap. The other effect that was automatically tested by this experiment is the orientation of the ripples in relation to the direction of incident electric field. The orientation of the ripples can be tested for irradiation with any wavelength, by rotating it using a half-wave plate for example. However, since the polarization orientation of the 400 nm pulses in this experiment was perpendicular to that of the 800 nm pulses through the frequency conversion process, the directions of the ripples when irradiated with pulses having a rotated polarization can be observed.

3.6.2 Experimental Setup

The experiment setup was based on the typical micromachining setup as described in Section 2.2.2. To generate 400 nm pulses, a 150 μm thick beta barium borate (BBO) crystal was placed in the beam path to act as a second harmonic generation medium to frequency-double the 800 nm light. The pulse duration of the 800 nm pulses was measured to be ~ 150 fs, using a second-order noncollinear autocorrelator. The expected pulse duration for 400 nm light, assuming the BBO crystal is thin enough to provide sufficient phase matching bandwidth, should be shorter than the fundamental pulse by a factor of $2^{1/2}$ [81].

This yields an expected pulse length of ~105 fs. Irradiation setup was identical to the experiment reported in 3.4.2.1.

The sample was placed in rough vacuum (~0.04 mbar) during the experiment. Pulse energies of 1 μJ to 40 nJ were used. At each pulse energy different sites are irradiated with different number of laser pulses, N (more specifically, N used at each pulse energy are 1, 5, 10, 20, 50, 100, 200, 500 and 1000, 2000, 5000 and 10000). Due to a limitation in the micromachining control system, irradiations with $N \geq 2000$ were performed at a repetition rate of 1 kHz, while the rest of the irradiations were performed with a repletion rate of 50 Hz.

3.6.3 Results and Discussions

The ripples produced in this experiment were perpendicular to the incident electric field of the 400 nm laser pulses. One irradiated site in particular (N = 50, with a pulse energy of ~1 μJ) showed features in the central portion of the irradiated region that do not resemble LIPSS (Figure 3-21).

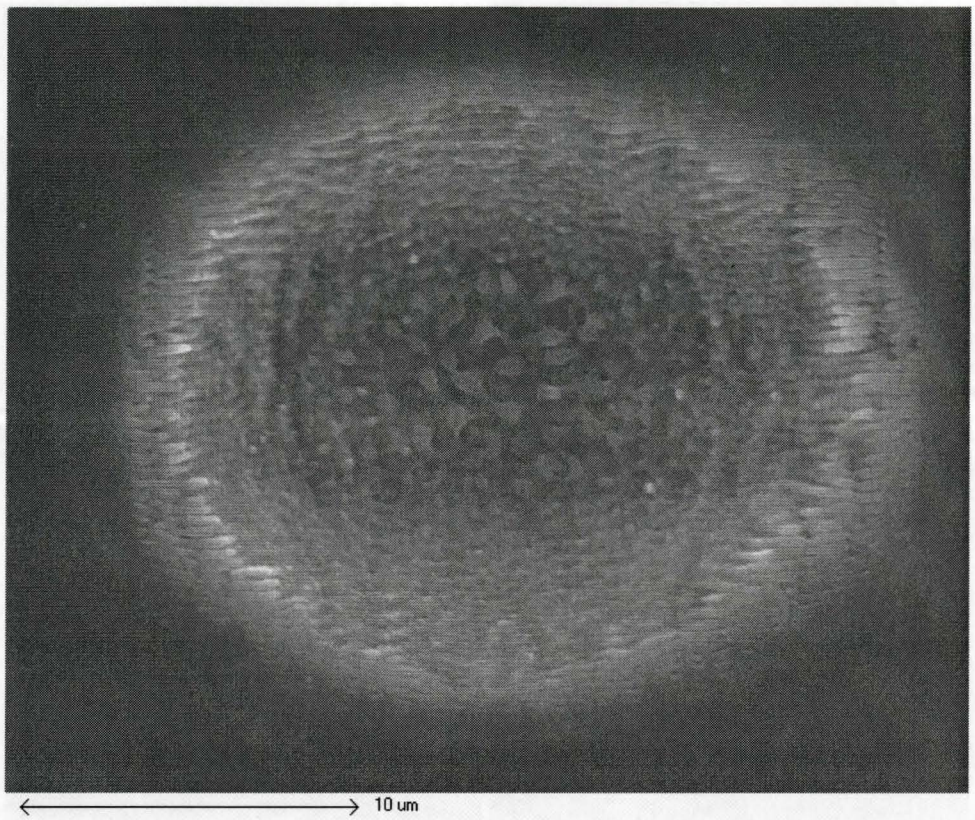

Figure 3-21: SEM image of a site irradiated with $N = 50$ with a pulse energy of ~1 μJ, at a wavelength of 400 nm. The central portion of the site shows features that do not resemble LIPSS. Since irradiation was performed with a short wavelength that is above the bandgap of GaP, no HSFL are found on any irradiated sites.

As N increases, LIPSS appearance became irregular (Figure 3-22). No HSFL are found on sites irradiated with this wavelength; only LSFL were observed. In general it was observed that irradiation with higher pulse energies generated LSFL with smaller spatial periods. LSFL were found to have spatial periods varying from 320 nm to 420 nm. LIPSS with spatial periods larger than the irradiation wavelength were unexpected and are generally not reported in the literature. Bifurcation of these LSFL, causing uneven spacing, could partly contribute to the large distribution in the spatial periods (e.g., see Figure 3-22).

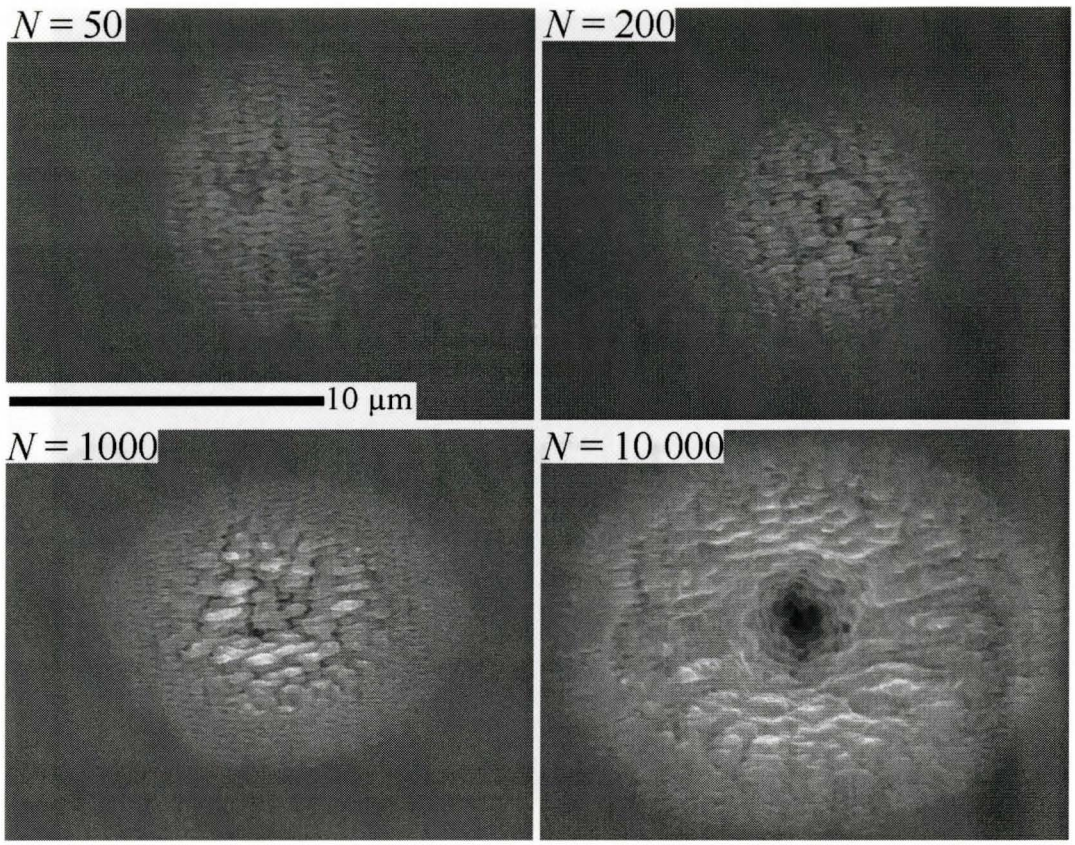

Figure 3-22: SEM images of sites irradiated with a pulse energy of ~ 90 nJ at a wavelength of 400 nm. The number of shots per irradiation site is labeled for each site.

The lack of HSFL due to irradiation with laser pulses having a wavelength corresponding to above-bandgap energy is consistent with observations reported in the literature [49, 50, 54].

3.7 LIPSS on Sapphire: Effect of Wavelength

3.7.1 Introduction

Sapphire samples were also irradiated to study the behavior of LIPSS formation on a wide bandgap dielectric material. Sapphire has a bandgap of 8.7 eV [82], which corresponds to a wavelength of 142 nm, above which the material is transparent. Since HSFL typically form when a material is irradiated with pulses having a wavelength corresponding to a below-bandgap energy [49, 50, 54], pulses with either 800 nm or 400 nm can be used to irradiate the sample to generate HSFL. In particular, it would be interesting to see whether HSFL with very fine spatial periods can be produced when the material is irradiated with a short wavelength (400 nm). It should be noted that this was a preliminary experiment and the irradiation conditions that best facilitate the generation of LSFL or HSFL might not have been employed in this experiment.

3.7.2 Experimental Setup

The experiment setup was mostly based on the typical micromachining setup as described in Section 2.2.2. Both 800 nm and 400 nm pulses were used to irradiate a c-plane sapphire sample. To generate 400 nm pulses, a 150 μm thick beta barium borate (BBO) crystal was placed in the beam path to act as a second harmonic generation medium to frequency-double the 800 nm pulses. The pulse duration of the 800 nm pulses was measured to be ~ 150 fs, using a second-order

noncollinear autocorrelator. Irradiation was carried out with a repetition rate lowered to 50 Hz using a chopper. A lens with a focal length of 75 mm was used to focus the laser perpendicular to the sample surface. This lens yields a spot size of ~ 13 μm based on D^2 technique [62]. The sample was placed in rough vacuum (~ 0.04 mbar) during the experiment. At a wavelength of 800 nm, pulse energies of 15 μJ to ~ 220 nJ were used to irradiate the sample. At a wavelength of 400 nm, pulse energies of 16 μJ to 200 nJ were used. At each pulse energy, sites were irradiated with different number of laser pulses N (more specifically, N used at each pulse energy are 1, 5, 10, 20, 50, 100, 200, 500 and 1000).

3.7.3 Results and Discussions

Comparing to gallium phosphide (refer to previous subsections in this Chapter), LIPSS do not appear to form readily on sapphire. When the sapphire sample was irradiated with 800 nm pulses, LSFL were only observed at a very narrow range of N and energy range, and were the most pronounced at $N = 10$ at a pulse energy of 15 μJ (Figure 3-23). These LSFL have a spatial period of ~720 nm. HSFL were observed on most of the irradiated sites for $N \geq 5$, in regions where no significant damage to the surface took place. For a given irradiated site, these HSFL tend to be observed in regions that were at a distance away from the center of the site (this can be observed in Figure 3-23), suggesting that the formation of these ripples is sensitive to the local fluence. These HSFL were found to have nominal spatial periods of ~255 nm. No obvious relationships

were observed between HSFL spatial periods and N or pulse energy Instead, a distribution between 210 nm and 300 nm exists throughout.

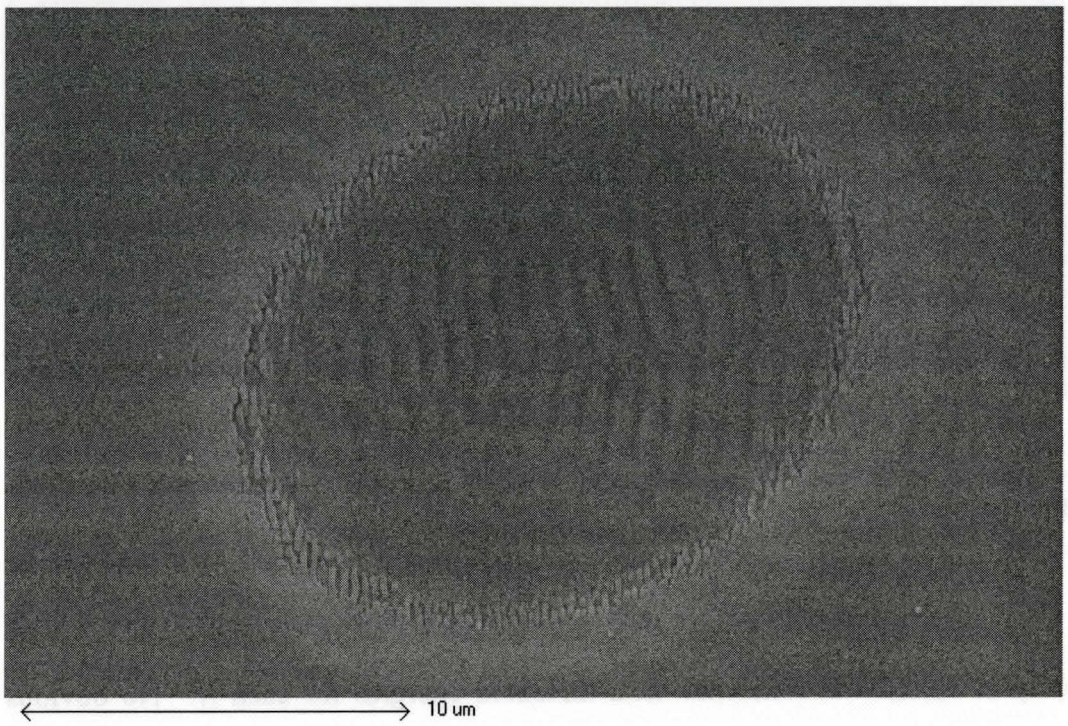

Figure 3-23: SEM image of a site irradiated with N = 10 at a pulse energy of 15 μJ and a wavelength of 800 nm. LSFL are generated at the central prtion of the irradiated site, while HSFL are found at the periphery.

In one particular case (N = 10, with 8 μJ of pulse energy) HSFL with spatial periods as small as ~ 155 nm were observed. These HSFL with finer spatial periods are surrounded by LIPSS with a nominal spatial period 230 nm, and the transition between the two types of LIPSS appeared to be gradual (Figure 3-24). The spatial period of ~ 155 nm measured for the HSFL is close to the third harmonic of the irradiation wavelength in sapphire. Refer to Section 3.8 for more details discussions and comparison of LIPSS results to literature reports.

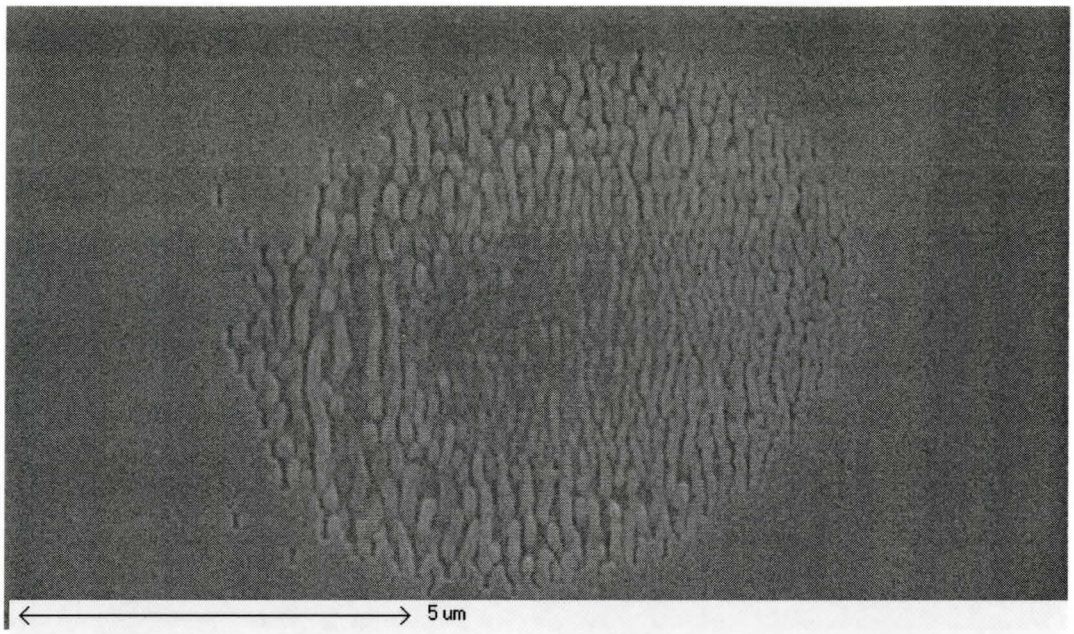

Figure 3-24: SEM image of a site irradiated with N = 10 at a pulse energy of 8 μJ and a wavelength of 800 nm. The spatial period of HSFL decreases at the central portion of the irradiated site.

Irradiation with pulses with a wavelength of 400 nm showed fine LIPSS only at $5 \leq N \leq 20$ at somewhat near-threshold energies for each N No obvious LSFL were observed. When N exceeded 20, deeper craters and/or irregular features were observed even at near threshold energies, preventing clear identifications of LIPSS structures to be made. Fine ripples found on sites irradiated with pulses with a 400 nm wavelength have a nominal spatial period of ~120 nm, and are found mostly in a circular band a distance away from the center of the irradiated region (for example, see Figure 3-25). This corresponds roughly to half of the fine LIPSS spatial period found in irradiation with a pulse wavelength of 800 nm. This observation is not surprising since LIPSS are

expected to scale with the irradiation wavelength [48, 49 and 50], assuming that the interference effects provide the dominant mechanisms.

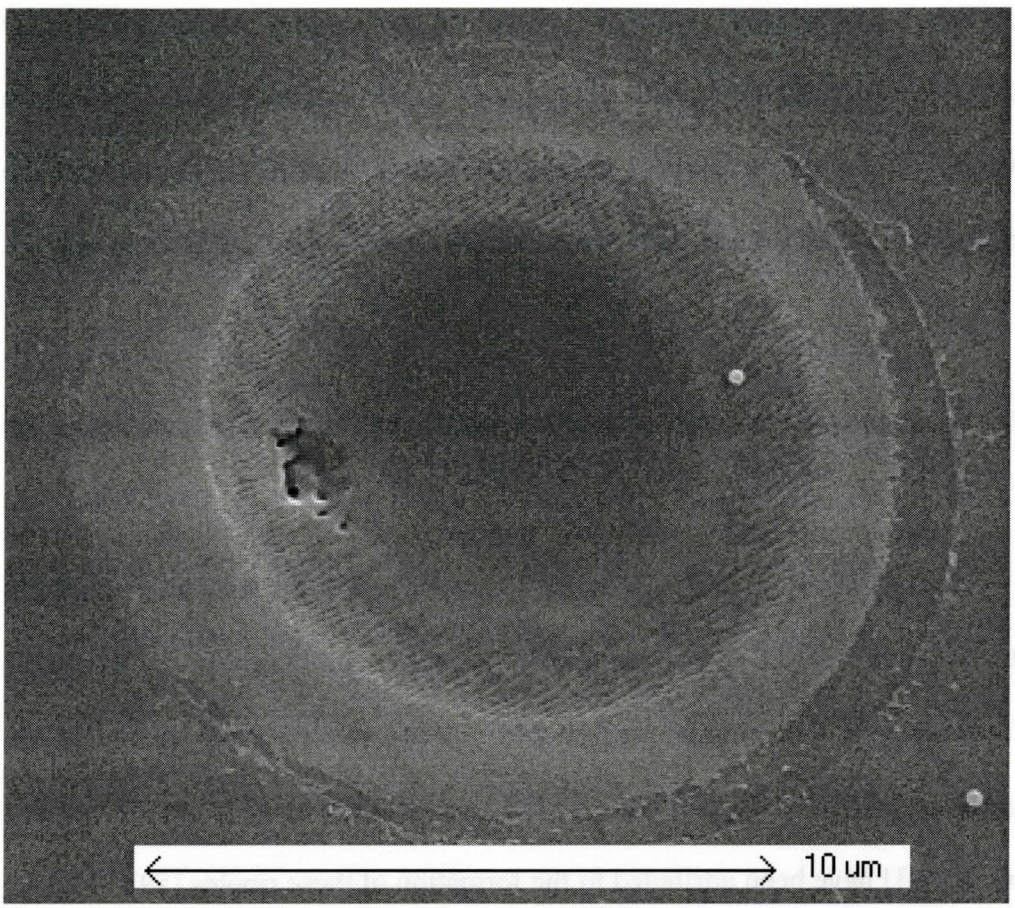

Figure 3-25: SEM image of a site irradiated with N=20 pulses with a pulse energy of 3.4 μJ at 400 nm.

This preliminary experiment confirmed that both 800 nm and 400 nm pulses can be used to generate fine LIPSS on sapphire. LIPSS observations in Figure 3-24 showed a gradual decrease in the spatial periods toward the center of the irradiated site, approaching the third harmonic wavelength of the fundamental (irradiation wavelength) in sapphire. It might be worthwhile to investigate the

striking features observed in Figure 3-23 and Figure 3-24. LSFL observation in Figure 3-23 showed LSFL in the central region having slightly different orientation, with a somewhat distinct boundary. An interesting extension of this experiment might be to use a material with a wide bandgap, where even frequency tripling or quadrupling of the Ti:Sapphire laser system output (pulses with 800 nm converted to 266 nm or 200 nm, respectively) corresponds to a below-bandgap energy, to determine whether even smaller spatial frequencies can be obtained.

3.8 Discussions and Comparison of LIPSS Reported in This Thesis to Literature Reports

As mentioned in Section 3.1, the exact formation mechanism responsible for the formation HSFL is unclear and is still under discussion in the literature. Self assembly of the material surface [46, 52-54], nonlinear interaction at the material surfaces [45, 47, 49, 50, 55, 56], and extensions [57, 58] of existing theory [41-43] have been attributed to the formation of these ripples [59].

A correlation between the spatial periods of HSFL is often made with the irradiation wavelength and its harmonics.

Table 3 presents a comparison of LIPSS spatial period measurements reported in this thesis as well as in the literature with the irradiation wavelengths and their second (and third, where applicable) harmonic wavelengths in different materials, provided relevant optical constants were available. LSFL reported in

the literature reports referenced in Table 3 typically have spatial periods somewhat less than the irradiation wavelength (between 63 – 95%). HSFL, on the other hand, typically have spatial periods near but somewhat larger than the second harmonic wavelengths in the material. In the case of sapphire where HSFL with even smaller spatial periods (as presented in Figure 3-24) are observed, the spatial period approaches (but is still somewhat larger than) the third harmonic wavelength in the material (refer to Table 3 for numerical details).

A comparison can be made between the HSFL spatial periods observed in GaP with the fundamental and second harmonic wavelengths. Second harmonic generation near the surface of the irradiated region had been suggested as a possible origin for HSFL formation [45, 47, 49, 50, 55, 56]. Referring to Table 3, the fundamental wavelength in the bulk GaP would be ~ 250 nm, much larger than the spatial periods for HSFL observed in this work. However, the HSFL spatial periods observed in the experiment is slightly larger than the second harmonic wavelength in the bulk. A reduction in the material refractive index can be induced upon laser irradiation due to the increase in the density of conduction band electrons [54], thus increasing the second harmonic wavelength in the material.

Table 3: Comparison of HSFL spatial periods to the fundamental and second harmonic wavelengths on different materials. Optical constants are provided if available. λ is the irradiation wavelength, $n(\lambda)$ is the refractive index of the fundamental wavelength for the material, $n(\lambda/2)$ is the refractive index of the second harmonic wavelength for the material, $\lambda/n(\lambda)$ is the fundamental wavelength in the material, $\lambda/2n(\lambda/2)$ is the second harmonic wavelength in the material, Λ_{LSFL} and Λ_{HSFL} are the spatial periods observed for LSFL and HSFL, respectively. Unless otherwise noted, optical constants are obtained from either [82] or [84]. For wavelength values that were not provided directly in [76] or [84], a rough estimate is made using linear approximation from the two nearest available values.

Material	Bandgap	λ (nm)	$\lambda/n(\lambda)$ (nm)	$\lambda/2n(\lambda/2)$ (nm)	Λ_{LSFL} (nm)	Λ_{HSFL} (nm)
GaP (reported in this thesis)	2.26 eV (549 nm)	800	250 (n=3.197)	95 (n=4.194)	520-680	150-175
GaP [49]					680	170
GaP (reported in this thesis)		400	95 (n=4.194)	95 (n=2.085)	320-420	
GaP [49]		1300	420 (n=3.079)	200 (n=3.300)	1050	300
		2100	690 (n=3.035)	340 (n=3.110)	1900	410
Sapphire (reported in this thesis)	8.7 eV (143 nm)	800	$\lambda/n(\lambda)$	$\lambda/n(\lambda/2)$	$\lambda/n(\lambda/3)$	Λ_{LSFL} 720 / Λ_{HSFL} 255	$\Lambda_{HSFL,II}$ 155
Sapphire [49]			455 (n_o=1.760)	225 (n_o=1.787)	145 (n_o=1.832)	730	260
Sapphire [83]							250
Sapphire (reported in this thesis)		400	225 (n_o=1.787)	110 (n_o=1.855)[1]	Λ_{LSFL}	Λ_{HSFL} 120	$\Lambda_{HSFL,II}$
InP [45]	1.35 eV (919 nm)	800	230 (n=3.462)	90 (n=4.415)	590-750	330-360
InP [49]		800			680	
InP [49]		1300	405 (n=3.203)	185 (n=3.520)	1150	310
InP [48]		2050	655 (n=3.131)	310 (n=3.304)	1730	470

Material	**Bandgap**	**λ (nm)**	**$\lambda/n(\lambda)$ (nm)**	**$\lambda/2n(\lambda/2)$ (nm)**	**Λ_{LSFL} (nm)**	**Λ_{HSFL} (nm)**
InP [49]	1.35 eV (919 nm)	2100	670 (n=3.130)	320 (n=3.289)	1750	430
GaAs [49]	1.43 eV (867 nm)	2100	630 (n=3.337)	300 (n=3.485)	1650	470
SiC[2] [46]		800			700	200
6H-SiC [56]	3.023 eV (410 nm)	800	295 (n_o=*2.730*) 300 (n_e=*2.649*)	145 (n_o=*2.795*) 140 (n_e=*2.860*)		150
		510	190 (n_o=*2.700*) 185 (n_e=*2.738*)	80 (n_o=*3.289*) 75 (n_e=*3.389*)		100
		400	145 (n_o=*2.795*) 140 (n_e=*2.860*)	50 (n_o=*3.947*) (n_e=N/A)		80
SiC-TiC-TiB[3] [46]		800			500	200
AlN[4] [46]	5.3, 5.8 eV (234 nm, 213 nm)	800	(n_o=N/A)[5]	180 (n_o=2.193) 180 (n_e=2.248)	610	200-300
TiN [51]	3.4 eV (365 nm)	800	**$\lambda/n(\lambda)$** (n=N/A)[6]	**$\lambda/n(\lambda/2)$** 200 (n=1.99)[6]	**$\lambda/n(\lambda/3)$** 110 (n=2.47)[6]	125
		267	110 (n=2.47)[6]	(n=N/A)[6]		40

Material	Bandgap	λ (nm)	$\lambda/n(\lambda)$ (nm)	$\lambda/2n(\lambda/2)$ (nm)	Λ_{LSFL} (nm)	Λ_{HSFL} (nm)
DLC[7] [51]	0.5-3 eV (2480-413 nm)[8]	800				100
		267				30
BaF_2 [52-54]		800	545 (n=1.472)[9]	270 (n=1.487)[9]	600-900	180-310
BaF_2 [53]		400	270 (n=1.487)[9]	130 (n=1.562)[9]		100-180
CaF_2 [53,54]	12 eV (103 nm)	800	560 (n=1.43052)	275 (n=1.44185)	600-900	180-310
CaF_2 [53]		400	275 (n=1.44185)	135 (n=1.49547)		100-180
ZnSe [55]	2.69 eV (461 nm)	800 & 400	320 (n=2.500) (using λ = 800 nm)	140 (n=2.890) (using λ = 800 nm)		160-180
Diamond Film [57]	5.5 eV (225 nm)	800	335 (n=2.397)	160 (n=2.463)	Λ_{coarse} 1600	Λ_{LSFL} 750 / Λ_{HSFL} 210
	Direct: 7.1 eV (175 nm)	400	160 (n=2.463)	70 (n=2.859)	Λ_{coarse}	Λ_{LSFL} 380 / Λ_{HSFL} 90

[1] Estimated value. This is in the transition region of wavelengths where n_o listed in [84]
[2] Crystal structure and orientation unspecified in this article
becomes n for longer shorter wavelengths.
[3] Unable to obtain optical constants for all of the compounds.
[4] Values for some optical constants have yet to converge in the literature [84].
[5] Optical constants are unavailable from [83] and refractive indices in this range of wavelength is in a region of an abnormal dip and is unavailable in [84].
[7] Refractive indices estimated from graphical data provided in [85].
[7] DLC, diamond-like carbon. The compositional nature of the film was not specified in the article, thus related optical constants are unavailable.
[8] The bandgap depends on the composition of the DLM film.
[9] Refractive indices estimated from graphical data provided in [85].

As mentioned in Section 3.4.2.2, with the high aspect ratios obtainable by HSFL features, a considerable volume of the top layer where HSFL are present can be occupied by voids. This type of structure will have a lower average refractive index. Other factors that can contribute to a change in the refractive index include a change in surface morphology or crystal structure after irradiation [48].

For most of the results summarized in Table 3, the HSFL spatial periods scaled with the irradiation wavelength and have spatial periods close to the second harmonic wavelength in the material. It might therefore be reasonable to consider second harmonic generation at the material surface as a contributing (if not sole) factor as the origin of HSFL. Similarly, the results for irradiation of sapphire presented in Section 3.7 (refer to Figure 3-24) showed HSFL with a spatial period close to the third harmonic wavelength in the material. This may suggest either the generation of third harmonic at the surface, or sum frequency generation between the fundamental and second harmonic, as a contributing factor for this type of HSFL. The observation of HSFL with spatial periods close to the third harmonic wavelength might be regarded as further support for higher harmonic generation at the material surface as an origin of HSFL generation. Observations of HSFL on TiN reported in [51] also reveal spatial periods close to third harmonic wavelength.

On the other hand, while self-assembly arguments, such as ones proposed in [52], [53] and [54], explain the periodicity of HSFL, extensions of such

arguments to explain the scaling of HSFL with irradiation wavelength as well as with the second and third harmonic wavelengths in the material may be difficult.

Chapter 4 Other Experimental Investigations

4.1 Introduction

This part of the thesis describes other preliminary experiments that were carried out and could potentially be useful for applications or research purposes.

4.2 Optical Fiber Applications

4.2.1 Introduction

The majority of the experiments described in the thesis are primarily performed for research purposes (i.e. to investigate the origin of ablation mechanisms or the generation of LIPSS). Ultrashort laser pulses are suitable for micromachining work where precision is required and minimal collateral damage is desired. Since optical fibers have a wide range of applications and are readily accessible, they would be a suitable choice for laser micromachining work. It might be possible to improve their functionalities in specific applications or develop alternative fabricating techniques by using ultrashort pulse laser processing. This part of the thesis reports preliminary work on two optical fiber applications using ultrashort pulse laser micromachining.

4.2.2 Removal of Metallic Coating on Glass Substrate

4.2.2.1 Introduction

The goal of this experiment is to determine the laser parameters (such as fluence of the irradiation pulses and translation speed of the sample during micromachining) which can cleanly remove a metal layer deposited on glass while leaving the glass undamaged. This is expected to be feasible since large bandgap dielectric materials such as glass generally have higher ablation thresholds than metals; it is possible to find a pulse energy or a range of pulse energies between the ablation thresholds of the two materials to achieve this goal. To provide some quantitative examples, the single-shot ablation threshold fluence for gold films when irradiated with a Ti:Sapphire ultrashort-pulse laser system had been reported to be ~700 mJ/cm^{-2} [85], while > 2 J/cm^{-2} had been reported for fused silica [87]. One of the potential applications of this experiment is to create slits on fiber end facets coated with a metallic layer. Having slits on the end of fibers can potentially eliminate the need for slits on other devices, such as spectrometers for example.

4.2.1.2. Sample Preparation and Experimental Setup

A Fisher Scientific Fisherbrand microscope slide was used as the glass substrates for this experiment (25×75×1 mm). A gold layer of approximately 180 nm in thickness was deposited onto the microscope slide using an Edwards

Sputter Coater S150B gold and carbon sputterer. The thickness of the gold layer was estimated by using a 15 nm/minute deposition rate, as indicated in the specification of the sputterer, for a total deposition time of 12 minutes. In comparison, the skin depth of the laser wavelength (800 nm) in gold is ~ 12.5 nm, and for typical telecommunication wavelengths of 1550 nm and 1310 nm are ~ 12.6 nm and ~ 12.5 nm, respectively [81]. The ~ 180 nm thickness for the gold layer provides an optically opaque coating at these wavelengths, which is essential for fabricating slits on fiber ends.

The laser micromachining on the samples was performed in vacuum. The laser pulses were focused perpendicularly on to the samples with a 5× microscope objective, yielding a nominal spot size of ~ 5 μm ($1/e^2$ radius) as extracted using the D^2 technique from previous experiments [62]. Pulse energies of 5 μJ to ~ 6 nJ were used. For each of the pulse energy employed, sample translation speeds of 500 μm/s and 1000 μm/s were used during irradiation to fabricate grooves in the gold layer. This yielded an effective number of shots per irradiated site, N_{eff} of ~ 13 for grooves machined at a translation speed of 500 μm/s and ~ 6 for 1000 μm/s, using Equation (3-6). Micromachined samples were studied using optical microscopy (OM) in both reflection and transmission mode.

4.2.2.2 Results and Discussions

Optical microscopy in reflection mode yielded better details of the gold layer due to its reflective nature, whereas transmission mode allowed better examination of the transparent glass substrate. The set of grooves machined with

a sample translation speed of 500 μm/s were first examined. At pulse energies of 910 nJ and above, peeling of the gold layer surrounding the irradiated region and deep damage to the glass were evident (Figure 4-1).

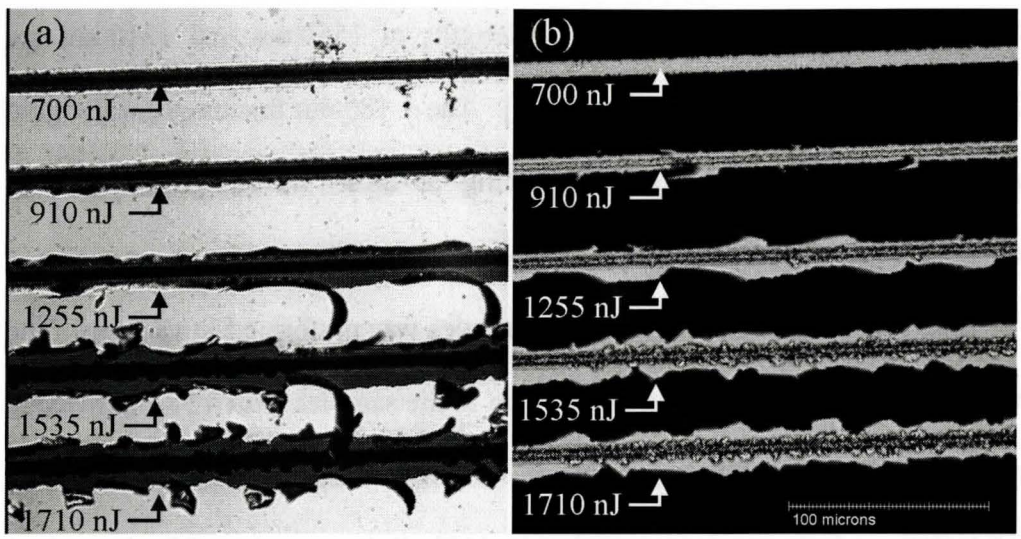

Figure 4-1: OM images of (single pass) grooves micromachined at various pulse energies, as labeled, at a translation speed of 500 μm/s. At pulse energies ≥ 910 nJ peeling of the gold is observed. (a) Reflection mode, the white part is the gold layer, the grey and black parts are the glass substrate. Peeling of the gold is easily observed using this microscopy technique. (b) Transmission mode, the black part is the gold layer and the white part is the glass substrate. Damage to the glass substrate is easily observed using this microscopy technique. Clean gold removal without significant damage is observed at 700 nJ in the above images.

Pulse energies of 700 nJ to ~390 nJ yielded what appeared to be the cleanest removal of the gold layer while the glass layer did not appear to be significantly damaged. Pulse energies of 290 nJ and lower yielded grooves in which islands of remaining gold are suspected to be present (Figure 4-2).

Grooves micromachined with a sample translation speed of 1000 μm/s showed results similar to the case where the sample was translated at 500 μm/s.

However, with the faster translation speed, the effective number of pulses per irradiated region (thus the laser energy deposited per region) is decreased. With a translation speed of 1000 μm/s, peeling of the gold layer surrounding the ablated region was evident for grooves irradiated with pulses having energies of 1.26 μJ and above. Irradiation with pulse energies of 700 nJ to ~390 nJ also yielded the cleanest removal of the gold layer while keeping the damage to the glass substrate minimal. Irradiation with pulse energies of 290 nJ and lower left islands of gold in the irradiated region.

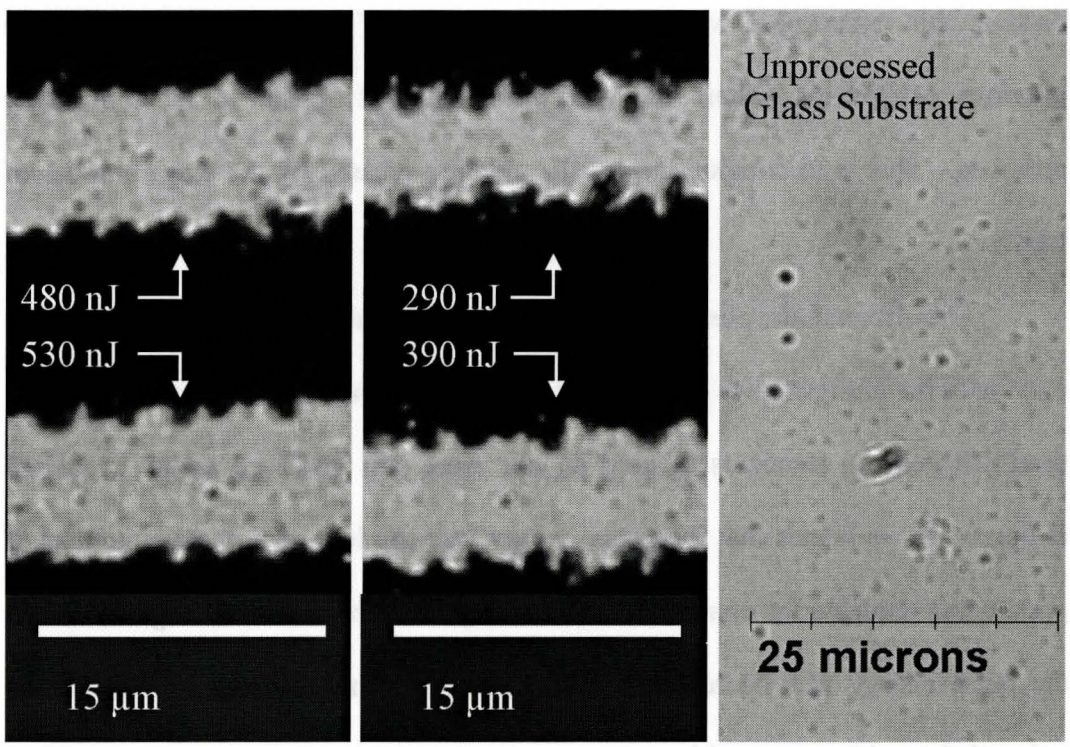

Figure 4-2: OM images (in transmission mode) of a blank glass substrate (right) and single-pass grooves machined at 500 μm/s with pulse energies as labeled. At 290 nJ (and lower energies), clumps of gold appear in the middle of the groove, indicating an incomplete removal of gold layer from the glass.

A follow-up experiment was performed to further investigate micromachining parameters in hope to produce a more regular removal edge of the gold. This may be feasible by lowering the pulse energy and irradiating the same area more than once. This experiment employed a translation speed of 1000 μm/s and energies decreasing from 150 nJ to 50 nJ. The sample was translated back and forth a different number of times when being irradiated, making multiple passes over the same irradiated regions. One to ten passes were used at each pulse energy to investigate the effect on ablation using a different number of passes on the gold layer and the glass substrate. Note that the energies used in this experiment were in the lower range of energies employed in the previous experiment, where the gold layer did not appear to be completely removed. This is to compensate for the ablation created by the extra number of passes.

One immediate observation made from the above experiment was that even with the highest pulse energy used (150 nJ) and the highest number of passes used (10 passes), remnants of gold islands were still observed in the irradiated region. This indicates that the pulse energy was too low, or a higher number of passes was required for complete removal of gold in the irradiated region. When the pulse energy was decreased from 150 nJ and/or the number of passes was reduced from 10, more gold remnants were found, showing that more ablation was required to completely remove the gold layer.

Overall, within the laser conditions tested in this experiment, a range of energies were found to remove the gold layer while keeping the surface of the glass substrate from being significantly damaged. However, there is still room for improvement. For example, even in the cases where the gold layer did not peel off, the edges of the gold layer appeared to be irregular. For future work, it might be worthwhile to investigate the deposition of the metallic layer or multiple layers using different metals to improve adhesion. Different ablation techniques can be tested for future work. For example, irradiation with pulses in the picosecond range might provide a gentler ablation process due to the decreased intensity for the same irradiation fluence, or temporal shaping of the pulses may be considered [89-98]. More details concerning ablation and micromachining with picosecond pulses as well as temporally tailored pulses are provided in Section 4.3.4.

4.2.3 Removal of Metal Coating on Fiber Facets

4.2.3.1 Introduction

The previous section described the difficulties in obtaining an optimized ablation condition to remove gold cleanly while leaving the glass surface unaffected. Despite this finding, attempts were made to use laser micromachining to remove gold layers deposited on to the ends of cleaved fiber sections as a proof-of-concept experiment. Also, first attempts were made in exploring the techniques required to fabricate slits on fiber ends.

4.2.3.2 Sample Preparation and Experimental Setup

Currently there is no extra port in the machining chamber to feed through optical fibers for machining. To modify a chamber for a feed-through while at the same time designing it such that the chamber still functions as a vacuum chamber was not attempted for this experiment. Instead, since this was merely an exploratory experiment, only short sections of optical fibers (that could be mounted and fit inside the machining chamber) were utilized.

The sections of fibers used in this experiment were cleaved from a spool of Newport F-SV-10 single-mode fiber, with a core diameter of 4 μm, a cladding diameter of 125 μm, and a diameter of 250 μm with the protective jacket. The jacket of the fiber was stripped using Micro Electronics Inc. Micro-Strip 125/250. The fiber stripper is designed for fibers having 125 μm claddings and 250 μm coatings. Stripped portions of the optical fiber were subsequently cleaved into approximately ½-inch sections using a PK Technology FK12 Angled Fiber Cleaver. Two ½-inch SEM stub mounts were glued together such that the mounting surfaces are in contact. A piece of double-sided carbon tape, frequently used for SEM sample mounting, was wrapped around a pin of one of the stub mounts. The short sections of the optical fiber were attached onto the double-sided carbon tape, with the sections parallel to the pin and with the ends of the sections protruding above the pin. The stub mounts assembly was placed in a home-made SEM stub holder using Struers Epofix, fabricated by Travis Crawford. Along with the stub mount holder, the entire assembly was placed in

the Edwards Sputter Coater S150B gold and carbon sputterer where a gold layer was deposited. Using a deposition rate of 15 nm/minute and a total deposition time of 12 minutes, a 180 nm layer of gold is expected. However, the specified deposition rate was calibrated for a working distance of 30 mm. Given the height of the fiber-mounting assembly, the fiber facets are roughly 20 mm higher than the calibrated height and a higher deposition rate (thus a thicker layer of gold) was expected. The exact thickness of the deposited gold layer would not have be a significant issue for this application since the only requirement was to obtain an optically opaque layer of metal. However, the thickness of the gold layer being different from that used in the experiment presented in Section 4.2.2 would possibly change the irradiation condition required to remove the gold layer while keeping the glass from begin damaged. Figure 4-3 shows the fiber-mounting assembly

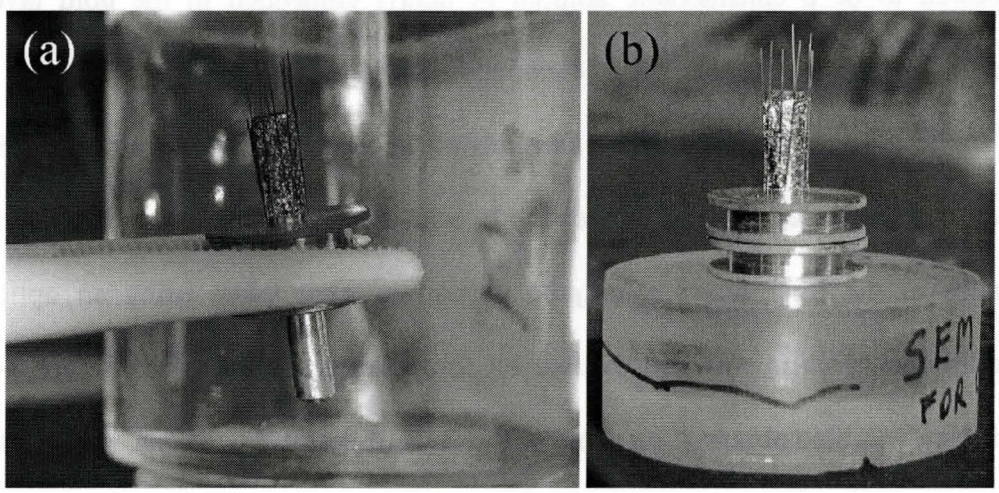

Figure 4-3: Homemade vertical mount for sections of optical fiber. (a) Two SEM stubs with the mounting surfaces secured together, with fibers attached to a pin using double-sided carbon tape. (b) The stub-mount assembly held in place in a holder made from

Laser micromachining was performed in rough vacuum (~0.05 mbar). The laser pulses were focused on to the sample using a 5× microscope objective, providing a spot size of ~5 μm ($1/e^2$ radius) as extracted in previous experiments using the D^2 technique [62]. A pulse energy of 710 nJ was used to machine the gold layer deposited on the ends of the fiber sections. This energy is roughly the same as the highest energy used in the experiment in Section 4.2.2 that provided a clean removal of the gold layer while no significant damage was found on the glass substrate. The laser was scanned across the machined surface a rate of 500 μm/s.

4.2.3.3 Results and Discussions

Preliminary results showed that the gold layer did not adhere to the ends of the fiber well, as part of the gold seemed to have peeled off. Also there appeared to be a considerable amount of debris embedded in the gold layer, possibly resulting from the lack of cleaning following the cleaving process.

In a follow-up experiment, the ends of the fiber sections were blown with a jet of compressed air and wiped lightly with methanol to remove the debris. Images of the fiber facets after gold deposition were taken using an optical microscope. Debris was still evident on some facets, as shown in Figure 4-4. Chipping was also observed on some of the ends of the fiber sections. This could merely be a matter of the user being inexperienced with the use of the fiber cleaver.

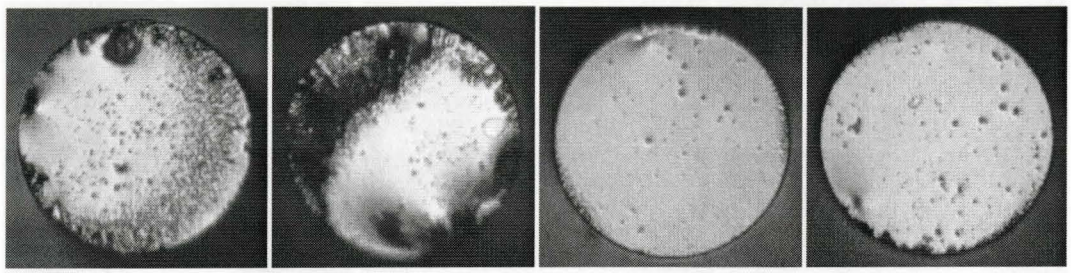

Figure 4-4: OM images of some fiber facets coated with gold, showing a range of surface qualities obtained. The diameter of the fibers (with the protective coating stripped, as shown in the images) is 125 µm.

From the previous experiment (Section 4.2.2), it was found that optical microscopy using reflection mode provides more details of the reflective gold layer, while transmission mode yields more details in the transparent glass substrate. However, due to the geometry of the mounting, it was not possible to employ transmission mode in the optical microscope. Reflection mode was the only option for OM to investigate the micromachined regions.

Different patterns were micromachined on the end facets of the gold-coated fibers, including a single-slit, 4-slits "grating", two perpendicularly intersection slits (forming a "+" sign), and a series of slits with close spacing between each to remove the gold layer in a rectangular section (Figure 4-5). A closer inspection showed that the center portions of the grooves, corresponding to irradiation with a higher local fluence assuming a Gaussian pulse beam profile, showed signs of damage to the glass. While it is uncertain if all of the patterns would have useful applications, closely-spaced and intersection features are good ways to test the adhesion of the gold.

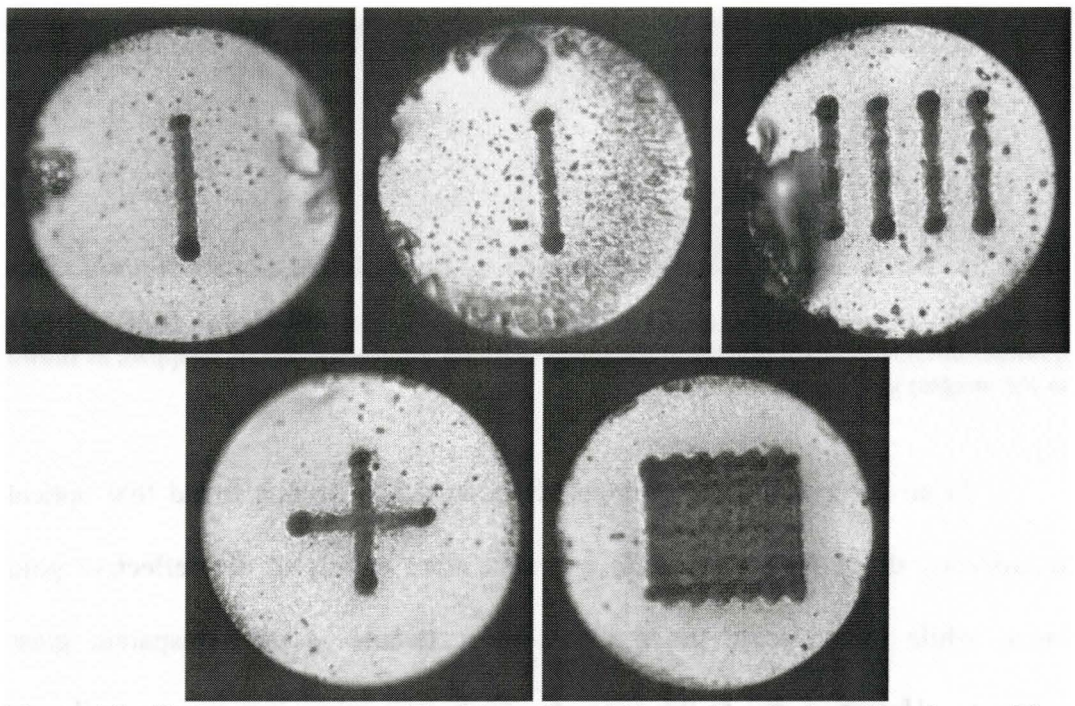

Figure 4-5: Various patterns machined into the gold layer deposited on fiber facets. First observation indicated that deeper regions are machined near the end of the grooves due to the micromachining stage accelerating/decelerating near the end of the translation. The fibers (with coatings stripped off) have a diameter of 125 µm.

In all cases the edges of the region where the gold layer was removed appeared to be rough and irregular This is not desirable for applications as exit slits since the irregularity could cause unwanted scattering of the light. Also, at the ends of the slits, stronger ablation is observed, most likely due to a slower sample translation rate. This slower translation rate exists since the motorized stage accelerates and decelerates at the beginning and end of the translation. The micromachining software can be modified such that the shutter opens to allow the laser pulses through only when the translation stage under the micromachining chamber is traveling at a constant speed (i.e. after acceleration and prior to deceleration).

While many improvements need to be made before a well-fabricated exit slit on the fiber ends can be obtained using laser micromachining, this experiment showed that it is likely feasible. Future investigations could be carried out to explore cleaning procedures for the fiber ends following the cleaving process. In addition, perhaps using a different metallic layer to enhance adhesion may improve the irregular edges in the ablated region. Finally, microscopy techniques where better observations of the quality of the glass in the fiber facets should be employed in future work.

4.2.4 Micromachining of Fibers

4.2.4.1 Introduction

Another possible application of laser micromachining on optical fibers is to use ultrashort laser pulses to remove or shape certain sections of the fibers. For example, if certain sections of the cladding of two fibers are removed and the fibers are brought close together, coupling of the light from one fiber to the other can be feasible. A similar scheme scan be establish for coupling of light between a fiber and a planar waveguide. Recently the removal of a length of fiber cladding for such applications has been achieved by means of mechanical polishing [e.g. 98-101]. Applications such as fiber Mach-Zehnder interferometer might be feasible. Another example is to create a V-shaped notch into the core of the fiber through the cladding such that the "V" is perpendicular to the central

axis of the core. Such V-notches are often created with mechanical means, and can be used for coupling of pump light from the side of the fiber to amplify seed pulses propagating in the core ("side-pumping" technique) [e.g. 103, 104]. Beveling of fibers might also be feasible with laser micromachining. Beveled-end fibers can be used to spatially shape laser beams, for example [105]. A shaped surface on the fiber facet might be helpful in coupling of light as well [e.g. 106-109]. In all cases, laser ablation conditions that can cut through the fiber while minimizing collateral damage is essential and needs to be determined. This part of the thesis reports preliminary experimental results on investigations of different ablation conditions and suggestions for future improvement.

4.2.4.2 Sample Preparation and Experimental Setup

The preparation of the fiber sections was identical to the process described in Section 4.2.3.2.

Since the goal of this experiment is to cut through the fibers, extra measures had to be taken to ensure we do not ablate the sample stage once we cut through the fiber. In an early experiment the sections of cleaved fibers were taped on both ends onto a glass microscope slide, exposing the central portions for ablation. However, it is possible that when the laser ablates through the fiber and cut slightly into the microscope slide, the molten material between the fiber and the glass slide can be fused together as they resolidify. To ensure that this does not happen, a mounting platform was devised for subsequent experiments to

suspend the mid-sections of the fibers in air while the ends of the fibers were secured to this platform. A simple platform was built with four microscope glass slides forming a square shape with the corners secured together using instant glue, and reinforced with Scotch Tape. Sections of the fibers were placed across two sides of this square platform and were secured to the glass slides using Scotch Tape.

Laser micromachining was performed in rough vacuum (~ 0.05 mbar). In some experiments the laser pulses were focused on the sample using a 5× microscope objective, providing a spot size of ~5 μm ($1/e^2$ radius) as extracted from previous experiments using the D^2 technique [62]. Some of the experiments used a lens with 75 mm focal length which yields a spot size of ~13 μm, in order to obtain a larger Rayleigh range (distance away from the focal plane where the spot size is expanded by a factor of $2^{1/2}$ compared to the spot size at the focal plane). The Rayleigh range is described by the equation [110]:

$$Z_R = \frac{\pi \omega_o^2}{\lambda} \qquad (4\text{-}1)$$

where Z_R is the Rayleigh range, ω_o is the beam waist, and λ is the wavelength of light. From the calculated spot sizes, Equation (4-1) yields a Rayleigh range of ~98 μm for focusing of 800 nm light using a 5× microscope objective, and ~664 μm when a 75-mm-focal length lens is used. The confocal parameter ($2\,Z_R$, described by the two Rayleigh ranges centered at the focal plane of the lens) for

the lens is much larger than the diameter of the fiber. This is the preferred situation for experiments where the goal is to cut through the fiber.

To cut through the fiber, "grooves" were cut into the fiber repeatedly ("multiple-passes") in the hope to obtain very deep grooves until the depth reaches the diameter of the fiber. In this study, we explored different micromachining conditions to cut these grooves, such as variable pulse energies, different numbers of passes (number of time the grooves are cut in to the same region), different shapes (notches and arcs) and various focusing schemes. The focal plane of the lens was moved into different depth of the fiber to study whether the position of the focal plane has an effect on the micromachined features.

Pulse durations of 1 ps, 3 ps, 10 ps and 20 ps were also used to investigate the effect of longer pulses on the morphology of the ablated regions. A "pulse train" was also utilized to machine the fiber in order to investigate the effect of ablation with a train of weaker pulses, where the pulse energy increases with each subsequent pulse and starts to drop off after a maximum pulse energy is reached. Discussions concerning ablation with picosecond pulses and other temporal manipulation schemes, including the pulse train, are presented in Section 4.3.4. The pulse train used in the experiment had a series of ~10 pulses, and had ~7.5 ns separation between each pulse. Pulse compression was optimized for the peak pulse which had a duration of ~150 fs at the output of the CPA. Pulses leading and trailing the peak pulse in the train are expected to have a duration longer than

~150 fs. This separation corresponds to a repetition rate of 133 MHz. A pulse train can be obtained by disabling the output Pockels cell inside the CPA (refer to the description of the CPA in section 2.2.1.3) such that the pulse being amplified in the CPA is not switched out of the cavity by the Pockels cell (refer to Section 2.2.1.3.2 for CPA operation details). Instead, a half-wave plate was placed in the beam path just prior to the polarizer to rotate the polarization of the pulse thus ejecting part of the energy each time the pulse makes a round trip in the amplifier cavity.

4.2.4.3 Results and Discussions

To demonstrate the effect of changing the height of the focal plane, two adjacent grooves were machined on the fiber with one machined with the laser pulses focused on to the top of the fiber and the other focused at the bottom of the fiber. These grooves were machined with 100 passes with a pulse energy of 5 μJ at a speed 500 um/s, using a 5× microscope objective. Under the optical microscope only the groove machined with the laser focal plane at the top of the fiber damaged the fiber. Figure 4-6 presents an optical microscope image of the two grooves.

A side-view optical microscope image revealed that the groove was not deep enough to cut through the fiber (Figure 4-6). This indicates that either a higher number of passes or a higher pulse energy was required. Note that the results shown in Figure 4-6 were from the first preliminary experiment where the sections of the fiber were placed directly on a glass slide (rather than having the

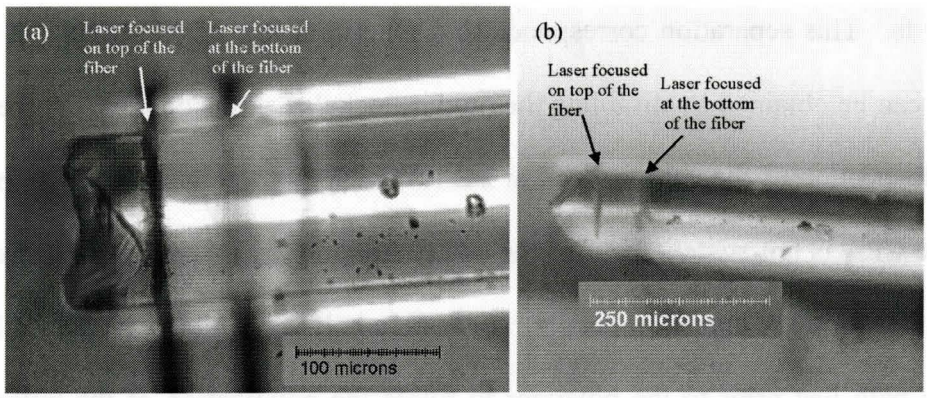

Figure 4-6: OM images of grooves micromachined into the fiber with 5 μJ, 150 fs laser pulses translating at a speed of 500 μm/s. 100 passes are used to machine the grooves. With these laser conditions, the grooves were not deep enough to cut through the fiber. A 5× microscope objective was used to focus the beam. The diameter of the fiber was 125 μm.

mid-sections being suspended). Different number of passes and different focusing regimes were also tested.

In a subsequent experiment, using a lens with 75 mm focal length, a groove was machined with 200-passes at a pulse energy of 15 μJ and a sample translation rate of 500 μm/s, with the laser focal plane aligned to the top of the fiber Two more grooves were machined with the same pulse energy and sample translation rate with 100 passes, one of which was machined with the laser focal plane aligned to the top of the fiber while the other one was machined with the focal plane set to 100 μm below the top of the fiber None of the above micromachining conditions provided a groove that appeared to cut through the fiber successfully

A drawback also observed was the "v" shape appearing in the grooves (Figure 4-7), which results from the lower ablation rate in the deeper region of the

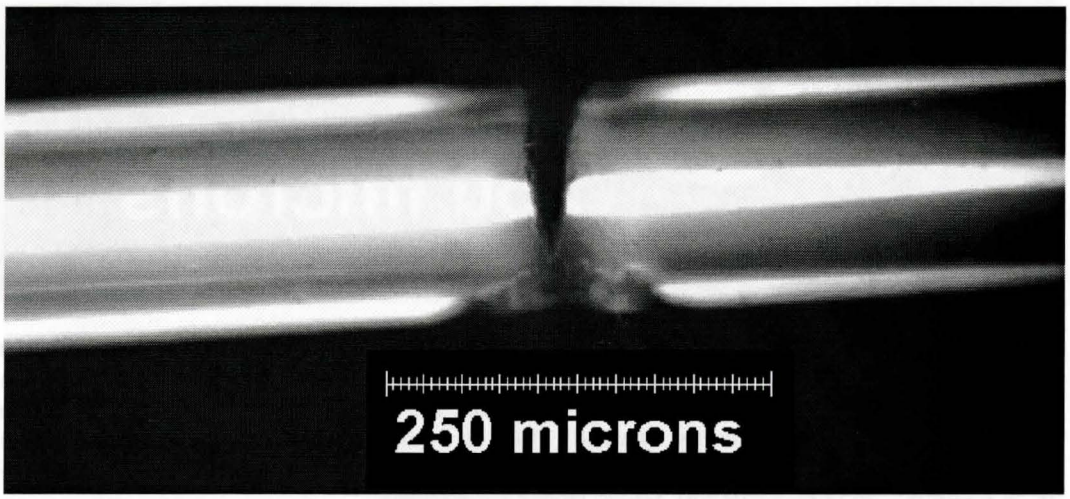

Figure 4-7: OM image of a groove micromachined into the fiber with 15 μJ, 150 fs laser pulses translating at a speed of 500 μm/s. 100 passes are used to machine the grooves. The laser focus was set at 100 um below the top of the fiber. With these laser conditions, the groove was not deep enough to cut through the fiber. Damage was also observed on the bottom of the fiber. A lens with 75 mm focal length was used to focus the beam. The diameter of the fiber is ~125 μm.

grooves, due to a possible material redeposition or scattering of light from the sidewalls of the grooves.

In some cases where the laser micromachining did not cut through the fiber, the grooves could act to initiate cleaving and breaking the fiber into sections either from subsequent handling or during the machining process from the movement of the motorized stages. In those cases the laser machined regions appeared to be much rougher than the cleaved region (Figure 4-8, for example). This roughening of the surface is undesired since smooth facets are essential for optical fiber applications.

Another effect investigated was the morphology of the micromachined regions on the fibers after ablation. Since the quality of the facets greatly affects the coupling and output efficiency of the fiber, a high quality facet is required after ultrashort pulse laser processing. Twenty single-pass grooves with different

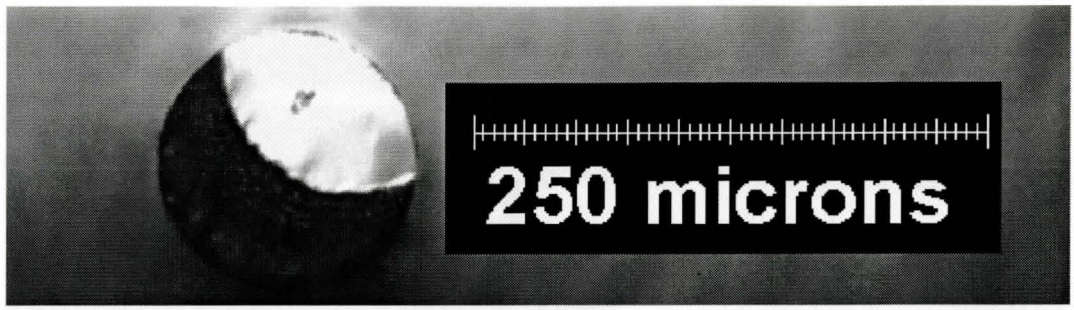

Figure 4-8: Fiber cross-section of a groove machined with 15 μJ, 150 fs laser pulses with 200 passes, focused onto the top of the fiber at the time of laser machining (roughly the bottom left area of the fiber in this image). It is suspected that the groove had initiated a cleave when the fiber was subsequently handled. The cleaved surface (the white portion in the cross-section) appears to be of much higher quality than the laser-machined surface (the black portion in the cross-section), which shows roughening.

pulse energies were machined into the fiber, perpendicularly to the intended light propagation axis of the fiber. Observations are made with optical microscopy and it appeared that irregularity and chipping occurs as a result of ablation (Figure 4-9), which is undesirable.

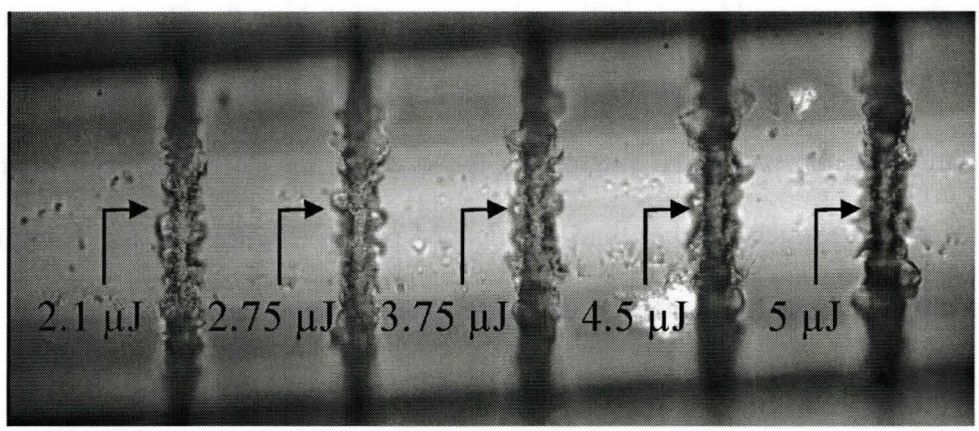

Figure 4-9: OM images of single-pass grooves machined with a translation speed of 500 μm/s at different pulse energies as labeled. Cracking introduced by the machining is evident. The laser pulses have a duration of ~150 fs and are focused with a 5× microscope objective.

It is possible that the localized pressure introduced by the intense ultrashort pulse may caused this type of unwanted damage. During ultrashort pulse laser ablation, a few hundred MPa to a few thousand GPa of pressure can develop in the material [19, 23, 24, 27]. To reduce the intensity of the ablation pulses while maintaining a similar pulse fluence, longer pulse durations can be used. For example, when the irradiation pulse width is stretched from 150 fs to 3 ps, the damage threshold fluence only increases by a factor of ~2 [65-68], but the threshold pulse intensity would decrease by a factor of 20. In a subsequent experiment (which used a lens with 75 mm focal length) 1 ps and 3 ps pulses were used to machine the fiber and the results were compared to the ablated regions obtained using 150 fs pulses. It was observed that cracking and chipping were more prominent when the pulse duration increased (Figure 4-10). Further discussions regarding ablation of dielectric material with different pulse durations are presented in Section 4.2.4.4

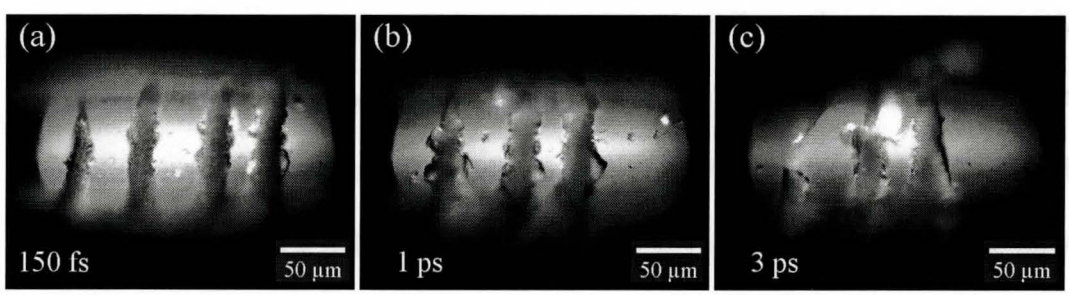

Figure 4-10: OM images of single-pass grooves machined with a translation speed of 500 µm/s with different pulse energies (Starting from the right for each image: 15 µJ, 13.5 µJ and 8 µJ (and 6 µJ, for the 150 fs case)). It was found that as the pulse duration is stretched from (a) 150 fs to (b) 1 ps, chipping became more severe. At (c) 3 ps, chipping was severe enough to causes inconsistent groove widths. Cracking was also observed at this pulse length. The laser pulses are focused with a 75 mm lens, yielding a spot size of ~ 13 µm.

A "pulse train" (a series of pulses), as well as 10 ps and 20 ps pulses were used to machine the fibers as well (with a 75 mm-focal length lens). A pulse-train ablation technique was reported in the literature to improve the quality of the ablated region [91-93]. However, this experiment was not successful due to difficulties with accurately judging the height of the laser focus, perhaps due to cylindrical shape of the fiber and the long focal length lens, likely in combination with sagging of the midsection of the suspended fiber. The grooves seemed to be embedded inside the fiber, making observation by microscopy impossible without elaborate cross-section techniques.

As mentioned above, due to the cylindrical geometry of the fibers, it is difficult to accurately judge the height of the laser focus relative to the fiber using the viewing camera in the machining setup (refer to Section 2.2.2 for a schematic of the laser micromachining setup). To explore how well alignment can be made, a v-shaped notch and a semi circular were are machined on to the fiber with the focus of the laser roughly at the top of the fiber using a 5× microscope objective. Attempts were made to align these features such that the tip of the "v" and the arc are located at the center of the fiber. Figure 4-11 presents an optical microscopy image of such features machined in to the fiber. These shapes awerere machined with 50 passes at a pulse energy of 5 μJ and a translation speed of 500 μm/s. V-notches are sometimes used in fiber applications where light needs to be coupled into the fiber from the side [106-109]. However, laser parameters allowing

grooves that cut through the fiber need to be determined before such applications can be realized.

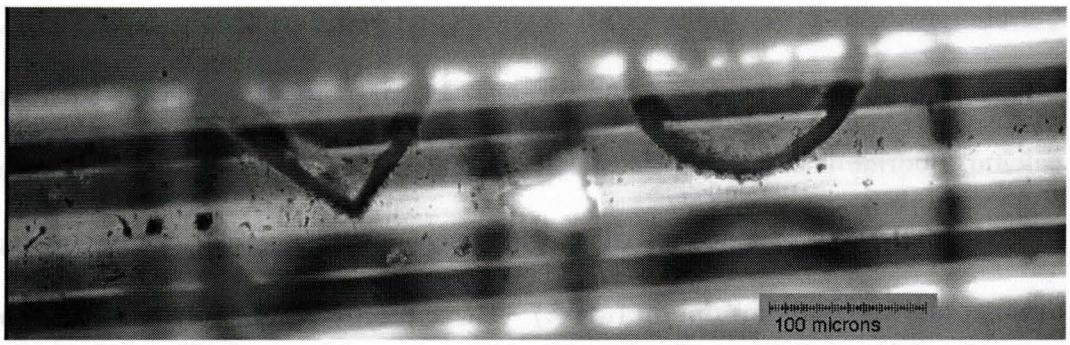

Figure 4-11: OM image of features machined into the fiber with 5 μJ, 150 fs pulses at a translation speed of 500 μm/s, using 50 passes. The laser pulses are focused with a 5× microscope objective.

4.2.4.4 Discussions Concerning Improvement of Optical Fibers Micromachining Using Temporal Manipulation of Laser Pulses

Based on experimental work performed for this thesis, as presented in previous subsections, major improvement in the morphology of glass resulting from micromachining is required before some of the intended applications may be feasible. Different schemes of temporal manipulation of laser pulses have been reported to improve the morphology of ablated or micromachined features in different materials [89-98]. Temporal manipulation can include simply varying the pulse lengths [89, 90], double-pulse [94-98], triple-pulse [96] and quadruple-pulse [92] ablation, or by using a pulse train (a series of pulses with a close temporal spacing) with >130 MHz [91-93], or THz repetition rate [96]

Depending on the electronic, crystal and physical structures of the material, picosecond laser processing might produces a smoother final morphology with fewer defects over femtosecond and nanosecond laser pulses. Materials with wide-bandgaps and strong electron-phonon coupling, such as calcium fluoride and amorphous silicon dioxide, are examples of such materials [89, 90]. In such materials, initial optical absorption creates electron-hole pairs through multi-photon absorption (MPA). These electron-hole pairs are prone to cause defects such as self-trapping excitons and Frenkel defects on a picosecond time scale [89, 90]. When a significant free-electron density in the conduction band and the density of defect (such as self-trapping excitons and Frenkel defects) is reached, single-photon absorption (SPA) becomes favored over MPA and can cause efficient local heating of the crystal [89].

In the above-mentioned materials, deformations and fractures may be caused by irradiation with subpicosecond pulses. When subpicosecond pulses are used, deposition of the optical energy into the material takes place before the conditions for efficient SPA is developed, thus MPA is the dominating process. In this case, localized excitons can weaken or destabilize the bonds of the crystal and create a considerable amount of stress to cause deformations and fractures [89, 90]. Howerver, when a picosecond pulse is used, smoother features may be obtained. During irradiation with a picosecond pulse, the leading part of the pulse establishes conditions that subsequently favor SPA. As the free-electron density reaches $\sim 10^{21}$ cm^{-3} [89], SPA due to free carrier absorption and through defects

(such as self-trapping excitons and Frenkel defects) becomes significant. At this point the trailing part of the pulse can efficiently heat up the crystal lattice to cause melting and vaporization of the material [89, 90], causing the material to "soften" and resulting in a smooth final morphology. As the pulse duration is further increased to the nanosecond range, fractures of material surface can be prominent again [89]. The cause for the fractures in nanosecond-pulse irradiation was attributed to the significant lateral heat diffusion during optical energy deposition, causing a shear stress to develop due to temperature gradient in a volume [89, 99]. Depending on the electron-phonon coupling strength of the material and the density of defects already existing in the material, the above descriptions may not be universally applicable.

Based on the arguments above, picosecond pulses were used to machine optical fibers, as reported in the previous subsections. However, it was observed that in the case of optical fiber laser machining, stretching of the pulse length to the picosecond-range caused more cracking and fracturing of the material than subpicosecond pulses. Pulses with < 100 fs durations were shown to improve the surface morphology of ablation craters [102]. This result was attributed to a stronger multiphoton absorption leading to a shallower light penetration depth [102]. The higher light penetration depths when longer pulses are used can allow to mechanical relaxation process in the glass (instead of direct material removal), causing roughening of the surface [102].

A double-pulse ablation scheme has also been shown to reduce cracking resulting from ultrashort pulse laser micromachining. Microcracks developed at the bottom of the grooves resulting from ultrashort pulse laser micromachining were eliminated by using a double-pulse ablation scheme, with a 10 ps separation between the pulses [98]. The improved feature from double-pulse ablation is considered to result from the first pulse softening up the material before the second pulse arrives at the material surface, allowing a more "gentle" process of material removal [97]. Such a technique might provide improved micromachining features on optical fibers. More detailed discussions on double-pulse ablation can be found in Section 4.3.

Extending the idea of having a pulse softening up the material (such as double-pulse ablation), pulse trains (a series of pulses that are closely spaced temporally) have also been used to demonstrate improved surface morphologies following laser micromachining [91-93]. Typical pulse trains reported in the literature have a repetition rate of 133 MHz. In [91], holes ablated with pulse trains did not show signs of fractures, cracks or swelling, which were observed with a multiple pulse ablation (at 1 Hz repetition rate). The improved surface morphology was attributed to heat cumulating between the pulses, improving the ductility of the surrounding material and thus reducing shock-induced cracking and fracturing. It might be worthwhile to reattempt micromachining with a pulse train on optical fibers to try to improve the final morphology (Refer to Section

4.2.4.3). Details of the generation of a pulse train from Ti:Sapphire CPA available in this laboratory was provided in Section 4.2.4.2.

Comparing the temporal distribution of the optical energy, a pulse train ablation scheme may provide better features than a double-pulse ablation scheme. The optical energy is distributed into more successive pulses in a pulse train, it may allow a "gentler" ablation than a double-pulse scheme.

4.3 Double-Pulse Laser Ablation of Silicon

4.3.1 Introduction

A "double-pulse" technique has been employed by various research groups and is reported to improve the final morphology of ablated regions and to avoid cracking in dielectric materials as well as thin semiconductor samples [94-98]. In this technique, an incoming laser pulse is typically separated into two pulses which are both used to irradiate the sample surface. An optical-delay line can be placed in the beam path for one of the pulses to create a variable delay between the two pulses. A Michelson interferometer-based second-order autocorrelator can be used for double-pulse generation. However, more elaborate temporal shaping of the pulses can be carried out by modulating the beam paths for different spectral parts of the pulses in the stretcher of the CPA. Using this technique, as the beam is recollimated at the output of the stretcher, where the spectral components are spread out in time, the spectral modulation in the stretcher will result in an amplitude modulation in time [95]. This technique allows more versatility in the temporal shaping of the pulses (both double-pulse and triple-pulse ablation scheme were demonstrated in [95]). A quadruple-pulse ablation scheme obtained by cascading two Michelson interferometers was also demonstrated [92]. The improved surface features in double-pulse ablated craters are due to the separated pulses allowing less stress accumulation, since the total

irradiation fluence is separated in time; the leading pulse can act to soften the material [97].

As mentioned in Section 2.1, the exact mechanisms responsible for ultrashort pulse laser ablation are still a topic of discussion in the literature. This double-pulse technique can be adopted as a tool to investigate the state of the material at different time frames after the incidence of the first laser pulse [111]. This can be achieved by adjusting the delay of the arrival of the second pulse. The final morphologies of the sites irradiated with double pulses having different relative delays can provide insights into the ablation mechanism.

4.3.2 Experimental Setup

Although the beam delivery and attenuation scheme is similar to the description in Section 2.2.2, for this experiment additional optics were required to set up the double-pulse ablation technique. Section 2.3.1 described a second-order noncollinear autocorrelator that is typically used to measure pulse durations. Such a setup contains components to split an incident beam into two pulses and direct them to parallel paths before a lens (Refer to Figure 2-18). Also placed in the autocorrelator is a motorized and computer controlled stage that allows one of the mirror to be translated, creating an optical delay line to control the relative delay between the two pulses. These components form the basis of the double-pulse technique. For this experiment, the autocorrelator was modified to establish the double-pulse scheme. By removing the lens and the second harmonic

generation crystal in the autocorrelator, and adjusting the position of one of the mirrors, the beams can be combined collinearly at the output of the beam splitter. With the beam paths established, a variable delay between the two pulses can easily be controlled by adjusting the positioning of the mirror in the optical delay line. Figure 4-12 illustrates changes made to the autocorrelator to create the double-pulse ablation scheme.

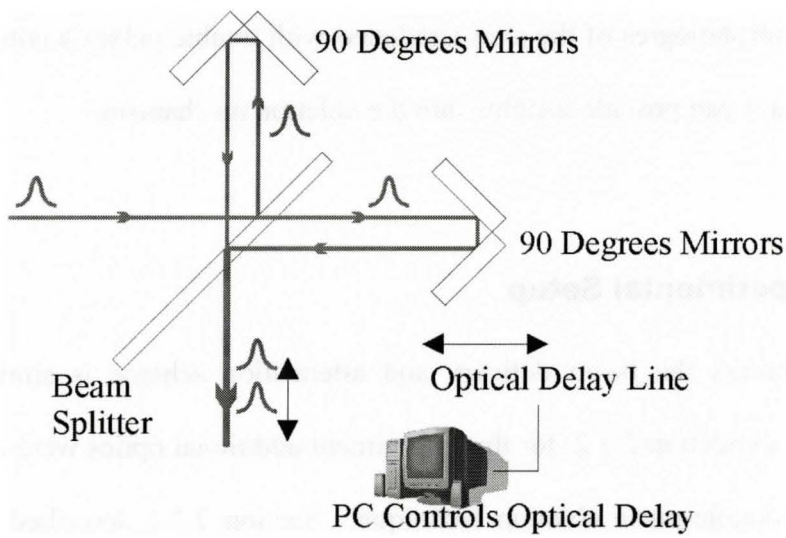

Figure 4-12: Symbolic representations of a double-pulse setup. The main modification to convert from an autocorrelator (refer to Figure 2-18) to a double-pulse setup is to translate the 90° mirror such that the pulses at the output side of the setup are collinear in the double-pulse setup.

To ensure that the beam paths of the output pulses from the double-pulse generation setup were collinear, fine alignment of the pulses was carried out by using a charge-coupled device (CCD) camera mounted at the machining chamber The mirror in the optical delay path was translated from one end of the translation

stage travel range to the opposite end so if there was any misalignment the two spots on the CCD camera would walk-off relative to one another.

In this experiment a ~280 μm thick silicon (100) sample was used as the irradiation target. A 5× microscope objective was used to focus the laser pulses such that they are incident on the sample surface perpendicularly. The 5× microscope objective yields a nominal spot size of ~5 μm ($1/e^2$ radius) as extracted using the D^2 technique. Pulse energies used in this experiment ranged from 2 μJ to 33 nJ per site for both single and double-pulse irradiation. For the double-pulse ablation, delays of 500 fs, 1 ps, 10 ps, 100 ps and 300 ps between the pulses were used. The longest delay provided by the translation stage in the double-pulse generation setup is about 330 ps. Single-pulse irradiation was performed as a benchmark, since this technique is our standard ablation scheme. To obtain a much longer pulse delay, the machining optics were converted back to a typical single-pulse setup, allowing two pulses with a 1 ms delay (corresponding to the repetition rate of the CPA output) in between the pulses to irradiate the surface. The energy of the pulses was adjusted such that total energy deposited for each irradiation site was constant. Observation of the irradiated sites was carried out on an optical microscope using the Nomarski technique.

4.3.3 Results and Discussions

The difference in the final morphology of sites irradiated using double-pulses with different delays were the most pronounced at the highest pulse energy

used. It is likely that there was a misalignment of ~2 μm on the sample surface between the two beam paths of the double-pulse setup, judging by the morphology of some of the craters. Overall the observations made from the morphologies of the ablation craters were mostly consistent with the general timescale described in Section 2.1.2 (as summarized in [29]). Single-pulse irradiated sites showed craters with relatively smooth bottom. As double-pulse ablation was used, a 500 fs separation between the pulses yielded craters with a very slight bump on the inside of the crater. The similar appearance in the bottom of the crater for double pulse ablation with a 500 fs separation and single-pulse irradiation suggests a somewhat unchanged crystal and electronic structure. This bump became more pronounced as the pulse separation as increased. The subtle bump at the bottom of the crater (due to the misalignment of the double-pulse setup) for double-pulse ablation with a 1 ps delay indicate softening of the material, possibly due to nonthermal melting or an initial stage of lattice heating. Ablation with double pulses having a separation from 10 ps to 300 ps showed increasing signs of heating and melting. At larger pulse separations (~50 ps and larger) it became evident that there were two sets of ablation crater rims, indicating that the two pulses in the double-pulse generation setup were not perfectly collinear. However, as the separation of the pulses increased to 300 ps, signs of melting and resolidification became more evident, suggesting a liquid phase in this time frame. A similar observation had been reported for fused silica where the morphology of craters ablated a double-pulse with 300 ps delay showed

indicative signs of a liquid phase [111]. Having two sets of rims due to the misalignment of the double-pulse beam paths might have aided in visualizing the state of the material as the second pulse is incident on the surface. At a much larger separation (1 ms), signs of melting were not evident. Instead, the morphology somewhat resembled that of single-pulse irradiation. However, the bottom portion of the craters appeared to be much rougher than that of single-pulse irradiated sites. This time scale is much larger than the reported resolidification time scale of a few tens to a hundred nanosecond [29 (and references therein), 16]. The material would have had plenty of time to cool and resolidify before the arrival of the second pulse. Figure 4-13 presents optical microscopy images of sites irradiated with a single-pulse, and a double-pulse at different separations between the pulses. Note the secondary outer rim shown in the figure for single-pulse ablation is likely due to material modification caused by the lower local fluence at the wing of the Gaussian beam which is not intense enough to cause ablation [112].

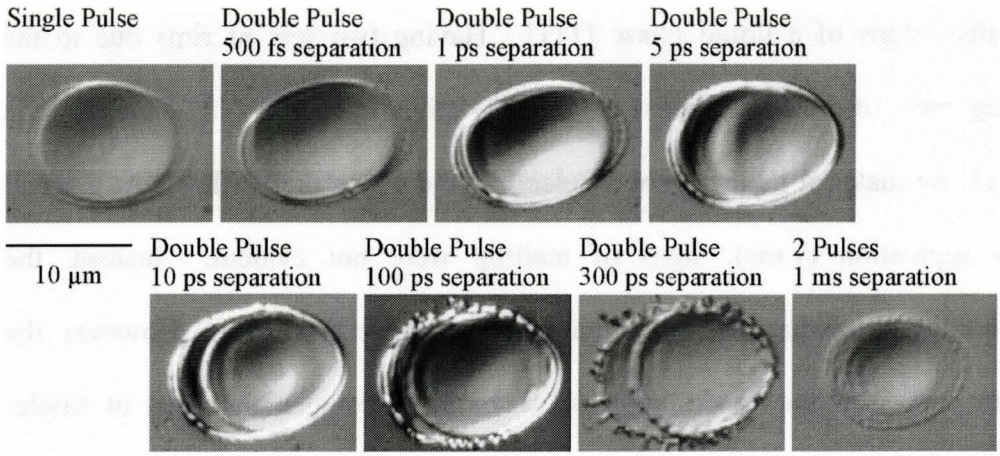

Figure 4-13: OM images summarizing observations made for single and double-pulse irradiations on silicon with different pulse separations as labeled above each site. The total energy used to irradiate each site is constant at 2 μJ. Pulse duration is ~ 150 fs.

Extensions of this experiment can include employing double-pulse ablation with finer time-delay steps to allow a more precise determination of the time scale over which ablation mechanisms take place. The same technique can also be employed over a range of materials (more specifically on metals, semiconductors and dielectrics) such that ablation mechanisms resulting through different means of optical absorption (refer to Section 2.1.2) can be studied.

4.3.4 Improvements and Future Work

This preliminary experiment demonstrated that the double-pulse technique can be used to determine the state of the material at different time frames after the incidence of the first pulse. However, there is much room for improvements and extensions. One immediate issue that needs to be addressed is the alignment technique. The CCD camera did not prove to be sufficiently accurate method to

align the two beam paths in this experiment. Other alignment techniques worth consideration might include the observation of interference fringes of the two pulses when the two splitting beam paths are made equal. Extending this idea further, one could send the double-pulse pulses through the SHG crystal collinearly and observe the fringes of the generated second-harmonic beams. Two-photon absorption on a photodetector can also be used as a tool to ensure temporal and spatial overlap of the two pulses [113].

A more elegant attenuation scheme can be introduced where the ratio of the energies of the two pulses can be adjusted, by attenuating one of the beams in the double-pulse generation setup for example. With this setup we would be able to send in a weak second pulse that does not actually induce significant damage, thus making observations at the time the second pulse is incident on the surface a less perturbing process. This setup could also be used to investigate an ablation scheme to improve the final morphology of the ablated features. For example, if a weak pulse is incident on the material surface first, it might be able to "soften up" the material surface such that the collateral damage caused by the ablating process of the second, stronger pulse might be reduced [88, 111]. A quadruple-pulse ablation setup using two cascading Michelson interferometers was demonstrated in [92]. One extension of such a setup is to insert extra optics to allow control of the fluence for each individual pulse. Comparison of single-, double- and quadruple-pulse, as well as pulse-trian ablation may be informative in terms of

determining mechanisms and related time frames of ultrashort-pulse laser ablation.

A similar setup can be adapted for pump-probe experiments as well where a weak probe-pulse can be sent in at a controlled delay after the first pulse. Information such as the time-dependent reflectivity may be extracted from such a technique, and carrier lifetime and refractive indices at different time frames may be deduced from such an experiment. Some other interesting extensions include a shadow-graph experiment [98, 114] to monitor the ejected material at different time frames of the double-pulse experiment. In a shadow-graph experiment a probe beam with a variable delay is shot across the sample surface onto a CCD camera such that the ejected material from the ablation casts a shadow on the CCD screen.

Future results from the above variation of expansion of the double-pulse setup can be tied in with proposed ablation mechanisms in the literature to further elucidate the processes of ultrashort pulse laser ablation.

There are other applications of the double pulse technique as well. Ejection of ions is reported to increase using double-pulse irradiation, and ion beam, as well as x-ray generation applications might be feasible [94, 115]. Fringes from the interference pattern between two collinear pulses can be used to create grating structures as well [116].

Chapter 5 Concluding Remarks

This thesis presents experimental works related to the physical studies of interactions of ultrashort laser pulses with materials.

Much effort was directed toward the study of laser induced periodic surface structures (LIPSS) that are observed on material surfaces after irradiation with laser pulses. More specifically, emphasis is placed on LIPSS with spatial periods much smaller than the wavelength of the irradiating laser pulses. These high spatial frequency LIPSS, or HSFL, are typically generated when a site is irradiated with multiple pulses with a laser wavelength that corresponds to a photon energy less than the bandgap of the material, and only occur in a specific range of fluences and number of pulses per irradiation site. The exact conditions depend on the material.

The exact formation mechanism of HSFL is still under discussion in the literature. A study on the dependence of HSFL formation on gallium phosphide on the pulse duration showed that HSFL can be generated over a large range of pulse durations (HSFL were observed for irradiation with 150 fs – 80 ps pulses), suggesting that its formation is insensitive to the pulse duration and intensity. A cross-sectional TEM study gallium phosphide on specimens prepared by focused ion beam milling showed that the inner portions of the HSFL protrusions have the

same crystal structure and orientation as the bulk, indicating that the material is unmodified in these regions.

Although no HSFL formation models are developed based on the experimental findings included in this thesis, the results may be tied into existing proposed theories. Experimental studies reported in this thesis favor some of the suggested mechanisms in the literature. More specifically, the scaling of HSFL spatial periods with irradiation wavelengths, as well as the observation of HSFL spatial periods approaching second harmonic wavelengths (in gallium phosphide, sapphire, as well as reports on other materials in the literature), or third harmonic wavelength (in sapphire) favors the idea of higher harmonic generation at the material surface as a contributing mechanism for HSFL formation. At the same time, this very observation may point to shortcomings in other proposed mechanisms in the literature such as the self-assembly model. Future work that may contribute to the elucidation of HSFL origin include a systematic study of simultaneous irradiation of fundamental and frequency doubled pulses. On another hand, sub-surface crystallographic analysis of sites irradiated with a single pulse or low number of multiple pulses with sub-single pulse ablation fluence to determine if the periodicity is "seeded" into the material at the early stages of the irradiation may provide valuable information as well.

Some preliminary work had been conducted to explore the feasibility of ultrashort laser micromachining in optical fiber applications (Section 4.2).

Experimental work showed potential for fabrication of slits in metallic coatings on fiber facts. However, fine tuning of the ablation parameters and details of the sample preparation procedures need to be further investigated before reasonable quality of processed materials can be achieved. Microscopy techniques allowing closer inspections of the machined features should also be explored. In the work of attempting to micromachine features in optical fibers using ultrashort laser pulses, many challenges, including an improvement of surface quality, need to be addressed before practical modifications for optical fiber applications can be realized.

Lastly, a preliminary experiment from early stages of the thesis work on a double-pulse ablation technique was carried out on silicon. In this experiment was it evident that different surface morphology and features resulted from ablation with the double-pulse scheme when the delay of the two pulses was varied. By tying some possible future work with this technique together with some of the proposed hydrodynamic models for ablation mechanisms in the literature, a clearer picture can be drawn for different time frames of the ablation process.

References

1. Kartner, F.X., "Few-Cycle Laser Pulse Generation and Its Applications", Ed. Springer-Verlag/Sci-Tech/Trade 2004
2. Dausinger, F., Lichtner, F. and Lubatschowski, H., "Femtosecond Technology for Technical and Medical Applications", Springer-Verlag/Sci-Tech/Trade 2004
3. C. Rullière, , "Femtosecond Laser Pulses – Principles and Experiments", (ed.) Springer-Verlag New York Inc. 1998
4. X. Liu, High-Power Lasers in Manufacturing, Proc. SPIE, vol 3888, p.198-209
5. K. H. Leong, A. A. Said and R. L. Maynard, 2001 Proceedings. 51st Electronic Components and Technology Conference, 2001, p 210-214
6. R. Bahnisch, W. Grob, J. Staud and A. Menschig, Sens. Actuators, A **74**, 31 (1999)
7. M. S. Giridhar, K. Seong, A. Schulzgen, P. Khulbe, N. Peyghambarian and M. Mansuripur, Appl. Opt. **43**, 4584 (2004)
8. X. Liu, Proc. SPIE, **3888**, 198 (2000)
9. K. H. Leong, A. A. Said, R. L. Maynard, Proc. 51st Electron. Components and Technol. Conference, 210 (2001)
10. M. D. Shirk and P. A. Molian, J. of Laser Appl. **10,** 18 (1998)
11. A. Cavalleri, K. Sokolowski-Tinten, J. Bialkowski, M. Schreiner and D. von der Linde, J. Appl. Phys. **85**, 3301 (1999)
12. Y. L. Yao, H. Chen and W. Zhang, Int. J. Adv. Manuf. Technol. **26**, 598 (2005)
13. B. N. Chichkov, C. Momma, S. Nolte, F. von Alvensleben and A. Tünnermann, Appl. Phys. A **63**, 109 (1996)
14. D. Bäuerle: "Laser Processing and Chemistry", 3rd Edition, Springer-Verlag Berlin Heidelberg 2000
15. D. Perez and L. J. Lewis, Phys. Rev. Lett. **89**, 255504, 2002
16. K. Sokolowski-Tinten, J. Bialkowski, A. Cavalleri, D. von der Linde, A. Oparin, J. Meyer-ter-Vehn and S. I. Anisimov, Phys. Rev. Lett. **81**, 224 (1998)
17. H. Dachraoui, W. Husinsky and G. Betz, Appl. Phys. A **83**, 333 (2006)
18. J. Reif, F. Costache, S. Eckert and M. Henyk, Appl. Phys. A **79**, 1229 (2004)
19. H.-P. Cheng and J. D. Gillaspy, Phys. Rev. B **55**, 2628 (1997)
20. W. G. Roeterdink, L. B. F. Juurlink, O. P. H. Vaughan, J. Dura Diez, M. Bonn and A. W. Kleyn, Appl. Phys. Lett. **82** 4190 (2003)
21. D. Perez and L. J. Lewis, Phys. Rev. B **67**, 184102 (2003)
22. C. Cheng and X. Xu, Appl. Phys. A **79**, 761 (2004)
23. E. Leveugle, D. S. Ivanov and L. V. Zhigilei, Appl. Phys. A **79**, 1643 (2004)

24. P. Lorazo, L. J. Lewis and M. Meunier, Phys. Rev. Lett. **91**, 225502 (2003)
25. F. Quéré, S. Guizard, P. Martin, G. Petite, O. Gobert, P. Meynadier and M. Perdrix, Appl. Phys. B **68**, 459 (1999)
26. D. von der Linde and K. Sokolowski-Tinten, Appl. Surf. Sci. **154**, 1 (2000)
27. P. Lorazo, L. J. Lewis and M. Meunier, Phys. Rev B **73**, 134108 (2006)
28. L. V. Zhigilei, P. B. S. Kodali and B. J. Garrison, Chem. Phys. Lett. **279**, 269 (1997)
29. B. Rethfeld, K. Sokolowski-Tinten, D. von der Linde and S. I. Anisimov, Appl. Phys. A **79**, 767 (2004)
30. P. Gibbon, "Short Pulse Laser Interactions with Matter", Imperial College Press 2005
31. "Taunami: Mode-Locked Ti:sapphire Laser" (Part Number 0000-232A) User's Manual, Spectra-Physics Lasers 1995
32. M. Uesaka, "Femtosecond Beam Science" (ed.), Imperial College Press 2005
33. "Spitfire: Multikilohertz Pulsed Ti:Sapphire Amplifier with Pulse Stretcher and Compressor" User's Manual, Spectra-Physics Lasers
34. D. Strickland and G. Mourou, Opt. Commun. **56**, 219 (1985)
35. R. W. Boyd, "Nonliner Optics", 2nd Edition, Academic Press, 2003
36. J. Thøgersen, A. Borowiec, H. K. Haugen, E. E. McNeill and I. M. Stronach, Appl. Phys. A **73**, 361 (2001)
37. R. Trebino, "Frequency-Resolved Optical Gating: The Measurement of Ultrashrot Laser Pulses", Kluwer Academic Publishers 2002
38. Z. Sacks, G. Mourou and R. Danielius, Opt. Lett. **26**, 462 (2001)
39. M. Raghuramaiah, A. K. Sharma, P. A. Naik and P. D. Gupta, Opt. Commun. **223**, 163 (2003)
40. M. Birnbaum, J. Appl. Phys. **36**, 3688 (1965)
41. H. M. van Driel, J. E. Sipe and J. F. Young, Phys. Rev. Lett. **49**, 1955 (1985).
42. J. E. Sipe, J. F. Young, J. S. Preston and H. M. van Driel, Phys. Rev. B **27**, 1141 (1983)
43. A. E. Siegman and P. M. Fauchet, IEEE J. Quantum Electron. **QE-22**, 1384 (1986)
44. N. R. Isenor, Appl. Phys. Lett. **31**, 148 (1977)
45. J. Bonse, M. Munz and H. Sturm, J. Appl. Phys. **97**, 013538 (2005)
46. P. Rudolph and W. Kautek, Thin Solid Films **453-454**, 537 (2004)
47. X. C. Wang, G. C. Lim, F. L. Ng, W. Liu and S. J. Chua, Appl. Surf. Sci. **252**, 1492 (2005)
48. M. Couillard, A. Borowiec, H. K. Haugen, J. S. Preston, E. M. Griswold and G. A. Botton, J. Appl. Phys. **101**, 033519 (2007)
49. A. Borowiec and H. K. Haugen, Appl. Phys. Lett. **82**, 4462 (2003)

50. T. H. R. Crawford and H. K. Haugen, Appl. Surf. Sci. **253**, 4970 (2007)
51. N. Yasumaru, K. Miyazaki and J. Kiuchi, Appl. Phys. A **76**, 983 (2003)
52. J. Reif, F. Costache, M. Henyk and S. V. Pandel, Appl. Surf. Sci. **197-198**, 891 (2002)
53. F. Costache, M. Henyk and J. Reif, Appl. Surf. Sci. **186**, 352 (2002)
54. F. Costache, M. Henyk and J. Reif, Appl. Surf. Sci. **208-209**, 486 (2003)
55. T. Q. Jia, H. X. Chen, M. Huang, F. L. Zhao, J. R. Qiu, R. X. Li, Z. Z. Xu, X. K. He, J. Zhang and H. Kuroda, Phys. Rev. B **72**, 125429 (2005)
56. X. J. Wu, T. Q. Jia, F. L. Zhao, M. Huang, N. S. Xu, H. Kuroda and Z. Z. Xu, Appl. Phys. A **86**, 491 (2007)
57. Q. Wu, Y. Ma, R. Fang, Y. Liao, Q. Yu, X. Chen and K. Wang, Appl. Phys. Lett. **82**, 1703 (2003)
58. R. Wagner, J. Gottmann, A. Horn and E. W. Kreutz, Appl. Surf. Sci. **252**, 8576 (2006)
59. Y. Dong and P. Molian, Appl. Phys. Lett. **84**, 10 (2004)
60. E. M. Hsu, T. H. R. Crawford, H. F. Tiedje and H. K. Haugen, Appl. Phys. Lett. DOI: 10.1063/1.2779914 (2007)
61. B. G. Streetman, "Solid State Electronic Devices", 4th Edition, Prentice-Hall 1995
62. Cs. Tóth, J. Faure, J. van Tilborg, C. G. R. Geddes, C. B. Schroeder, E. Esarey and W. P. Leemans, Opt. Lett. **28**, 1823 (2003)
63. J. Bonse, J. M. Wrobel, J. Krüger and W. Kautek, Appl. Phys. A **72**, 89 (2001)
64. Y. Jee, M. f. Becker and R. M. Walser, J. Opt. Soc. Am. B **5**, 648 (1988)
65. B. C. Stuart, M. D. Feit, S. Herman, A. M. Rubenchik, B. W. Shore and M. D. Perry, J. Opt. Soc. Am. B **13**, 459 (1996)
66. A.-C. Tien, S. Backus, H. Kapteyn, M. Murnane and G. Mourou, Phys. Rev. Lett. **82**, 3883 (1999)
67. M. Lenzner, J. Krüger, S. Sartania, Z. Cheng, Ch. Spielmann, G. Mourou, W. Kautek and F. Krausz, Phys. Rev. Lett. **80**, 4076 (1998)
68. M. D. Perry, B. C. Stuart, P. S. Banks, M. D. Feit, V. Yanovsky and A. M. Rubenchik, J. Appl. Phys. **85**, 6803 (1999)
69. D. Ashkenasi, M. Lorenz, R. Stoian and A. Rosenfeld, Appl. Surf. Sci. **150**, 101 (1999)
70. M. Lenzner, J. Krüger, W. Kautek and F. Krausz, Appl. Phys. A. **68**, 369 (1999)
71. W. Clark and L. Walker, Proc. SPIE **5706**, 69 (2005)
72. E. Coyne, J.P. Magee, P. Mannion, G.M. O'Connor and T.J. Glynn, Appl. Phys. A **81**, 371 (2005)
73. C. Hnatovsky, R. S. Taylor, E. Simova, V. R. Bhardwaj, D. M. Rayner and P. B. Corkum, Opt. Lett. **30**, 1867 (2005)
74. C. Hnatovsky, R. S. Taylor, P. P. Rajeev, E. Simova, V. R. Bhardwaj, D. M. Rayner and P. B. Corkum, Appl. Phys. Lett. **87**, 014104 (2005)

75. V. R. Bhardwaj, E. Simova, P. P. Rajeev, C. Hnatovsky, R. S. Taylor and P. B. Corkum, Phys. Rev. Lett. **96**, 057404 (2004)
76. C. Hnatovsky, R. S. Taylor, E. Simova, P. P. Rajeev, D. M. Rayner, V. R. Bhardwaj and P. B. Corkum, Appl. Phys. A **84**, 47 (2006)
77. T. H. R. Crawford, A. Borowiec and H. K. Haugen, Appl. Phys. A **80**, 1717 (2005)
78. A. Weck, T. H. R. Crawford, D. S. Wilkinson, H. K. Haugen and J. S. Preston, Appl. Phys. A DOI: 10.1007/s00339-007-4203-6 (2007)
79. A. Borowiec and H. K. Haugen, Appl. Phys. A **79**, 521 (2004)
80. O. Varlamova, F. Costache, J. Reif and M. Bestehorn, Appl. Surf. Sci. **252**, 4702 (2006)
81. J.-C. Diels and W. Rudolph, "Ultrashort Laser Pulse Phenomena" Academic Press (2005)
82. E. D. Palik, "Handbook of Optical Constants of Solids", Ed., Boston: Academic Press, Inc. 1985
83. M. Henyk, N. Vogel, D. Wolfframm, A. Tempel and J. Reif, Appl. Phys. A **69**, S355 (1999)
84. S. Adachi, "Optical Constants of Crystalline and Amorphous Semiconductors – Numerical Data and Graphical Information", Kluwer Academic Publishers (1999)
85. "Ioeff Physico-Technical Institute: n, k Database", Online Resource, Available at: http://www.ioffe.rssi.ru/SVA/NSM/nk/index.html
86. J. Krüger, D. Dufft, R. Koter and A. Hertwig, Appl. Surf. Sci. **253**, 7815 (2007)
87. D. Giguère, G. Olivié, F. Vidal, S. Toetsch, G. Girard, T. Ozaki, J.-C. Kieffer, O. Nada and I. Brunette, J. Opt. Soc. Am. A **24**, 1562 (2007)
88. F. Wang, J. Shan, E. Knoesel, M. Bonn and T. F. Heinz, Proc. SPIE **5252**, 216 (2004)
89. D. Ashkenasi, H. Varel, A. Rosenfeld, F. Noack and E. E. B. Campbell, Appl. Phys. A **63**, 103 (1996)
90. D. Ashkenasi, H. Varel, A. Rosenfeld, F. Noack and E. E. B. Campbell, Nucl. Instrum. Methods Phys. Res. B **122**, 359 (1997)
91. P. R. Herman, A. Oettl, K. P. Chen and R. S. Marjoribanks, Proc. SPIE – Int. Soc. Opt. Eng. **3616**, 148 (1999)
92. I. H. Chowdhury, X. Xu and A. M. Weiner, Proc. SPIE **4978**, 138 (2003)
93. L. McKinney, F. Frank, D. Graper, J. Dean, P. Forrester, M. Rioblanc, M. Nantel and R. Marjoribanks, Proc. SPIE **5970**, 59701L (2005)
94. A. Yokotani, Y. Kurogi, N. Matsuo, H. Sawada, T. Ninomiya, K. Kawahara and K. Kurosawa, Electric. Eng. Jpn. **149**, 43 (2004)
95. M. Spyridaka, E. Koudoumas, P. Tzanetakis, C. Fotakis, R. Stoian, A. Rosenfeld and I. V. Hartel, Appl. Phys. Lett. **83**, 1474 (2003)
96. R. Stoian, M. Boyle, A. Thoss, A. Rosenfeld, G. Korn and I. V. Hertel, Appl. Phys. A **77**, 265 (2003)

97. A. C. Forsman, P. S. Banks, M. D. Perry, E. M. Campbell, A. L. Dodell and M. S. Armas, J. Appl. Phys. **98**, 033302 (2005)
98. T. Y. Choi, D. J. Hwang and C. P. Grigoropoulos, Appl. Surf. Sci. **197-198**, 720 (2002)
99. S. Gogoll, E. Stenzel, H. Johansen, M. Reichling and E. Matthias, Nucl. Instrum. Methods Phys. Res. B **116**, 279 (1996)
100. S.-K. Liaw, J.-Y. Chiu and S.-M. Tseng, Jpn. J. Appl. Phys. **36** L1179 (1997)
101. G. V. Mishakov and V. I. Sokolov, Proc. IEEE **4644**, 498 (2002)
102. J. Krüger, W. Kautek, M. Lenzner, S. Sartania, C. Spielmann and F. Krausz, Appl. Surf. Sci. **127-129**, 892 (1998)
103. H. Kim, J. Kim, U.-C. Paek, B. H. Lee and K. T. Kim, Opt. Lett. **29**, 1194 (2004)
104. L. Goldberg, B. Cole and E. Snitzer, Electron. Lett. **33**, 2127 (1997)
105. J. P. Koplow, L. Goldberg and D. A. V. Kliner, IEEE Photon. Technol. Lett. **10**, 793 (1998)
106. I. S. Melnik, M. Fischer, G. Flemming and R. Hibst, Proc. SPIE – Int. Soc. Opt. Eng. **1893**, 177 (1993)
107. V. S. Shah, L. Curtis, R. S. Vodhanel, D. P. Bour and W. C. Young, J. Lightwave Technol. **8**, 1313 (1990)
108. S.-M. Yeh, Y.-K. Lu, H.-H. Lin, C.-H. Hsieh and W.-H. Cheng, J. Lightwave Technol. **22**, 1374 (2004)
109. S.-M. Yeh, S.-Y. Huang and W.-H. Cheng, J. Lightwave Technol. **23**, 1781 (2005)
110. F. L. Pedrotti, S. J., L. s. Pedrotti, "Introduction to Optics", 2nd ed. Prentice Hall, Inc (1993)
111. I. H. Chowdhury, X. Xu and A. M. Weiner, Appl. Phys. Lett. **86**, 15110 (2005)
112. J. Bonse, S. Baudach, J. Krüger, W. Kautek and M. Lenzner, Appl. Phys. A **74**, 19 (2002)
113. Y. P. Deng, X. H. Xie, H. Xiong, Y. X. Leng, C. F. Cheng, H. H. Lu, R. X. Li and Z. Z. Xu, Opt. Express, **13**, 3096 (2005)
114. A. Semerok and C. Dutouquet, Thin Solid Films **453-454**, 501 (2004)
115. Z. Zhang, A. A. Van Rompay and P. P. Pronko, Appl. Phys. Lett. **83**, 431 (2003)
116. T. Kurobori, T. Yamakage, Y. Hirose, K.-I. Kawamura, M. Hirano and H. Hosono, Jpn. J. Appl. Phys. **44**, 910 (2005)